Turbulence in Aneurysms

Numerical Investigation in Abdominal Aortic Aneurysms

Digvijay S. Rawat

Technische Universiteit Delft

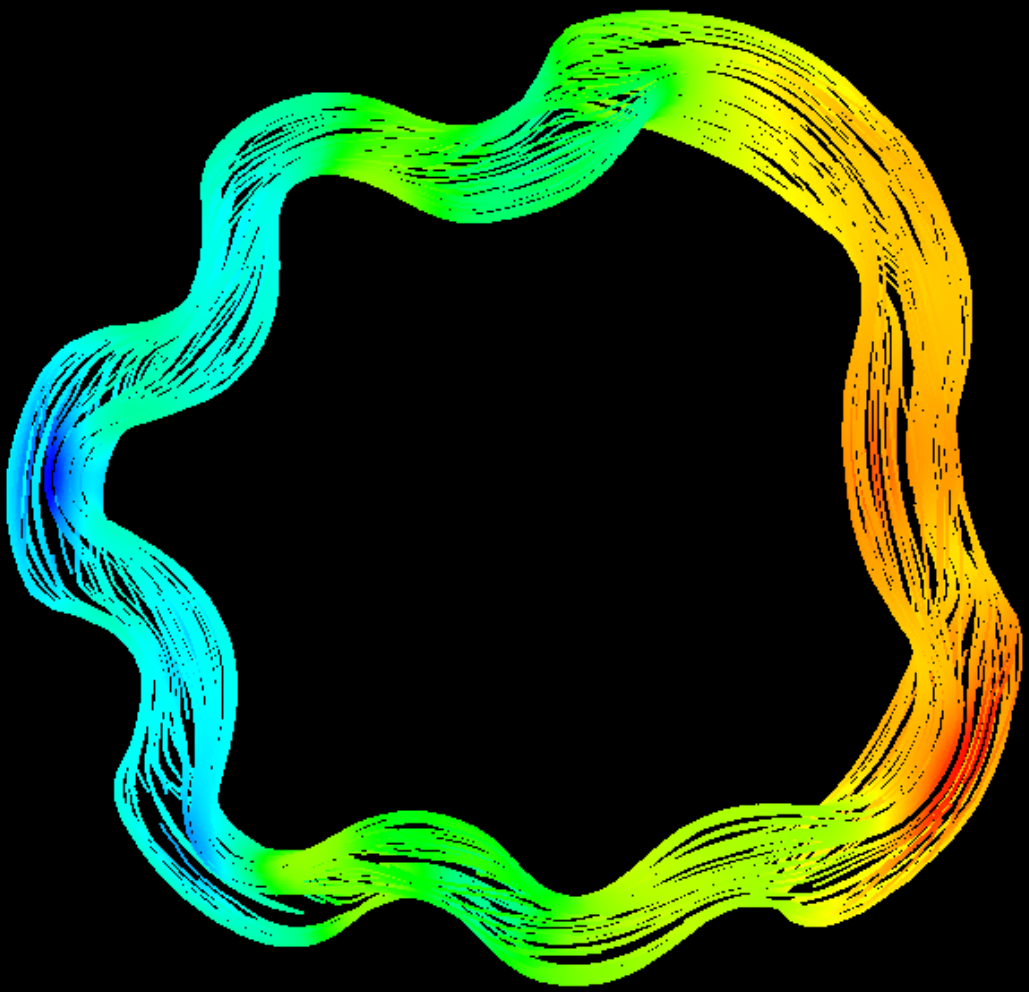

TU Delft

Turbulence in Aneurysms

Numerical Investigation in Abdominal Aortic Aneurysms

by

Digvijay S. Rawat

to obtain the degree of Master of Science at the Delft University of Technology, to be defended publicly on Tuesday October 24, 2017 at 02:00 PM.

Student Number:	4506340	
P&E Report Number:	2857	
Supervisor:	Prof. dr. ir. C. Poelma,	TU Delft
Thesis Committee:	Dr. ir. M.J.B.M Pourquie,	TU Delft
	Dr. ir. Marios Kotsonis,	TU Delft

TU Delft Delft University of Technology

Preface

This master thesis report is the end product of the research done over a period of nine months at the Aero & Hydro Laboratory at TU Delft. The thesis counts towards the completion of the masters degree in Mechanical Engineering in the track Sustainable Process & Energy Technology.

The work presented in this report is a short study on the fluid mechanics involved, and in particular turbulence, in an abdominal aortic aneurysm (AAA). Investigation is carried out on various geometries of hypothetical AAAs through CFD simulations in the commercial package ANSYS Fluent. The entire study is oriented chiefly towards the complex fluid mechanics involved rather than the bio-mechanical aspect of an AAA. The conclusions presented at the end of the report can be used as a starting point to further develop a general numerical model with respect to the flow field exhibited in an axisymmetric AAA.

Readers particularly interested in the results of this thesis are directed to chapter 5. A detailed discussion regarding the underlying mechanism of generation of turbulent fluctuations and comparison between various geometries is presented in sections 5.1.3, 5.2.1, 5.3 and 5.5. A brief discussion of the bio-mechanical aspects is also presented in sections 5.1.4 and 5.1.7.

The image on the cover represents an azimuthal instability developed on the vortex ring shed in one of the AAA geometries. The image represents the surface vortex lines on the ring coloured by the azimuthal vorticity.

Digvijay S. Rawat

Delft, October 2017

Acknowledgements

First and foremost, I would like to thank my supervisor *Prof. Christian Poelma* for giving me the opportunity to work on such an interesting topic and for the patience and understanding he showed in dealing with me. A special thanks goes out to *Dr. Mathieu Pourquie* for his extensive knowledge related to almost anything and everything in CFD. I also enjoyed all the non thesis related discussions with him on various topics such as the university canteen, old academic traditions and interesting lab stories (‘*my books have a large diffusion coefficient!*’). Further, I would like to thank *Dr. Marios Kotsonis* for taking out the time from his schedule to be a part of my thesis defence.

I had the opportunity to briefly present a part of the current work to *Prof. Stefan Hickle* and fellow master student *Carsten Sanders* and am grateful for their valuable feedback and suggestions. I would like to acknowledge *Caroline Legierse* for helping out with the administrative tasks concerning the thesis defence.

The past few months, in the aftermath of my father’s passing away, have been extremely hard. I would like to acknowledge the support I got from everyone around me; relatives, friends, and most importantly my mother. I would also like to take this opportunity to thank my father who constantly encouraged me to chase my dreams and has always been a source of inspiration for me.

I have thoroughly enjoyed working in the laboratory and a large credit of it goes to fellow master students. Working on a thesis is far more enjoyable with random conversations and good friends; so massive props to *Abhiroop, Bihari, Bum, Doctor, Jalebi, Sai* and *Veera*. I had a memorable time with all my friends at Cesar Franckstraat and would like to thank them for all the wonderful memories: *Abhishek, Jairaj, Mittal, Ozi* and *Vaibhav*. I would also like to thank my football mates for the great weekend games we have had over the past two years.

A final small but necessary thanks is in order to IceFrog and his team at Valve for developing the video game DotA 2. I have been playing since more than 4 years and apart from acting as a stress buster, DotA 2 has given me some great friends and instilled a general sense of confidence, perseverance, teamwork and patience in me.

Digvijay S. Rawat

Delft, October 2017

Summary

An aneurysm refers to the local dilation or ballooning of a blood vessel and if left unchecked, almost every aneurysm continues to grow in size until it eventually ruptures. The abdominal aorta is the most common location for an aneurysm to form and can turn lethal in the event of rupture. Even after decades of research, the precise role of each of the numerous factors involved in the inception and growth of an abdominal aortic aneurysm (AAA) is still not known. In this study, the role of turbulence in a hypothetical axisymmetric AAA (4A) geometry is investigated.

Majority of the investigations on AAAs are done through CFD simulations and this thesis is no exception. Since the current clinical practice to classify AAAs is on the basis of their size (diameter), it was decided to vary the geometric parameters viz., the expansion ratio (ER) and the expansion angle (EA). ER is the ratio of the maximum AAA diameter to the healthy aorta diameter whereas the EA is a measure of the steepness of the arterial wall between the healthy aorta and the aneurysm. All the combinations of ER and EA lead to a total of 8 cases. Flow parameters such as the Reynolds number and the Womersley number are chosen in accordance with the average values found in humans and are kept constant across all the cases.

The simulations show that a vortex ring is shed just after peak systole in every case. The vortex ring, at inception, is similar for all cases within visual limits. As the rings travels downstream, an azimuthal instability sets in that grows with time. This is the short wave or the elliptical instability usually associated with a vortex pair perturbed by an infinitesimally small amplitude sinusoidal wave. The number of waves formed along the circumference of the ring as a result of the instability varies from case to case but in general, the number of waves decreases as the diameter of the aneurysm increases. The growth of this instability, along with interaction of the ring with the remnants of the flow field form the previous cardiac cycle, cause it to break down into smaller vortices which subsequently decay. The manner in which the ring breaks down is different from cycle to cycle which leads to turbulent fluctuations.

It was also observed that the vortex ring does not break down in all the cases. Specifically, it does not break in the 2 cases that had an expansion angle of 15°. This suggests that turbulence in AAAs is perhaps a stronger function of the EA rather than the ER. Investigations were also carried out to identify recirculating or dead flow regions in all the cases as an intraluminal thrombus (ILT) is a commonly found feature in AAAs. An ILT deprives the surrounding arterial tissue of oxygen thereby weakening the aortic wall and increasing the risk of rupture. It could be seen from the simulations that the inflection regions of the 4A geometry are most prone to the formation of an ILT which is in agreement with the physically observed locations. Finally, the oscillatory shear index (OSI) is investigated to see the influence of

turbulence on a hemodynamic parameter. It was found that for the geometries tested, there is no clear co-relation between the two.

From this thesis, numerous conclusions can be drawn. But perhaps the most important conclusion is that the flow field in an AAA is very complex and sensitive to various input parameters such as the ER and EA. Although flow parameters such as the Reynolds and the Womersley number were kept constant across all the cases investigated in this thesis, existing literature clearly highlights the dependence of the flow field on them. As such, the desire to be able to formulate general co-relation trends between various flow field quantities in AAAs is wishful thinking at best.

Contents

List of Figures

List of Tables

Abbreviations

Acronym	Full Form
AAA	**A**bdominal **A**ortic **A**neurysm
CFD	**C**omputational **F**luid **D**ynamics
4A	**A**xisymmetric **A**bdominal **A**ortic **A**neurysm
DNS	**D**irect **N**umerical **S**imulation
UDF	**U**ser **D**efined **F**unction
WSS	**W**all **S**hear **S**tress
OSI	**O**scillatory **S**hear **I**ndex
ILT	**I**ntra**l**uminal **T**hrombus
TKE	**T**urbulent **K**inetic **E**nergy
EA	**E**xpansion **A**ngle
ER	**E**xpansion **R**atio

List of Symbols

Symbol	Usage
Re	Reynolds Number
α	Womersley Number
ϕ	Phase
ρ	Density
μ	Dynamic Viscosity
ν	Kinematic Viscosity
η	Kolmogorov Length Scale
λ	Taylor Microscale
a	Vortex Ring Core Diameter
d	Vortex Ring Diameter
d_0	Healthy Aorta Diameter
L_h	4A Streamwise Length
t_v	Vortex Ring Shedding Time Scale
t_a	Advective Time Scale
t_s	Stability Time Scale
U	Vortex Ring/Bubble Translational Velocity
Γ	Circulation

1

Introduction and Overview

The current chapter provides an introduction to the thesis. First, a brief overview of the cardiovascular system and abdominal aortic aneurysms (AAA) is presented in sections 1.1 and 1.2, respectively. Then in section 1.3 the role of hemodynamics in an AAA is explained and in section 1.4 the relevance of computational fluid dynamics in investigating AAAs is discussed. Finally, the thesis objective is formulated in section 1.5 and a brief overview of the thesis structure is presented in section 1.6.

1.1. Cardiovascular System

The human cardiovascular system is an organ system whose primary function is to circulate blood and carry out transport of nutrients and waste throughout the entire body [1]. The cardiovascular system consists of the heart, blood and blood vessels and is essentially comprised of two circulation loops: the pulmonary circulation and the systemic circulation. Pulmonary circulation refers to the pumping of the oxygen depleted blood from the heart to the lungs via the pulmonary artery and then being returned to the heart after being oxygenated by the lungs, via the pulmonary vein. Systemic circulation refers to blood circulation to the entire body but the lungs. It involves pumping of oxygenated blood from the heart through the aorta to all the body parts and the return of oxygen depleted blood back to the heart through the vena cava. The systemic and pulmonary circulation together form the cardiac cycle. On an average, the cardiac cycle occurs approximately 75 times per minute or once every 0.8 seconds in an adult human.

1.2. Abdominal Aortic Aneurysm (AAA)

An aneurysm refers to the localized bulging or ballooning of a blood vessel wall. An aneurysm can form in any blood vessel but is commonly formed in the brain and the aorta. Aortic aneurysm is a common cardiovascular disease usually affecting men above 50 years of age who typically have high blood pressure or smoke or have it in their family history. Aortic aneurysms can be located in the thoracic aorta but are more commonly located in the abdominal aorta, the latter being commonly termed as AAA or Triple A. A healthy abdominal aorta, depending chiefly on age and sex, measures approximately 20 mm in diameter [2]. Figure 1.1 depicts a healthy aorta and an AAA.

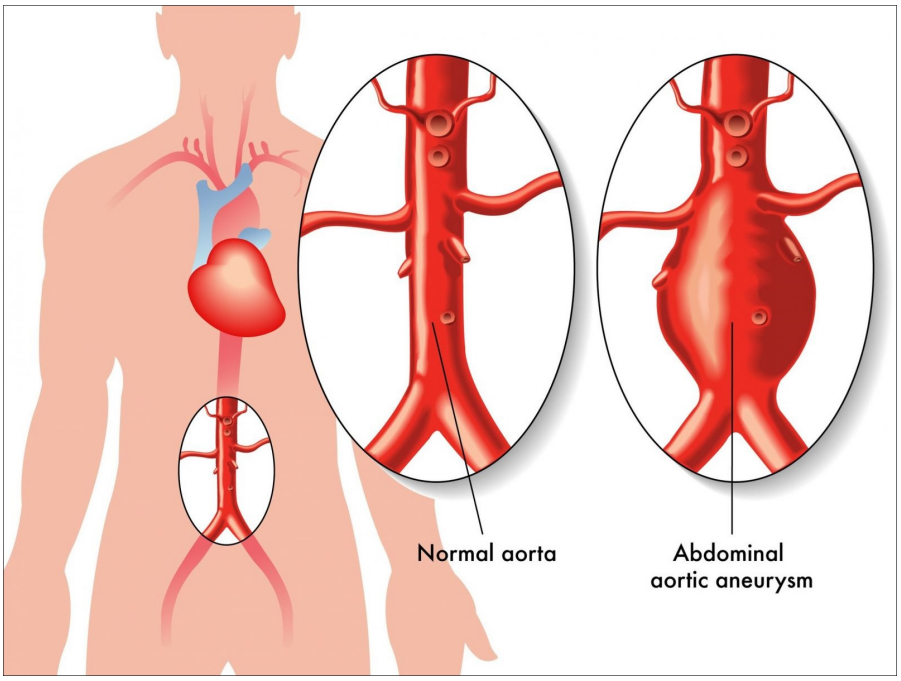

Figure 1.1: Abdominal Aortic Aneurysm. Reproduced from [3]

What really makes aneurysms dangerous is that the majority of cases are asymptomatic; a person suffering from an aneurysm is generally unaware of it. With time, an aneurysm expands further and if it grows large enough such that the arterial wall tension exceeds the material strength, the aneurysm can burst leading to massive internal bleeding which more often then not leads to death. 65 - 75% of ruptured AAAs cause death before the patient can even reach the hospital and nearly 90% die before they can be operated on [4]. Thus, it is extremely important to be able to identify the formation and growth of an AAA so that it can be monitored and operated on, if required. The current clinical practice to decide if an aneurysm needs to be operated on is chiefly decided by its diameter; usually treatment is recommended if the diameter of the AAA is more than 5.5 cm in men or 5 cm in women [5]. Although the criterion of maximum diameter is standard clinical practice, it is common knowledge that aneurysms which are smaller in size can rupture and aneurysms which are larger may remain stable [6] thereby warranting further research on the topic.

An AAA is widely regarded as the result of aorta degeneration although the exact mechanism of this degenerative process remains unclear even today [7]. As depicted in figure 1.2, a healthy abdominal aorta, like any other artery, has three tissue layers: the innermost layer, the intima, consisting of endothelial cells; the middle layer, the media, containing smooth muscle cells and the outermost layer, the adventitia, chiefly consisting of collagen. Although an AAA causes bulging of all the layers of the aorta, it only starts developing after the degeneration of media in the vessel wall [7]. While an aneurysm may be initially formed only due to biological factors, hemodynamics play a major role in its subsequent development and more importantly, in its rupture.

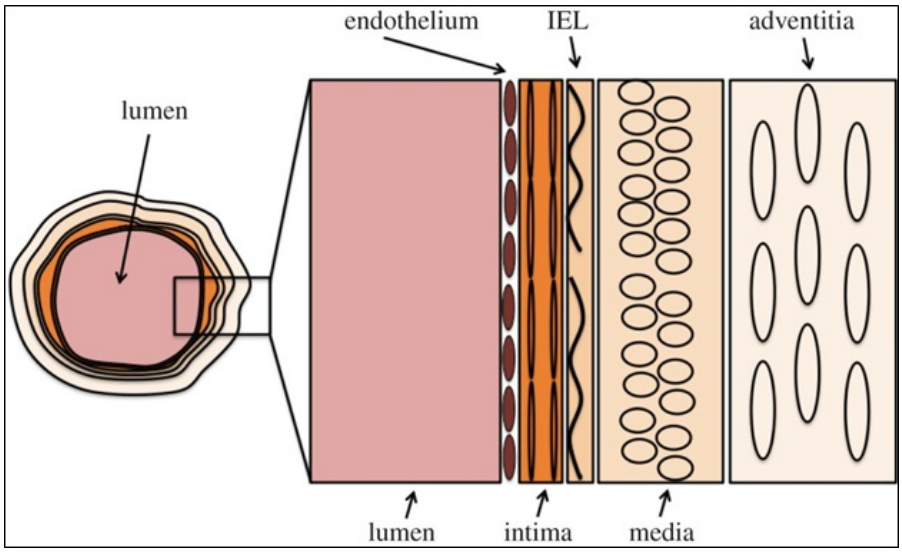

Figure 1.2: Aortic wall structure representing all the three tissue layers of the aorta. Lumen refers to the space through which blood flows. The endothelium cells line the intima layer and are in constant contact with blood flow. Reproduced from [8]

1.3. Hemodynamics

Hemodynamics refers to the dynamics of blood flow. Since the intima layer is the innermost layer and is thus always in contact with flowing blood, the endothelial cells are perpetually subjected to the hemodyanmic forces generated by the dynamics of blood flow. Hemodynamic forces consist of three components: normal hydrostatic pressure, wall shear stress and the relative wall shear strain [9]. Hydrostatic pressure is the force acting normally on the vessel wall. Wall shear stress refers to the tangential stress acting on the vessel wall caused due to blood flow. Finally, relative wall strain is the stretching of the vessel wall in the circumferential direction due to the tensile/ hoop stress present in the wall itself.

Although the endothelial cells are not capable of sensing the total blood flow rate directly, arteries can dilate or contract locally in response to change in flow rate. This is possible due to the fact that the endothelial cells can sense the wall shear stress acting on them [10] which in turn depends on the flow rate. Arteries can adapt to cycle to cycle changes in wall shear stress by dilating or contracting locally

to maintain the value of flow induced wall shear stress at approximately 15 $dynes/cm^2$ [11]. Similarly, arteries can also adapt to long term changes in wall shear stress by remodelling themselves to a larger/ smaller diameter which is done by changing the thickness of the intima and media layers.

Thus, it is easy to see how hemodynamic forces, and in particular the wall shear stress, can influence the shape and diameter of an artery. Although the wall shear stress alone does not result in the formation of an aneurysm but when combined with biological factors such as atherosclerosis, smoking, genetics etc., it does play a major role in its eventual development and rupture. Since blood flow is pulsatile and not strictly uni-directional everywhere, the wall shear stress (WSS) vector keeps changing its magnitude and direction throughout the cardiac cycle. To be able to quantify such an oscillatory nature of the WSS vector, Ku et al [12] proposed the hemodynamic parameter Oscillatory Shear Index (OSI) that basically describes how much the WSS vector changes direction from its mean direction. Some examples of other WSS based hemodynamic parameters are: mean WSS, maximum WSS, gradient oscillatory number (GON) and the aneurysm formation index (AFI). Some examples of non WSS based hemodynamic parameters are: Rupture Potential Index (RPI) [13], aneurysm expansion rate [14], presence of intraluminal thrombus [15] and degree of asymmetry [16]. In this thesis, the OSI will be used as the hemodynamic parameter to gain insight about AAAs and will be discussed in detail later in section 2.5.5.

1.4. AAA, Hemodynamics & CFD

Computational Fluid Dynamics (CFD) is the branch of fluid mechanics in which fluid flow equations are solved numerically by discretizing the problem domain into many smaller domains. It is essentially a combination of fluid dynamics and numerical methods for solving partial differential equations, which, in the case of fluid flow are the Navier Stokes equations. Since the equations are solved numerically on a computer, problems usually associated with experimental procedures such as setup, calibration of instruments, reducing environmental disturbances etc., are circumvented. Also, with the increase in computational power in the last couple of decades, it is now possible to solve large and complex systems computationally with higher accuracy. Finally, since the governing equations are solved numerically, output parameters such as hemodynamic parameters for AAAs can be easily calculated and visualised.

A considerable amount of research has been done on aneurysms with the help of CFD. With respect to AAAs, researchers have mainly focused on calculation and visualization of wall shear stress and associated hemodynamic parameters to understand the mechanism behind the growth and rupture of an AAA. Variation of input parameters such as expansion ratio, velocity waveform, blood rheology and geometric shape and thereby the effect on the wall shear stress, is well documented. Keeping all this in mind, the research objective of this thesis is formulated.

1.5. Thesis Objective

It is important to define clear and concise objectives so that the scope and aim of the thesis is well defined. The basic aim of this thesis is to investigate the flow field in an axisymmetric AAA (abbreviated as 4A hence) and try to understand the underlying flow mechanism. Substantial research has already been done using CFD but a relatively unexplored topic is the transition of the flow field to turbulence and its effect on hemodynamic parameters. Since blood flow is pulsatile in nature, the Reynolds number is not constant but rather changes from phase to phase within a cardiac cycle. In a healthy abdominal aorta, the mean flow averaged over an entire cycle is generally laminar. However, it can be transitional or even turbulent during the peak systole when the flow rate is high. Further, it will be interesting to know if turbulence in an AAA will be affected by the standard input parameters such as aneurysm diameter and how turbulence in the flow field will affect the usual hemodynamic parameters such as oscillatory shear index (OSI) in an AAA. Thus, the objective of this thesis is framed as

To investigate the transition to turbulence and its dependency on the geometric parameters in pulsatile blood flow through an axisymmetric abdominal aortic aneurysm

The above objective can be broken down into many smaller objectives such as

- What assumptions and simplifications can be considered to carry out a CFD simulation of the flow field inside the 4A geometry?
- Which geometric parameters can be expected to have an impact on turbulence?
- How is turbulence affected by change in geometric parameters?
- How does the change in turbulence affect a hemodynamic parameter such as the OSI?
- What is the underlying mechanism of the transition to turbulence?

1.6. Overview

In order to work towards the above mentioned objective(s), a planned approach needs to be adopted to ensure that efforts are put in a meaningful direction. A brief overview of the planned steps is as follows

1. **Input Parameters**

   For this project, geometric parameters are focussed on. The reason for making such a choice is that the current clinical practice classifies AAAs on their diameter size which is a geometric parameter. Also, it would be interesting to see how turbulence varies and how it influences the OSI as an AAA progresses in size. Apart from the AAA diameter, the expansion angle is also varied. The expansion angle is varied as flow in an AAA has some common characteristics with flow over a backward facing step (BFS) and it is known that flow over a BFS is influenced by the expansion angle. Thus, it is desirable to see the effect of expansion angle on the flow in an

AAA. The range of both these input parameters is decided from literature and physically observed values. Other factors involved in the problem such as the Reynolds number are also explained in chapter 2.

2. **Geometry Creation and Meshing**

   Since geometric input parameters are being varied, numerous 4A geometries have to be made. In total, 8 geometries are made. In all the geometries, the total length of the aneurysm is kept constant. The geometries are made with the help of SolidWorks 2015 and then imported to ANSYS ICEM CFD for meshing. Since the geometries are cylindrical in shape, O-grid blocking is done to ensure a high quality mesh and avoid distortion/ skewness of mesh elements near the boundary. Further details on computational aspects can be found in chapter 3.

3. **CFD Simulation**

   ANSYS Fluent 16.1 is used as the solver. Transient simulations are done as blood flow is pulsatile. A user defined function (UDF) is written to serve as the velocity input keeping in mind the pulsatile nature of blood flow. Although blood is a non Newtonian fluid, it is assumed to behave in a Newtoninan fashion in all the simulations for reasons explained in the next chapter. Each simulation is run on a reasonably fine mesh for a sufficient number of cardiac cycles, as justified in chapter 4, to achieve reasonable temporal convergence.

4. **Post Processing**

   During every simulation, data of relevant variables, such as velocity, is exported. Data is exported in ASCII format as it allows export at selective locations. Data visualisation through contour plots and relevant graphs is done in MATLAB from the exported ASCII files.

5. **Results**

   All the results obtained from the simulations are presented in chapter 5. To get a general idea of the flow field in a 4A geometry, contour plots of variables such as velocity and vorticity are presented. Since the objective of this thesis is to investigate turbulence, comparison plots are made between various geometric configurations to see how turbulence is affected by changing geometric parameters of an AAA. Finally, the underlying mechanism of transition to turbulence is also discussed.

6. **Conclusion**

   The conclusions that can be drawn from this study are presented in chapter 6. Further, possible ideas and avenues for building up on the current work are also presented.

2

Theoretical Background

This chapter presents a detailed perspective on the theoretical aspects of the characteristics of blood flow through an abdominal aortic aneurysm (AAA). The objective of this chapter is to help the reader in getting familiarised with the theoretical concepts involved so that they are able to understand the decisions taken regarding simulations and are able to interpret the obtained results.

2.1. Pulsatile Blood Flow

The opening and closing of heart valves during every cardiac cycle gives rise to a pulsatile pressure gradient that drives the blood flow in arteries thereby causing blood flow to be pulsatile. To understand the basic fundamentals of pulsatile blood flow in an artery, it is a good idea to investigate fluid flow driven by an oscillatory pressure gradient in a straight cylindrical tube. To describe fluid flow in a cylindrical tube, the Navier Stokes equations along with the continuity equation, in cylindrical co-ordinates, are studied. The Navier Stokes equations are obtained by applying Newton's second law of momentum conservation to fluid flow in a control volume. The Navier Stokes equations and the continuity equation, obtained by applying conservation of mass across a control volume, together form the governing equations of fluid flow. The choice to express the Navier Stokes equations and the continuity equation in cylindrical co-ordinates is obvious owing to the cylindrical geometry of the fluid flow domain. The continuity equation for a constant and non zero density ρ, in cylindrical co-ordinates, is given by [17]

$$\frac{1}{r}\frac{\partial}{\partial r}(ru_r) + \frac{1}{r}\frac{\partial u_\varphi}{\partial \varphi} + \frac{\partial u_z}{\partial z} = 0 \tag{2.1}$$

The Navier Stokes equations for a constant and non zero density ρ, in cylindrical co-ordinates, are given by [17]

$$\frac{\partial u_r}{\partial t} + (\mathbf{u}.\nabla)u_r - \frac{u_\varphi^2}{r} = -\frac{1}{\rho}\frac{\partial p}{\partial r} + \nu\left(\nabla^2 u_r - \frac{u_r}{r^2} - \frac{2}{r^2}\frac{\partial u_\varphi}{\partial \varphi}\right) \tag{2.2}$$

$$\frac{\partial u_\varphi}{\partial t} + (\mathbf{u}.\nabla)u_\varphi + \frac{u_r u_\varphi}{r} = -\frac{1}{\rho r}\frac{\partial p}{\partial \varphi} + \nu\left(\nabla^2 u_\varphi - \frac{u_\varphi}{r^2} + \frac{2}{r^2}\frac{\partial u_r}{\partial \varphi}\right) \tag{2.3}$$

$$\frac{\partial u_z}{\partial t} + (\mathbf{u}.\nabla)u_z = -\frac{1}{\rho}\frac{\partial p}{\partial z} + \nu\nabla^2 u_z \tag{2.4}$$

In all the above equations, r, φ and z denote the radial, azimuthal and axial directions. **u** is the complete velocity vector that is comprised of u_r, u_φ and u_z; the velocities in the radial, azimuthal and axial directions, respectively. In the above Navier Stokes equations, it is assumed that there are no body forces acting on the fluid and that the fluid has a constant kinematic viscosity ν. A general solution to the full system of the Navier Stokes equations, such as equations 2.1 - 2.4, has not been found yet but for some special cases wherein certain assumptions can be justly made, an analytical solution can be obtained. Fluid flow that is driven by an oscillating pressure gradient through a cylinder is one such special case. The assumptions that can be made, with their respective consequences, are as follows

- $Axisymmetric\ Flow \longrightarrow \partial/\partial\varphi = 0$
- $Nearly\ uni-axial\ flow \longrightarrow u_r = 0, u_\varphi = 0$

Equations 2.1 - 2.4 simplify substantially with the help of the above mentioned assumptions. Equation 2.1 simplifies to

$$\frac{\partial u_z}{\partial z} = 0 \tag{2.5}$$

Equation 2.3 vanishes completely. Equations 2.2 and 2.4 simplify to

$$-\frac{1}{\rho}\frac{\partial p}{\partial r} = 0 \longrightarrow \frac{\partial p}{\partial r} = 0 \tag{2.6}$$

$$\frac{\partial u_z}{\partial t} = -\frac{1}{\rho}\frac{\partial p}{\partial z} + \nu\nabla^2 u_z \tag{2.7}$$

From equation 2.5 and the assumption of axisymmetric flow, it can be concluded that $u_z = u_z(r,t)$. Similarly, with the help of equation 2.6, it can be concluded that $p = p(z,t)$. Since u_z is the only non zero velocity component, the subscript z is dropped hence onwards. Equation 2.7 is now further worked upon.

$$\frac{\partial u}{\partial t} = -\frac{1}{\rho}\frac{\partial p}{\partial z} + \nu\left[\frac{1}{r}\frac{\partial}{\partial r}\left(r\frac{\partial}{\partial r}\right) + \frac{1}{r^2}\frac{\partial^2}{\partial \varphi^2} + \frac{\partial^2}{\partial z^2}\right]u \tag{2.8}$$

$$\frac{\partial u}{\partial t} = -\frac{1}{\rho}\frac{\partial p}{\partial z} + \nu\left[\frac{1}{r}\frac{\partial}{\partial r}\left(r\frac{\partial u}{\partial r}\right)\right] \tag{2.9}$$

$$\frac{\partial u}{\partial t} = -\frac{1}{\rho}\frac{\partial p}{\partial z} + \nu\left[\frac{\partial^2 u}{\partial r^2} + \frac{1}{r}\frac{\partial u}{\partial r}\right] \tag{2.10}$$

Since $p = p(z,t)$, $\partial p/\partial z$ is only a function of t. According to Womersley [18], an oscillatory pressure gradient can be expressed as a Fourier series since it is periodic in nature.

$$\frac{\partial p}{\partial z} = -Ae^{i\omega t} \tag{2.11}$$

In the above expression, A is the pressure gradient amplitude and ω is the normal frequency. To correlate this expression to the human oscillatory pressure gradient, the heart beat rate would be denoted by the normal frequency f which is correlated to ω by the relation $\omega = 2\pi f$. The pressure gradient in equation 2.11 can also be comprised of multiple harmonics but for the sake of simplicity, only one harmonic is considered for this derivation. Substituting the above expression in equation 2.10,

$$\frac{\partial u}{\partial t} = \frac{1}{\rho}Ae^{i\omega t} + \nu\left[\frac{\partial^2 u}{\partial r^2} + \frac{1}{r}\frac{\partial u}{\partial r}\right] \tag{2.12}$$

Since the flow is pressure driven and $u = u(r,t)$, it is possible to split u as

$$u(r,t) = U(r)e^{i\omega t} \tag{2.13}$$

Substituting expression 2.13 in equation 2.12,

$$Ui\omega e^{i\omega t} = \frac{1}{\rho}Ae^{i\omega t} + \nu e^{i\omega t}\left[\frac{d^2U}{dr^2} + \frac{1}{r}\frac{dU}{dr}\right] \tag{2.14}$$

$$Ui\omega = \frac{A}{\rho} + \nu\left[\frac{d^2U}{dr^2} + \frac{1}{r}\frac{dU}{dr}\right] \tag{2.15}$$

The above obtained equation is a linear, second order ordinary differential equation and in particular, is the Bessel differential equation. Its solution, without further proof, is

$$U(r) = \frac{A}{\rho}\frac{1}{i\omega}\left[1 - \frac{J_0\left(r\sqrt{\frac{\omega}{\nu}}i^{3/2}\right)}{J_0\left(R\sqrt{\frac{\omega}{\nu}}i^{3/2}\right)}\right] \tag{2.16}$$

where J_0 is the zero order Bessel function of the first kind, R is the radius of the cylinder and $i = \sqrt{-1}$. The dimensionless number $R\sqrt{\frac{\omega}{\nu}}$ is called the Womersley number and is usually denoted by α. The Womersley number is of great importance in oscillatory flows and is explained in section 2.3. The above obtained expression for U can now be substituted in equation 2.13 to get the complete velocity profile.

$$u(r,t) = \frac{A}{\rho}\frac{1}{i\omega}\left[1 - \frac{J_0\left(\frac{r}{R}\alpha i^{3/2}\right)}{J_0(\alpha i^{3/2})}\right]e^{i\omega t} \tag{2.17}$$

Thus, the analytical solution for an oscillatory flow in a straight cylindrical tube is known. However, it must be noted that the above obtained solution is only for the case wherein the pressure gradient can be expressed as a pure single harmonic. Since the pressure gradient in the human cardiac cycle cannot be expressed as a single harmonic, the velocity profiles in arteries are not exactly the same as suggested by the above expression.

2.2. Flow Regime

A single Reynolds number cannot be used to describe blood flow due to its pulsatile nature. In general, blood flow can be regarded as laminar when considering the mean flow averaged over the entire cardiac cycle but during certain phases of the cardiac cycle, such as the peak systole, the flow rate and hence the velocity magnitude are high enough to cause transitional or turbulent flow. Since the Reynolds number depends on the vessel diameter and fluid velocity, the average Reynolds number ranges from 1 in small vessels such as arterioles to as high as 4000 in large arteries such as the aorta [10]. Keeping in mind the general threshold for the onset of turbulence in pipe flow (Reynolds number between 2000 and 2300), transitional or turbulent flow can be expected in large arteries such as the aorta during the peak systole at least. From a biological point of view, it is important to investigate turbulence in blood flow as turbulent shear stresses can easily attack and damage the endothelial cell lining on the arterial wall and injure living blood cells, as shown by Davies et al [19].

The flow field in an AAA is particularly susceptible to turbulence due to temporal acceleration or deceleration and spatial acceleration or deceleration. The pulsatile nature of blood flow is responsible for the temporal acceleration or deceleration whereas the geometry of the AAA is responsible for spatial acceleration or deceleration. Temporal acceleration refers to the systolic phase of the cardiac cycle during which the applied pressure keeps increasing thereby accelerating the flow whereas temporal deceleration refers to the diastolic phase of the cardiac cycle when the flow decelerates due to decrease in pressure applied. From the knowledge of basic fluid mechanics, we can expect that temporal acceleration will help in stabilizing the flow but temporal deceleration destabilizes it. Since an aneurysm has a larger diameter than a healthy aorta, flow in an AAA involves blood passing through a diverging section where it is subjected to an adverse pressure gradient that decelerates the flow and can cause flow separation. A converging section is present at the distal end of an AAA where the aneurysm diameter blends into the normal aortic diameter causing blood flow to accelerate due to the favourable pressure gradient. Thus, due to these factors, transition to turbulence can be expected in aneurysms at lower than usual thresholds.

2.3. AAA Relevant Parameters

2.3.1. Reynolds Number

The Reynolds number (Re) of a flow indicates the ratio of inertial forces to viscous forces. It is a non dimensional number and is formulated as

$$Re = \frac{\rho v L}{\mu} \tag{2.18}$$

where ρ is the fluid density, v is the characteristic velocity magnitude, L is the characteristic length and μ is the dynamic viscosity. For flow in a circular cylinder, the cylinder diameter (d) is the characteristic length and the average velocity over the cross section (bulk velocity) of the cylinder is the characteristic velocity. For flow in a circular cylinder, a Reynolds number in the range of 2000-2300 is the threshold for laminar to turbulent transition. Pulsatile blood flow cannot be described with a constant Reynolds number as the flow velocity is constantly changing with time. To depict characteristics of pulsatile blood flow, two Reynolds numbers are defined: mean and peak Reynolds number. The mean Reynolds number is based on the mean velocity (v_m) taken over a cardiac cycle and the peak Reynolds number is based on the peak velocity (v_p) in the time dependent velocity profile.

$$Re_p = \frac{\rho v_p d}{\mu}, Re_m = \frac{\rho v_m d}{\mu} \tag{2.19}$$

Different parts of the arterial tree have characteristic pulsatile velocity profiles. In the abdominal aorta, the mean Reynolds number is around 600 (laminar) during resting conditions [10]. Adopting the Mills velocity profile to this mean Re results in a peak Re of nearly 3150 (turbulent).

2.3.2. Womersley Number

The Womersley number (α) is a non dimensional number that is of significant relevance in pulsatile flows. It denotes the ratio of the unsteady inertial forces to viscous forces and is formulated as

$$\alpha = R\sqrt{\frac{\omega}{\nu}} = D\sqrt{\frac{\pi\rho}{2\mu T}} \tag{2.20}$$

where ω is the angular frequency associated with the pulsatility of the flow, R is the cylinder radius and ν is the kinematic viscosity. With respect to the human circulatory system, T is the time period of one cardiac cycle, which, in this project is taken to be 0.8 seconds. From the formula it is evident that keeping everything else constant, an increase in heart beat rate (thereby reducing T) results in an increase in the Womersley number. Thus, a higher heart beat rate results in a higher Womersley number. Figure 2.1 depicts the velocity profiles for four different Womersley numbers corresponding to the analytical solution derived in section 2.1 for an amplitude of unity. Due to the simple sinusoidal

pressure gradient, velocity profiles corresponding to the phases from 180 to 360 degrees are opposite of the 0 to 180 degrees part and have thus been omitted from the figure. From the figure, it can be seen that for a low Womersley number, the velocity profiles attain a parabolic shape but at a higher Womersley number, the profiles are a lot flatter. At low Womersley numbers, the low frequency allows the profile to attain a parabolic shape but at higher Womersley numbers, the high frequency does not give enough time for the parabolic profile to develop. Thus, the flow is dominated by viscous forces at low values of α but by $\alpha = 3$ [20], unsteady inertial forces become significant which leads to the departure from the quasi steady parabolic profile.

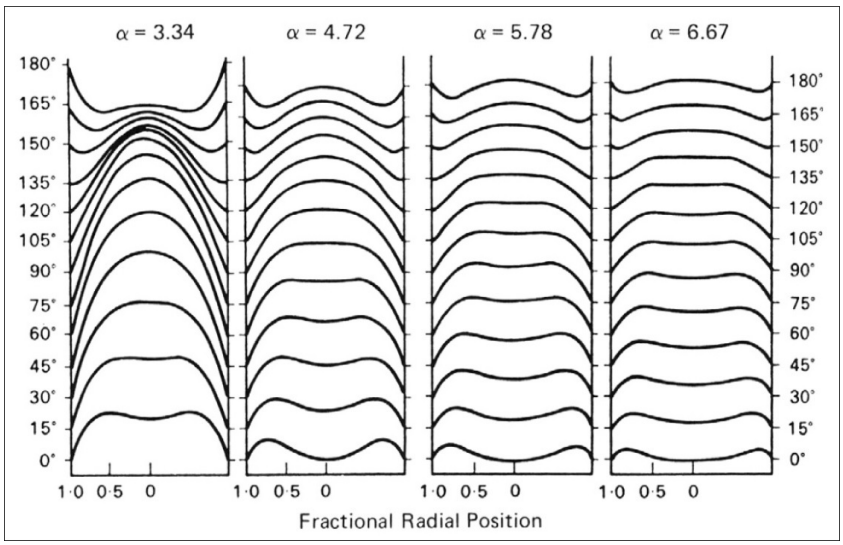

Figure 2.1: Womersley profiles for a simple sinusoidal pressure gradient. At low α, viscous forces dominate which leads to the classic parabolic profile but at higher α, non inertial forces cause the profiles to flatten out. Profiles for phases 180 degree onwards are left out since they are simply the opposite of the profiles from 0 to 180 degrees. Here, a phase of 0 degree corresponds to the start of a cycle and a phase of 360 degree corresponds to the end of a cycle or the start of the next cycle. Reproduced from [21]

Flow reversal near the wall can also be seen in figure 2.1. The reversal of pressure gradient is responsible for this which, in turn depends on the temporal acceleration and deceleration of the flow field. Thus, the amount of flow reversal depends on the Womersley number and is higher for low Womersley numbers. Another important aspect of pulsatile flow is that there exists a phase lag between the applied pressure gradient and the flow rate. The phase lag increases with increase in pulsating frequency or the Womersley number [22]. In this thesis, the average value of 75 heart beats per min (BPM) is adopted. This results in a value of 16.9 for the Womersley number.

2.3.3. Choice of Inlet Profile

In order to properly model the flow field in an AAA, a good approximation of the time varying flow rate needs to be imposed at the inlet. Mills et al [23] took a series of measurements recording the velocity waveforms in numerous patients at various locations including the abdominal aorta through

cardiac catheterization. Their obtained waveform has been used by many researchers such as Finol and Amon [24]. In this thesis, the time dependent inlet waveform is borrowed from the work of Tim Van Kruchten [25], who adjusted the waveform of Finol and Amon to obtain a mean Reynolds number of 600. This waveform is illustrated in figure 2.2.

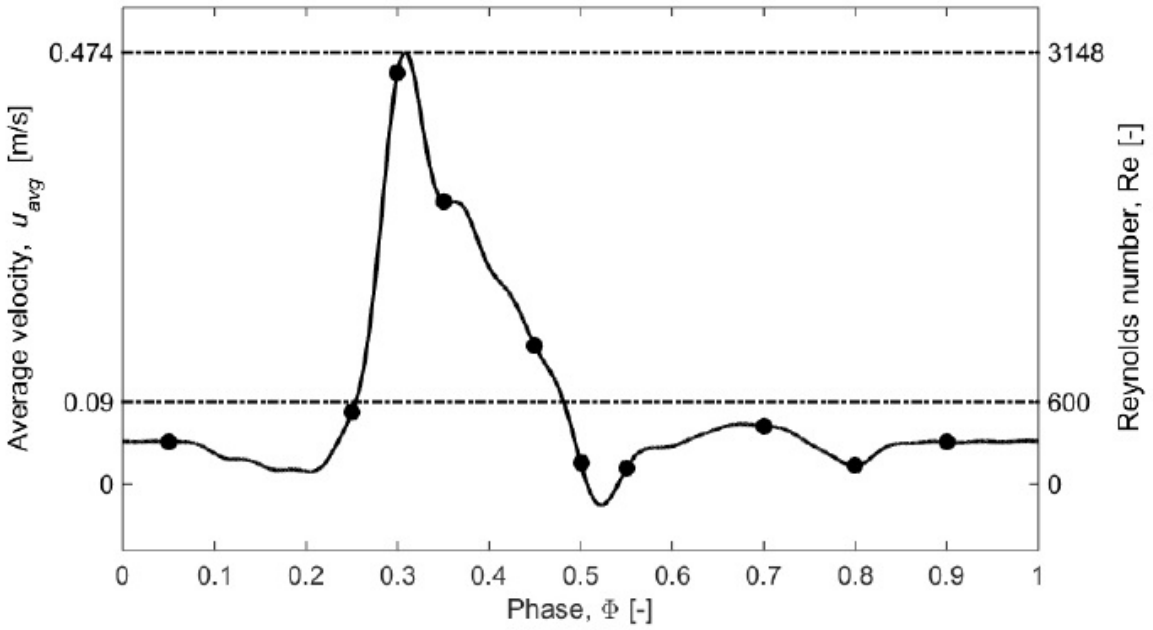

Figure 2.2: Mills' inlet velocity profile adapted for mean Re = 600. The bulk velocity is plotted against the phase within a cycle wherein phase Φ = time/time period. The black markers are the phases at which data is frequently exported for visualisation purpose. Reproduced from [25]

.

The cardiac cycle, as depicted in the above figure, can be split up into two parts: the systole and the diastole. During the systole, blood is ejected into the aorta. Systole can further be subdivided into two parts: systolic acceleration and deceleration. The phases from $\phi = 0.2$ to the peak flow rate phase $\phi = 0.32$ is the systolic acceleration. At the end of systolic deceleration, there is a small amount of backflow at the inlet. Thus, flow reversal is inherently present in the velocity profile. During the diastole, the heart is filled with blood and no blood is ejected. Hence, the velocity is constant and of small magnitude during the diastole.

2.3.4. Expansion Ratio (ER)

The ratio of the aneurysm diameter to the healthy aorta diameter is known as the expansion ratio (ER). While deciding the aneurysm diameter for investigation, it is important to choose physically realistic values for the simulations. Schumacher et al [26] collected data of 242 AAA patients regarding aneurysm diameter, aneurysm length, healthy aorta diameter among other parameters. Their data gives an average value of healthy aorta as 22 mm and 48 mm for the aneurysm diameter. The healthy aorta

diameter is directly adopted from the data of Schumacher et al as 22 mm. Keeping diagnosis and surgery thresholds in mind, 3 expansion ratios, 1.5, 2, and 2.5, are tested in this study which result in the aneurysm diameters to be 33 mm, 44 mm, and 55 mm, respectively.

2.3.5. Expansion Angle (EA)

The steepness of the aneurysm expansion is referred to as the expansion angle. While the effect of expansion angle on the flow field has not been widely investigated, it has the potential to play a significant role. One need not look further then the flow over a backward facing step (BFS) to see the importance of expansion angle. Flow over a BFS and flow through an AAA share a major common aspect: both involve divergent regions wherein the fluid flow is subjected to an adverse pressure gradient which can lead to flow separation and formation of recirculating regions or vortex shedding at high enough Reynolds numbers. Numerous researchers [27–31] have investigated flow over a BFS and tried to understand the impact of expansion ratio, expansion angle, Reynolds number and pulsatility of flow. Mushyam et al [30] undertook a comprehensive numerical study of the effect of varying expansion angle of the BFS in the laminar flow regime. They noted that the length of the recirculating region was fairly independent of the expansion angle but the drag coefficient had an inverse relationship to the expansion angle. Obviously, we should not expect exact similarities in the flow field of this thesis with that of the BFS since the geometry in this work is axisymmetric but some qualitative similarities can perhaps be expected.

Regarding the value of expansion angles to be investigated, it was decided to keep the upper limit as $45°$ since an expansion angle higher than that would seemingly cause an unphysical amount of stress concentration at the expansion. Thus, 3 expansion angles are investigated: $15°$, $30°$ and $45°$. From a basic knowledge of solid mechanics it can be expected that the stress in the divergent portion of the AAA at higher expansion angles will be higher due to the relatively higher stress concentration. Combining the 3 expansion angles with the 3 expansion ratios, a total of 9 cases are obtained.

2.4. Blood Properties

Blood is a heterogeneous mixture and is chiefly comprised of blood plasma and blood cells. It is basically a suspension of red blood cells, white blood cells and platelets in blood plasma. Like with most other suspensions, blood is a non Newtonian fluid which means that the shear stress is not linearly proportional to the velocity gradient. This implies that the viscosity of blood is not a constant but rather depends on a plethora of factors such as shear rate, temperature, hematocrit and vessel diameter. Determining the precise viscosity after taking all the factors into consideration is a very complex problem and is better suited as a separate rheological study. Nonetheless, ignoring the non Newtonian behaviour of blood, as is done in this thesis, needs to be justified.

The temperature dependence of viscosity can safely be ignored since blood temperature of a healthy person has a constant value of 37 degree Celsius. Hematocrit refers to the volume percent of red blood

cells in blood and unless a person is sick, its value too can be assumed to be constant. Viscosity also depends on the diameter of the blood vessel as demonstrated by Fåhræus and Lindqvist [32]. Basically, when the vessel diameter is 0.5 mm or smaller, red blood cells tend to occupy the center of the vessel which results in almost pure plasma occupying the space near the wall. Since the plasma viscosity is lower than the whole blood viscosity, overall viscosity in such small vessels decreases, as illustrated in figure 2.3. Since the aortic diameter is significantly higher than 0.5 mm, the vessel diameter plays no role in determining the viscosity of blood.

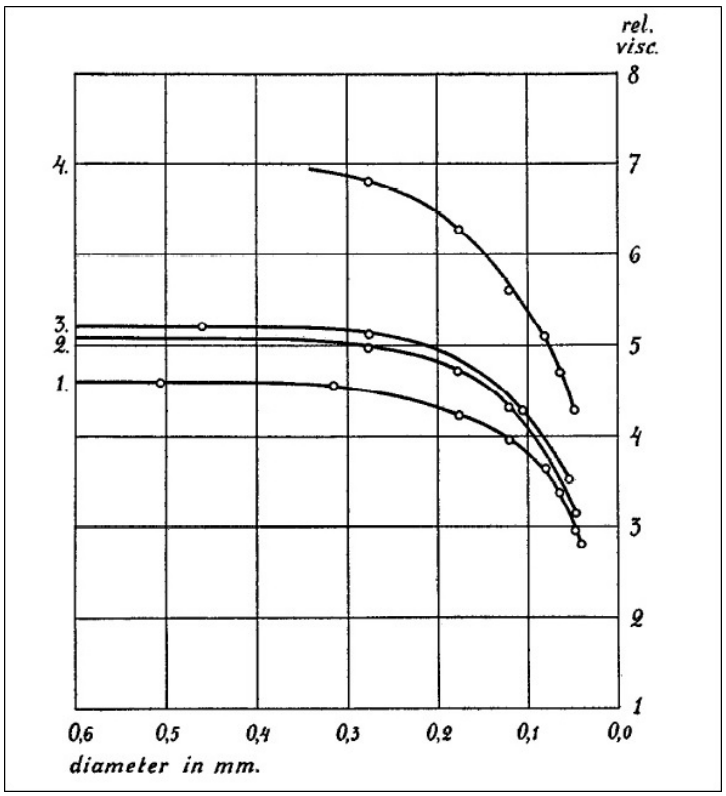

Figure 2.3: Viscosity dependence on vessel diameter. Viscosity attains a constant value for all vessel diameters more than 0.5 mm. Thus, the aorta is not affected by the Fåhræus and Lindqvist effect. Reproduced from [32]

The most important factor affecting blood viscosity is the shear rate. Figure 2.4 shows the dependence of blood viscosity on the shear rate for different hematocrit values. It is clearly evident from the figure that at high shear rates ($> 100\ s^{-1}$), viscosity attains a constant value. Shear rates in the aorta near the wall are approximately $300\ s^{-1}$ and thus, the viscosity can be assumed to be a constant value there. The velocity gradients, and thus the shear rates, are lower near the center of the aorta implying a higher viscosity at the center than at the walls. Thus, the non Newtonian nature of blood is not strictly negligible even in the aorta but can be approximated as Newtonian with reasonable confidence. Infact, assuming blood to be a Newtonian fluid in the aorta is a rather standard assumption in this field of study.

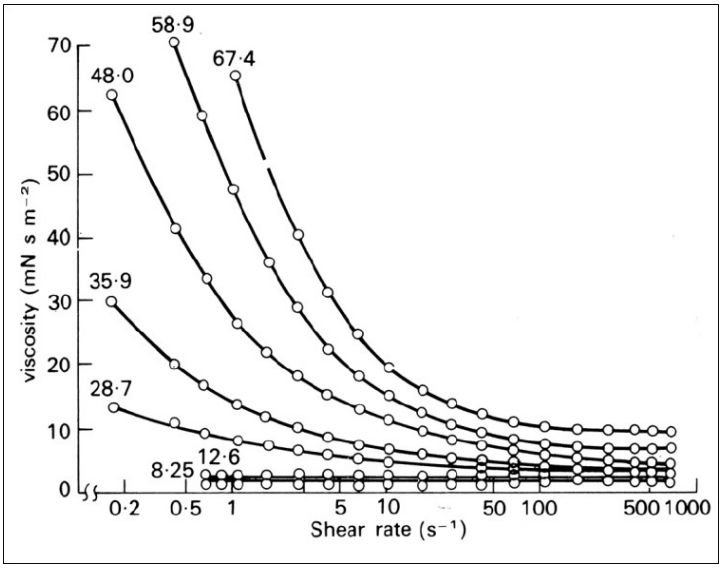

Figure 2.4: Viscosity dependence on shear rate for different hematocrit values. The curves level out at shear rates higher than 50 - 100 s^{-1}. Reproduced from [33]

The viscosity and density value for the simulations done in this thesis are taken from the computational inter laboratory study on simulating blood flow in a medical device. This project was undertaken by the United States Food and Drug Association (FDA) [34]. Blood density is taken as 1056 kg/m^3 and the (dynamic) viscosity is taken as 0.0035 Pa.s for all the simulations in this study.

2.5. Output Variables

The flow field can be described with the help of many variables. Since the main objective of this thesis is to investigate turbulence, velocity and vorticity are quantities of utmost importance. Also, to identify areas of high Oscillatory Shear Index (OSI), the wall shear stress needs to be analysed. A short explanation of all such relevant output variables/ parameters is given in the following sub sections.

2.5.1. Velocity

Usually, in statistically steady turbulent flow fields, the velocity variables are expressed using the Reynolds decomposition. The aim of doing so is to be able to understand the contribution of the fluctuations and compare it against the mean flow contribution. Since blood flow is periodic and hence unsteady in nature, a slightly different decomposition is used to analyse such pulsatile flows. This decomposition comprises a periodic and a fluctuating component [20].

$$\mathbf{u}(\mathbf{x}, t) = \mathbf{u}_\phi(\mathbf{x}, \phi) + \mathbf{u}'(\mathbf{x}, t) \tag{2.21}$$

The first term on the RHS of equation 2.21 is the periodic or phase averaged velocity component. This is computed by averaging the same phases in different cycles and hence depends on position and the

phase ϕ of the cycle. Thus, the phase averaged component is equivalent to the mean component in the Reynolds decomposition. The second term represents the fluctuations in the velocity field and depicts deviation from the periodic component or what is different from cycle to cycle at the same phase. Thus, this term depicts the turbulent fluctuations. Such a decomposition is used for other variables of interest also such as vorticity and kinetic energy.

2.5.2. Kinetic Energy

As explained in the previous section, kinetic energy can also be decomposed in two components: periodic kinetic energy and turbulent kinetic energy. The general formula to calculate kinetic energy at any position **x** and time *t* is

$$KE(\mathbf{x},t) = \frac{1}{2}\left(u^2(\mathbf{x},t) + v^2(\mathbf{x},t) + w^2(\mathbf{x},t)\right) \tag{2.22}$$

To calculate periodic kinetic energy (PKE), periodic velocity components from equation 2.21 need to be substituted in equation 2.22. Similarly, to calculate turbulent kinetic energy (TKE), the components signifying turbulent fluctuations in equation 2.21 need to be susbstituted in equation 2.22. As explained in section 3.1, temporal acceleration/deceleration and spatial acceleration/deceleration can affect the transition to turbulence threshold and can cause fluctuations to increase. Plotting contours of TKE is an effective way to visualise turbulence in the aneurysm.

2.5.3. Vorticity

Vorticity is a vector field (usually denoted by $\vec{\omega}$) that can formally be defined as the curl of the velocity vector. It basically represents the local flow rotation. The vorticity equation can be obtained by taking the curl of the Navier Stokes equation.

$$\frac{D\omega_i}{Dt} = \omega_j \frac{\partial u_i}{\partial x_j} + \nu \frac{\partial^2 \omega_i}{\partial {x_j}^2} \tag{2.23}$$

Before analysing the above equation, it is important to note that the equation is in the Einstein notation. The vorticity equation describes how the vorticity changes with respect to a reference frame that moves along with the fluid element. The second term on the RHS of 2.23 signifies the diffusion of vorticity due to viscosity. The first term denotes the stretching/ tilting of vorticity. Vortex stretching is the key mechanism through which larger eddies lose energy to smaller eddies in the energy cascade process. Thus, vorticity stretching and hence vorticity, is an essential and fundamental aspect of turbulence [35].

2.5.4. Pressure & Wall Shear Stress

Despite the plethora of factors involved in the formation and progress of an aneurysm, its rupture is ultimately due to material failure. An aneurysm ruptures when the stresses acting on the arterial wall

exceed the arterial tissue strength, as shown by Vorp in his review article [6]. Thus, one can now see the shortcoming of the maximum diameter criterion; it is not necessary that the weakest tissue be present at the location of the maximum diameter. Although shear stress is important in computing hemodynamic parameters such as the oscillatory shear index (OSI), Vorp asserted that flow induced shear stress is five to six orders of magnitude lesser than the pressure/ stretch induced wall stress. This strongly suggests that rupture would take place at locations of maximum normal stress and not maximum shear stress. A comparison of pressure and shear stress can be found in appendix A.5.

2.5.5. Oscillatory Shear Index

The Oscillatory Shear Index (OSI) is a hemodynamic parameter that gives an idea as to how much the wall shear stress vector changes in magnitude and direction. Mathematically, it is formulated as

$$OSI(\mathbf{x}) = \frac{1}{2}\left[1 - \frac{\frac{1}{T} \mid \int_0^T \tau_w(\mathbf{x}, t)dt \mid}{\frac{1}{T}\int_0^T \mid \tau_w(\mathbf{x}, t) \mid dt}\right] \tag{2.24}$$

wherein τ_w is the wall shear stress (WSS) vector and T is the time period of one cardiac cycle. The above definition of OSI can be computed with one cardiac cycle or with multiple cardiac cycles. In case of a purely uni-axial flow wherein the velocity vectors near the wall don't change direction, the numerator and denominator in the above formula will be equal and the OSI will have a value of zero. Similarly, for a flow that completely reverses its direction at a point, the numerator will be zero leading to an OSI value of 0.5. Thus, OSI values lie between 0 and 0.5 with 0.5 depicting maximum fluctuation of the WSS vector and 0 depicting minimum. Many researchers have tried to use the OSI to identify regions of potential rupture in numerical computations since a high OSI region implies high fluctuations near the wall (arterial tissue) which lowers the strength of the tissue. Since the chief objective of this thesis is to study turbulence, the OSI is not analysed extensively. In this study, the OSI is chiefly used to test sufficient temporal convergence of simulations. This is further explained in chapter 4.

3

Computational Modelling

Since an analytical solution of pulsatile flow in an AAA is not possible, the Navier Stokes equations are discretised over the entire flow domain that transforms them from a set of partial differential equations to algebraic equations which can then be solved numerically on a computer. This is the core principle of Computational Fluid Dynamics. In order to carry out a numerical simulation, the problem needs to be set up in a way that can be understood by the computer. This broadly involves creating the flow domain geometry and meshing it, applying appropriate boundary conditions and selecting optimal numerical schemes to solve the system of algebraic equations. In this thesis, ANSYS Fluent, a commercial finite volume code, is used as the solver. The following sections explain the steps taken and choices made in regards to setting up the simulation.

3.1. Governing Equations

The set of equations that represent the physics involved in a problem are known as the governing equations. For problems of fluid dynamics, the Navier Stokes equation and the continuity equation are the governing equations. Both these equations can be obtained from the general transport equation. The conservative/ Eulerian form of the transport equation for a general conserved property (per unit mass) ϕ, can be defined as

$$\frac{\partial(\rho\phi)}{\partial t} + div(\rho\phi\vec{u}) = div(\tau\nabla\phi) + S \tag{3.1}$$

where τ is the diffusion coefficient and S represents any additional source term.

The finite volume formulation of equation 3.1 is obtained by taking its integral and then applying the Gauss divergence theorem.

$$\frac{\partial}{\partial t}\left[\int_V \rho\phi dV\right] + \int_A \vec{n}.(\rho\phi\vec{u})dA = \int_A \vec{n}.(\tau\nabla\phi)dA + \int_V SdV \tag{3.2}$$

In equation 3.2, $\vec{n}$ is the normal vector to the differential surface element dA. The conserved properties per unit mass in the transport equation, ϕ, are unity (mass conservation), directional velocity components (momentum conservation) and specific energy (energy conservation). Since temperature is not a variable in this study, the energy conservation equation is not solved; only the mass conservation and momentum conservation equations are solved in the finite volume formulation in ANSYS Fluent. For an incompressible, Newtonian fluid such as in this thesis, and with no external sources, the mass (continuity) and momentum (Navier Stokes) conservation equations can finally be written as

$$\frac{\partial\rho}{\partial t} + \nabla.(\rho\vec{u}) = 0 \tag{3.3}$$

$$\rho\left[\frac{\partial\vec{u}}{\partial t} + \left(\vec{u}.\vec{\nabla}\right)\vec{u}\right] = -\vec{\nabla}p + \mu\vec{\nabla}^2\vec{u} \tag{3.4}$$

Investigation of turbulence is the primary objective of this thesis. Usually, an appropriate turbulence model is used in simulations since it is computationally expensive to resolve all the flow scales. But turbulence modelling also introduces assumptions into the problem that may or may not be strictly valid. Thus, it was decided to not use any turbulence model in this thesis and rather make the mesh fine enough to be able to capture nearly all the flow scales.

3.2. Geometry Creation

Idealised axisymmetric AAA (4A) models are generated in SolidWorks 2015, a commercial CAD software. As explained in the previous chapter, three cases each of expansion ratio and expansion angle are investigated for a total of 9 cases. Since the 4A geometries are axisymmetric, a cosine curve is used to represent the shape and curvature of all the geometries. A cosine curve allows a smooth transition from the healthy aortic diameter to the aneurysm diameter thus preventing sharp kinks in the geometry that can cause unwanted disturbances in the flow. Table 3.1 gives an overview of all the cases.

AAA Stage	Expansion Ratio (ER)	Healthy Aorta Diameter (mm)	Aneurysm Diameter (mm)	Expansion Angle (EA)
Diagnosis	1.5	22	33	$15°, 30°, 45°$
Intermediate	2	22	44	$15°, 30°, 45°$
Surgical	2.5	22	55	$30°, 45°$

Table 3.1: Overview of Cases

Since both, the expansion ratio (ER) and expansion angle (EA), are varied, the total length of a 4A model is kept constant to keep the number of cases under control. The total length of the aneurysm in a 4A geometry is taken to be 100 mm. This value is decided keeping physicality of AAAs in mind. Also, a length of 100 mm allows the aneurysm part of a 4A geometry to be modelled by straight cylindrical parts in between a divergent and a convergent region which is almost always the case in real AAAs.

Apart from the aneurysm length, the inlet and outlet length need to be decided to complete the entire flow domain. A sufficient amount of inlet length needs to be given for the flow to develop and mimic the actual velocity profile in the human aorta. An insufficient outlet length can cause unphysical flow reversal at the outlet. A simulation in a straight cylindrical pipe is done to check the development length of the flow. From this simulation, an inlet length of 5 times the inlet diameter is chosen. Detailed results of this validation are presented in the next chapter. The outlet length too is chosen to be 5 times the inlet diameter as it is deemed sufficient enough for no back flow to occur; this is verified from previous research articles [24]. The general geometrical aspects common to all 4A geometries are illustrated in figure 3.1.

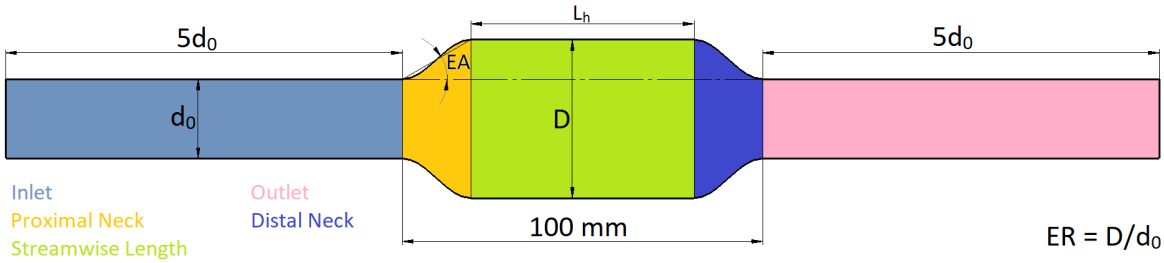

Figure 3.1: General geometric aspects and terminology used to characterise a 4A geometry. L_h refers to the streamwise length of an AAA and its role is discussed in detail later in section 5.3. The inlet and outlet length of $5d_0$ and the total aneurysm length as $100mm$ is common to all the 4A geometries; L_h varies from case to case depending on the value of ER and EA.

Due to the total length of the aneurysm being fixed at 100 mm, it is not possible to have a 4A geometry with an expansion ratio of 2.5 and an expansion angle of $15°$ such that the total length of the aneurysm is 100 mm or less. Thus, this case is not simulated and the total number of cases is 8. An illustration of all the 8 cases can be found in appendix A.7.

3.3. Mesh Generation

Meshing is the process of discretising the entire flow domain into several smaller volumes on which the system of algebraic equations are solved. ANSYS ICEM CFD 16.1 is used to mesh all the geometries in this thesis as it allows complete control over all the meshing parameters thereby resulting in high quality meshes. Since no turbulence model is used in this study, it is extremely important to create a mesh that can sufficiently capture most, if not all, of the flow scales. At the same time, a very, very fine mesh will result in an extremely high number of cells that will lead to an impractical simulation time. Thus, a balance is necessary between the two requirements.

3.3.1. General Element Size

The Kolomogorov scales are an indication of the smallest scales associated with any flow. Theoretically, to resolve the smallest flow scale numerically, the mesh cell size should not be more than the Kolmogorov length scale, which can be expressed as

$$\eta \sim d_0 Re_p^{-3/4} \tag{3.5}$$

where η is the Kolmogorov length scale, d_0 is the healthy aorta diameter and Re_p is the peak Reynolds number over the entire cardiac cycle. Since η scales inversely with the Reynolds number, the peak Reynolds number Re_p is chosen to capture the smallest flow scales over the entire cycle. Creating a mesh in accordance with the Kolmogorov length scale results in extremely expensive and practically infeasible simulations. As explained by Moin and Mahesh [36], the Kolmogorov scale is too stringent a limit and the length scale by which most of the dissipation occurs is usually bigger than the Kolmogorov length scale. One such length scale is the Taylor microscale, which can be expressed as

$$\lambda \sim d_0 Re_p^{-1/2} \tag{3.6}$$

From equations 3.5 and 3.6, it can clearly be seen that η and λ both decrease as the Reynolds number of the flow increases thereby increasing the computational cost of the simulation. This is the chief reason as to why direct numerical simulation (DNS) of large Re flows is still not possible even today. The peak Re in this study is $\approx$ 3150 which results in $\eta \approx 0.05$ mm and $\lambda \approx 0.4$ mm. Since $\lambda \approx 10\eta$, the general element size is decided in accordance with the Taylor microscale. Further, a mesh independence study is done to test two general element sizes: λ and 1.2λ. It was found that a general element size of 1.2λ (0.48 mm) is sufficiently fine; results from both the sizes for comparison are shown in the next chapter.

3.3.2. Near Wall Element Size

The elements near the wall need to be refined in order to capture the high wall gradients. Blasius skin friction relation for internal flows is used as the starting point to get a rough idea of the first near wall cell size.

$$C_f = 0.079 Re_p^{-1/4} \tag{3.7}$$

The wall shear stress can then be estimated as

$$\tau_w = \frac{1}{2} C_f \rho u_p^2 \tag{3.8}$$

The wall friction velocity u_τ can be written as

$$u_\tau = \sqrt{\frac{\tau_w}{\rho}} \tag{3.9}$$

Finally, the dimensionless wall unit y^+ can be defined as

$$\frac{y^+}{y} = \frac{u_\tau \rho}{\mu} \tag{3.10}$$

To be able to resolve the flow gradients near the wall, this dimensionless wall unit y^+ should be around 1. Substituting this in 3.10, we can obtain the value of y which is nothing but the distance of the first cell from the wall. For $Re_p \approx 3150$, this distance turns out to be $\approx$ 0.09 mm.

In deciding both, the general element size and the near wall cell size, the peak Reynolds number is used. This is a very conservative estimate as the peak Re is significantly higher than the mean Re. Thus, even if the estimations are based on approximate relations such as the Blasius relation, they are accurate enough to capture most of the flow dissipation throughout the cardiac cycle.

3.3.3. Meshing Technique

Hexahedral cells/ bricks are used to mesh the entire domain so that cells can be orthogonal in the wall normal direction. As explained in section 3.3.2, the elements near the wall need to be refined. Hexahedral cells allow the refinement of grid without large face skewness. ANSYS ICEM CFD 16.1 is used to carry out the meshing for all the cases since its 'blocking' feature easily allows users to create hexahedral grids. Once a geometrical feature has been assigned a block, its mesh characteristics can be changed in an independent fashion from the rest of the blocks to yield a highly customised mesh. Thus, if one part of the geometry is rectangular and the other part is circular, blocking allows the mesh to be aligned with the surface curvature of the respective sub parts. Further, blocking also allows for certain regions of the mesh to be selectively refined (near wall region) or coarsened (sufficiently downstream region). In ICEM CFD, it is also possible to use O grids with the blocking technique. An O grid significantly reduces the face skewness of the mesh elements that make up the corners of a circular surface such as a cylinder. Figure 3.2 depicts the face of a cylinder meshed with hexahedrals but without the usage of an O grid.

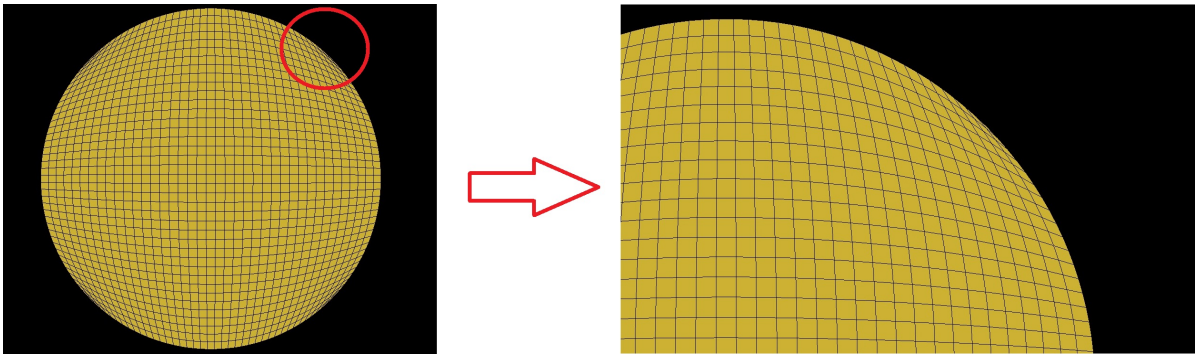

Figure 3.2: Hexahedral Mesh without O Grid. Absence of O grid leads to extremely skewed elements near the corners of the cylindrical surface (zoomed in region)

The face skewness of the elements along the curvature of the cylinder can clearly be seen. Such extreme skewness can cause cross diffusion and poses a very high chance to compromise the accuracy of the solution. This can be avoided by using O grids, as illustrated in figure 3.3.

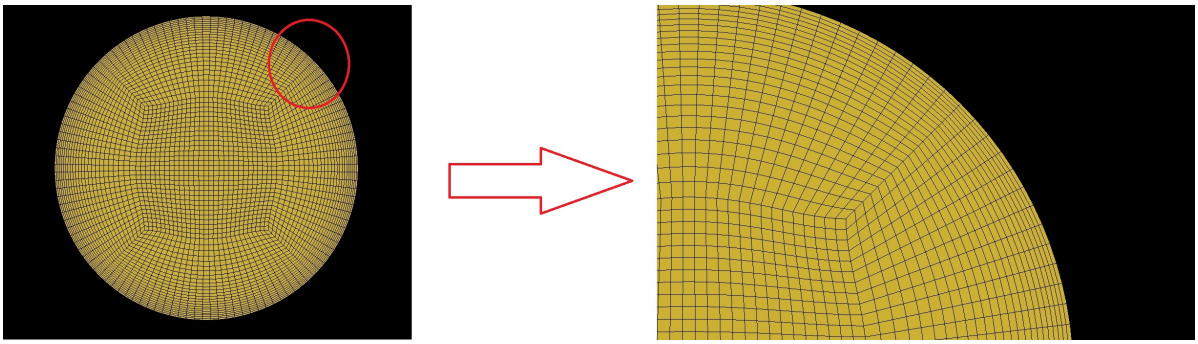

Figure 3.3: Hexahedral Mesh with O Grid. Corner elements no longer have face skewness but are instead wall normal

From figure 3.3, it can easily be seen that the face skewness is no longer present. Also, since the near wall elements are now wall normal, inflation (refinement) in the near wall region can be very easily implemented by changing the O grid block parameters. As explained earlier, the first near wall element size is 0.09 mm. A geometric mesh law is applied to the O grid block edge that is associated with inflation near the wall. A geometric ratio of 1.01 and 1.06 is set in the inlet/outlet region and in the aneurysm, respectively. A total number of 40 nodes define the inflation layer and in combination with the geometric ratio, the inflation layer seamlessly blends into the mesh elements in the bulk region. The aneurysm part of the flow domain is meshed with a uniform spacing law with a general element size of 0.48 mm. As for the cylindrical outlet and inlet regions, geometric mesh law is again used. For the inlet, the elements at the inlet face are $\approx$ 1.5 mm but are then reduced in a geometric fashion to the general element size of 0.48 mm for a seamless connection to the aneurysm region. For the outlet, the same law is applied but in a reverse fashion.

Across all the cases, the inlet and the outlet cylindrical parts are identical. Thus, the mesh generated in these parts is also identical in all the cases. But the aneurysm part of every geometry is different which leads to small differences in the general mesh element size despite keeping the first cell size from the wall constant for all the cases. Depending on the case, the total number of cells vary approximately between 4.5 million and 9.8 million.

3.4. Boundary Conditions

3.4.1. Inlet

It is common practice in numerical simulations to explicitly define a fully developed profile at the inlet face to avoid the computational cost of allowing the flow to develop over a long inlet length. Doing this for pulsatile blood flow is not so straightforward due to the temporal variation in the flow. Thus, the velocity profile in this case has two components: a spatial function and a temporal function.

$$u(r,t) = f(t)g(r) \tag{3.11}$$

To obtain the spatial variation, a comparison with the analytical Womersley profiles is necessary. The Womersley number (α) for all the simulations in this thesis is 16.9. As shown in the previous chapter, at high values of α, such as in this case, the spatial variation of the velocity profile is considerably different from the parabolic shape usually obtained in steady pipe flow. The Womersley profiles due to a simple sinusoidal pressure gradient for $\alpha = 16.9$ are illustrated in figure 3.4.

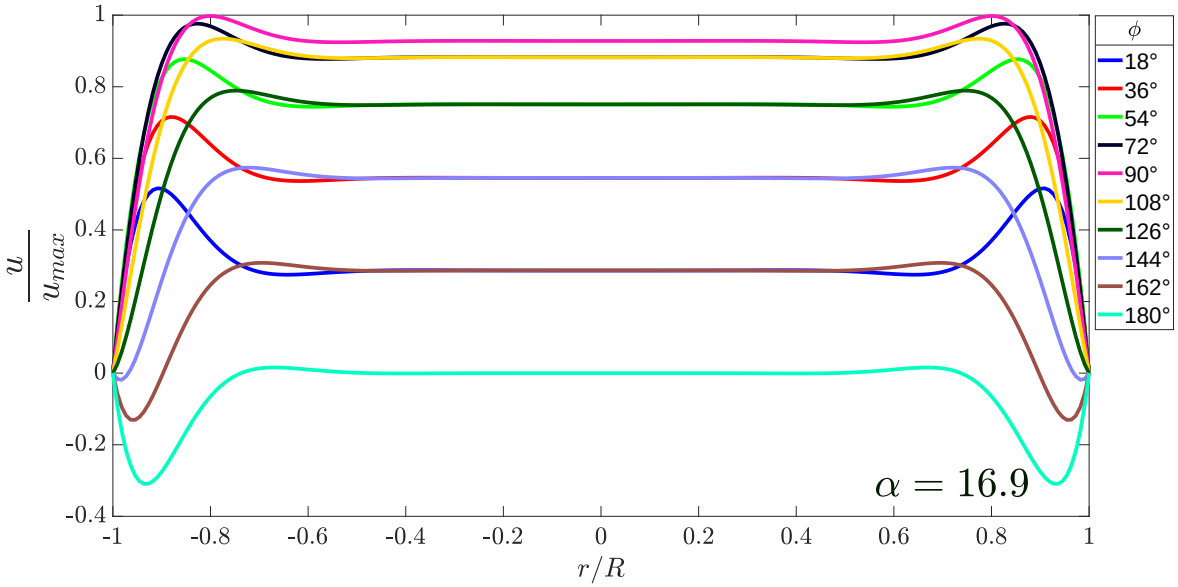

Figure 3.4: Womersley profiles for for $\alpha = 16.9$ due to a simple sinusoidal pressure gradient. Significant deviation from a parabolic profile can be observed at such a high value of α. The profiles for phases after 180 degrees upto 360 degrees have been omitted since they are simply opposite of the profiles for phases 18 to 180 degrees

From the figure, the deviation from a parabolic profile can be easily seen. Of course, the pressure gradient in blood flow is more complex than a simple sinusoidal pressure gradient but a qualitative similarity can be expected between the two and hence it is safe to conclude that for $\alpha = 16.9$, the profile will be considerably flat in the center. Thus, a power 10 function is used to depict the spatial variation of the velocity profile in this thesis. Equation 3.11 can now be written as

$$u(r,t) = f(t)\left[1 - \left(\frac{r}{R}\right)^{10}\right] \tag{3.12}$$

where R is the radius of the inlet and r is the distance from the center to the concerned point. The spatial variation is formulated as above in accordance with the no slip wall boundary condition. It is then believed that the power 10 profile will soon resemble (over a short inlet length) the actual spatial profile found in the aorta. To determine the temporal variation, we need to formulate the function in accordance with a couple of facts: the total flow over a cycle should be equal to the actual amount of blood flow in a cardiac cycle and the flow rate $Q(t)$ should resemble the flow rate in the abdominal aorta as closely as possible. To formulate the flow rate variation in the abdominal aorta, the best possible way is to actually measure the flow rate. Mills et al [23] measured the blood pressure and velocity waveforms in several patients through cardiac catheterization at several locations in the arterial tree including the abdominal aorta. The obtained flow rate waveform, adapted for a mean Re of 600, is illustrated in figure 3.5.

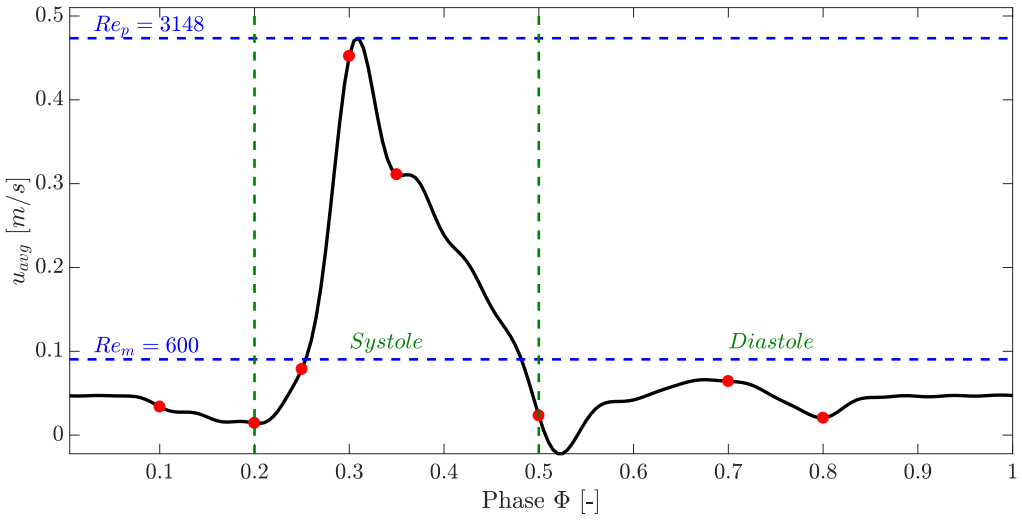

Figure 3.5: Mills' time dependent velocity waveform adapted for mean Re = 600. The plot shows the variation of the bulk velocity against the phases of the cardiac cycle. The red markers are the phases at which data is visualised in this thesis. Adapting Mills' waveform for a mean Re of 600 results in a peak Re of nearly 3150.

Such a time dependent velocity waveform can be represented mathematically as a Fourier series comprised of sines and cosines. It is then implemented in ANSYS Fluent through C program subroutines called user defined functions (UDF). Fluent has the capability to implement boundary conditions through a UDF and thus the velocity waveform is directly loaded as the inlet boundary condition. The Fourier series representation of the waveform is

$$Q(t) = \frac{a_0}{2} + \sum_{n=1}^{\infty} a_n cos(\omega_n t) + \sum_{n=1}^{\infty} b_n sin(\omega_n t) \tag{3.13}$$

wherein a and b are the Fourier coefficients and ω_n is the multiplication of the fundamental frequency with the harmonic n. Although equation 3.13 is an exact equation, Tim van Kruchten [25] showed in his work that 19 harmonics are sufficient to give a smooth, nearly identical velocity waveform as depicted in figure 3.5. For 19 harmonics, 3.13 can be re-written as

$$Q(t) \approx M_0 + \sum_{n=1}^{19} M_n cos(\omega_n t + \phi_n) \tag{3.14}$$

where M_n is the amplitude of the cosines and ϕ_n are the corresponding phase shifts. The value of these parameters is borrowed from Tim's thesis [25] and can be found in appendix A.1. The Mills waveform depicted in figure 3.5 was originally obtained for a mean Re ≈ 300. Thus, to adapt the waveform for a mean Re of 600, a factor of 2 needs to be multiplied to equation 3.14.
The average velocity over the entire face of the aorta can be defined as

$$u_{avg}(t) = \frac{Q(t)}{A} = \frac{Q(t)}{\pi R^2} \tag{3.15}$$

This is the spatial average and not the temporal average and thus, is a function of time. Henceforth, the term 'average' is used to describe any kind of spatial average and the term 'mean' is used to describe any kind of temporal average. Similarly, 'max' is reserved for the spatial maximum and 'peak' for the temporal maximum. $f(t)$ can be written using u_{max} in equation 3.12. Since u_{avg} can be easily computed from equation 3.15, it is desirable to express equation 3.12 in terms of u_{avg}. To do so, a relation between u_{max} and u_{avg} is derived as follows.

$$u_{avg}(t) = \frac{1}{A} \iint u_{max}(t) \left[1 - \left(\frac{r}{R}\right)^{10}\right] r dr d\theta = \frac{5}{6} u_{max}(t) \tag{3.16}$$

$$u_{max}(t) = \frac{6}{5} u_{avg}(t) \tag{3.17}$$

Substituting relation 3.17 and 3.15 in equation 3.12 gives the complete expression for the spatio-temporal dependence of velocity

$$u(r,t) = \frac{6}{5}\frac{Q(t)}{\pi R^2}\left[1 - \left(\frac{r}{R}\right)^{10}\right] \tag{3.18}$$

The expression derived above is implemented through a UDF on the inlet face. The velocity obtained from 3.18 is in the streamwise direction. Hence, the x component of velocity is calculated at every point and every time step from the UDF loaded into ANSYS Fluent. Usually, only the streamwise velocity component is non zero at the inlet since the flow is uni-axial initially. Since investigation of turbulence is the primary objective of this thesis, the inlet flow is perturbed in the perpendicular direction to the streamwise direction. This is done to induce early transition of flow as it is widely observed that pipe flow transitions at a much lower Re in experiments than in numerical simulations due to the inherent imperfections and disturbances present in experiments. As for deciding the optimal amount of perturbation, Peixinho et al [37] observed that a 0.1% perturbation gives similar numerical results as compared to the experiments for a gradual expansion pipe flow with an expansion angle of $26.57°$. Keeping in mind the imperfect geometry of an actual human aorta and the general disturbances created due to various activities, a value of 1% of the average velocity at each time step is deemed to be a reasonable perturbation for this thesis. Thus the complete velocity vector at the inlet can be written as

$$\vec{\mathbf{u}}(\vec{\mathbf{x}},t) = u(r,t)\hat{\mathbf{i}} + (0.01u_{avg})\hat{\mathbf{k}} \tag{3.19}$$

3.4.2. Outlet

At the outlet face, a pressure outflow boundary condition is used. The gauge pressure at the outlet is set to be zero. Since the operating pressure for all the cases is the atmospheric pressure, setting a zero gauge pressure at the outlet is equivalent to cutting the aorta and exposing it to the atmosphere. However, since the pressure drop across the aneurysm is the only variable of interest, such a boundary condition is acceptable.

3.4.3. Walls

The arterial walls are assumed to be rigid in all the cases simulated. Thus, the usual no slip boundary condition is applied at the wall.

3.5. Simulation Settings

ANSYS Fluent gives a choice of using either a pressure based or a density based solver. The pressure based solver is intended for incompressible low speed flows while the density based solver is intended for high speed compressible flows [38]. Since blood flow in this thesis is modelled as incompressible, it is natural to choose the pressure based solver. As for pressure velocity coupling, the Pressure Implicit

with Splitting of Operators (PISO) scheme is used for all the cases as it is highly recommended for unsteady simulations due to its stability even when working with a skewed mesh and a large timestep [38].

3.5.1. Discretization Schemes

As mentioned in section 3.1, ANSYS Fluent is a finite volume solver. Thus, value of ϕ in equation 3.2 is stored at the cell volume center. But ϕ is also required at the cell volume faces for the convection terms. To obtain the value at cell faces, the value from the cell center is interpolated. This interpolation can be done via numerous spatial discretization schemes. In this thesis, a second order central differencing scheme (CDS) is chosen so as to reduce the risk of false diffusion, which is generally the case with upwind schemes. As for the temporal discretization, a second order implicit time marching scheme is chosen as implicit schemes are unconditionally stable for all time step sizes [39].

3.5.2. Solver Settings

Unsteady simulations are carried out to simulate pulsatile blood flow. As mentioned in section 3.1, no turbulence model is used in this study. Thus, viscous 'laminar' Navier Stokes equations are solved in Fluent. A constant time step of 4 ms is used for all the cases. Thus 200 time steps constitute one cardiac cycle of 0.8 seconds. A time step of 4 ms results in a maximum Courant number of $\approx$2 at the peak velocity in the cardiac cycle; through most of the cycle it is less than 1. A time step of 4 ms also allows for easy export of data every tenth time step which results into 20 data exports for every cardiac cycle. The convergence criteria for the continuity as well as the momentum equations was set to 0.001. A maximum of 40 iterations are done at every time step to achieve convergence. In general, convergence is easily achieved (within 20 time steps) throughout the cycle except the few phases leading upto the peak systole wherein the convergence criteria only reached as low as 0.005. Apart from the convergence criteria, it is always a good idea to monitor a physical parameter to check for convergence. The solution is said to be converged when the value of such a physical parameter stops changing or changes extremely little after a certain number of iterations. The total wall shear stress on the aneurysm is monitored in this study and it always reached a nearly constant value; even when the convergence criteria did not reach 0.001. Thus, at every time step, the computed solution is sufficiently accurate.

Every case was simulated on the Reynolds cluster of the Aero and Hydrodynamics group at TU Delft. Each case was simulated with 28 cores and depending on the case, the wall clock simulation time varied from one week to three weeks to simulate a total of 75 cycles.

3.6. Post Processing

For post processing, MATLAB 2017a is used instead of commercial software such as CFD Post or Tecplot. This is chiefly done to have complete control over the visualisation of variables and have access to all the data so that derived quantities such as the OSI and turbulent kinetic energy (TKE) can be easily computed. Data is exported in ASCII format since this allows data to be exported on desired planes and surfaces rather than the entire volume domain thus saving a tremendous amount of disk usage. Data is exported once every ten time steps or once every 40 ms. Thus, one entire cardiac cycle (800 ms) has 20 data files for every location of data export. As for the variables, velocity and vorticity components are exported in the XY (Z = 0) and ZX (Y = 0) plane. All three components of wall shear stress are exported on the aneurysm surface. The pressure value is also exported along the centerline of the aneurysm. Lastly, only the visualisation of vortex rings and related coherent structures is done in CFD post.

4

Validation

Before presenting the results of flow through an aneurysm, it is important to establish a baseline flow field to which the results of the aneurysmal flow field can be compared. In order to establish the baseline flow, flow through a healthy aorta is simulated. Quantities like turbulence intensity and OSI in various aneurysm geometries are compared against this baseline flow field. Apart from establishing a baseline flow field, this chapter presents an elaborate overview of the reasoning behind the decisions taken on particular matters such as the inlet flow development length and the mesh density.

4.1. Inlet Flow Development Length

The flow development length refers to the length after which gradients, apart from the pressure gradient, in the streamwise direction become negligible. Here the pressure gradient has a constant value that drives the flow forward. Thus, if x is the streamwise direction, then for any quantity ϕ (except pressure), $\partial\phi/\partial x = 0$. For pipe flow with a constant pressure difference imposed across its ends, this length can be easily calculated using any of the standard relations (depending on the flow regime) given in any basic fluid mechanics textbook such as [40] but equivalent relations for an oscillatory pressure difference are not easily available, even if the pressure difference is expressed as a simple single sinusoidal harmonic. As mentioned in the previous chapter, the inlet velocity waveform is defined with the help of 19 Fourier harmonics which implies that the pressure difference is also represented through a combination of 19 harmonics. Thus, to estimate the development length of such a pulsatile pressure gradient, a separate simulation is necessary.

Pulsatile flow in a straight cylindrical pipe of total length 300 mm is simulated in which the time dependent inlet velocity waveform is implemented through a UDF. At every 20 mm along the cylinder length, the streamwise velocity along the vertical line through the cylinder center is recorded. This is done for each of the 20 phases at which data was exported. Figure 4.1 depicts the velocity profiles of all the exported phases at various streamwise locations.

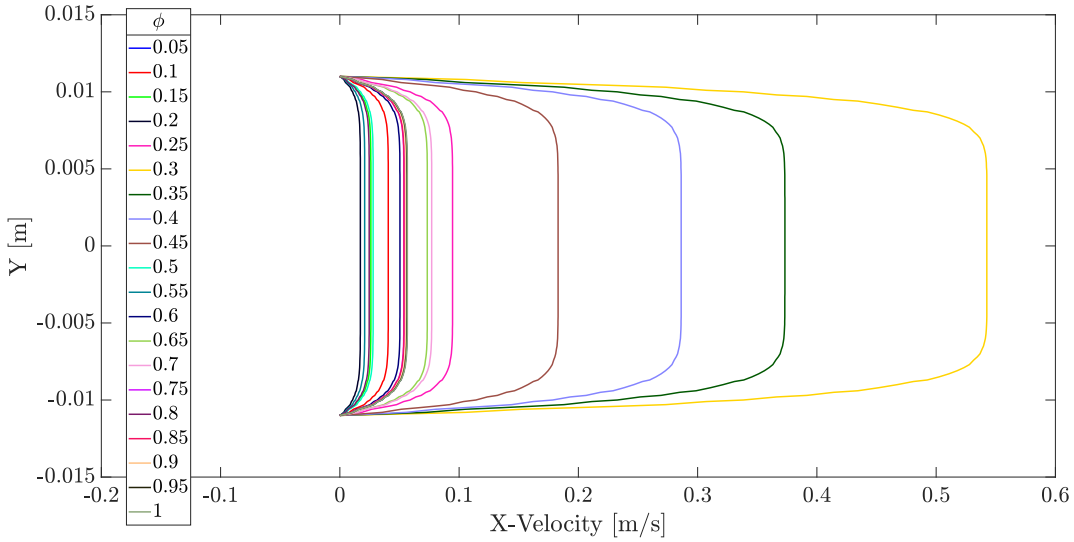

Figure 4.1: Streamwise velocity profiles for all the 20 exported phases at $x = 0$. None of the phases have backflow since only the power 10 profile is in effect at the inlet.

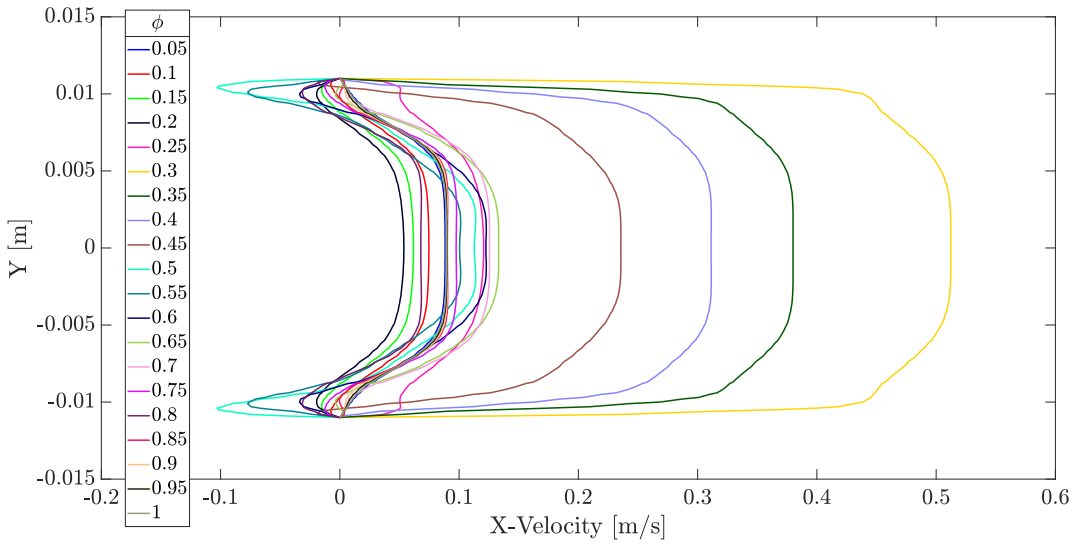

Figure 4.2: Streamwise velocity profiles for all the 20 exported phases at $x = 0.10m$. The profiles have developed considerably and backflow near the wall for some phases can be clearly seen.

At x = 0, where the UDF is imposed, the profile of all the phases is similar; flattened in the middle with no backflow near the wall. This is expected as the power 10 profile inherently does not have any backflow. Also, all the velocities are positive as none of the 20 exported phases include the small negative velocity

region in the inlet waveform. As the flow moves downstream, retrograde flow develops close to the wall and the general shape of the profile starts to change, as shown in figure 4.2. The flow can be called developed when there is negligible change in the velocity profile of every phase further downstream. In order to quantify this development, the difference between the velocity profiles at two successive locations is taken for every phase. The standard deviation of the velocity profile difference is computed per phase and then an average of such standard deviation is taken over all the phases. This procedure is done at every 20 mm along the length of the cylindrical pipe except at the inlet and outlet where the velocity profiles are a bit different due to the inlet and outlet conditions, respectively. The curve obtained as a result of this is shown in figure 4.3.

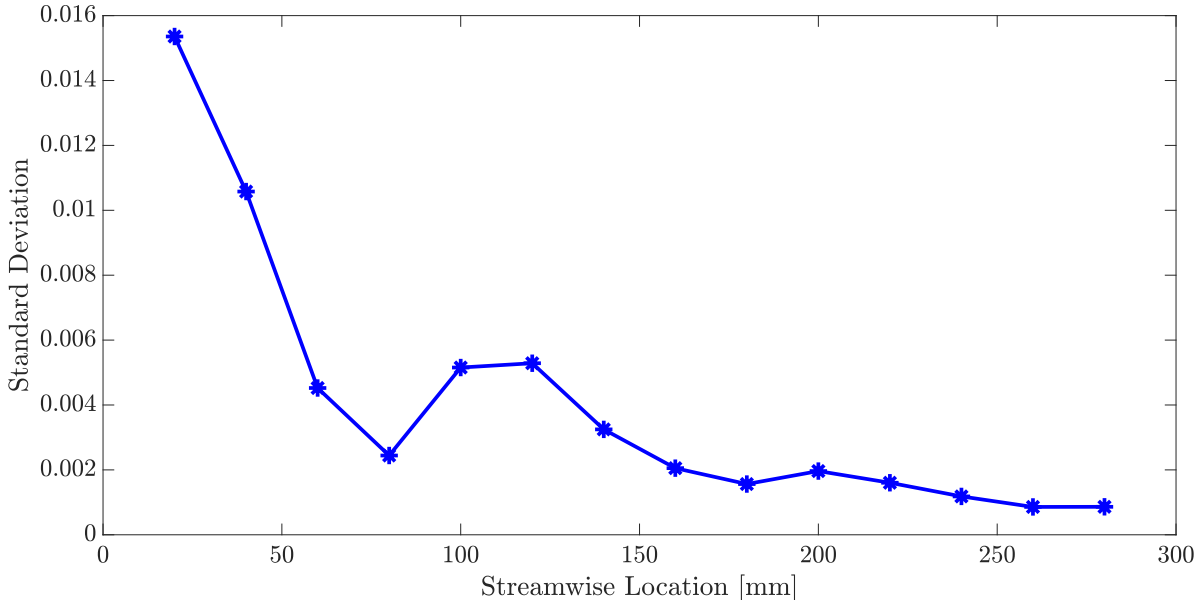

Figure 4.3: Mean (taken over all phases) of the standard deviation of the difference between axial velocity profiles at successive streamwise locations. Each data point represents the difference taken between velocity profiles at that location and the location 20 mm upstream of it.

Each data point in the above figure shows the mean standard deviation of the velocity profiles between the streamwise location at which it is plotted and the point 20 mm upstream of it. It can be seen from the figure that the major flow development takes place in the first 60 mm of the pipe length. Also, mean standard deviation of the velocity profile differences reduces to approximately 0.5% for the velocity profiles obtained at 100 mm and 120 mm. Thus, a length of 110 mm is decided as the inlet length; coincidentally this is equal to 5 times the inlet diameter.

4.2. Grid Independence Study

A grid independence study is done to ensure that the results obtained form the simulations are not dependent on the resolution of the mesh. Since no turbulence model is used in this study, it is even more important to verify that most of the dissipation scale is resolved with the chosen mesh resolution and

that a finer mesh resolution doesn't show a significantly different flow field. To test mesh independence, the aneurysm geometry with expansion ratio 2 and expansion angle 30° is simulated. Two hexahedral meshes are generated using the O grid blocking feature of ICEM CFD. The general element size of the first mesh is 20% larger (1.2λ) than the Taylor microscale and for the second mesh, it is equal to the Taylor microscale (λ). The Taylor microscale, as calculated in the previous chapter, is 0.4 mm for all the cases simulated. Thus, the general element size is 0.48 mm for the coarse mesh and 0.4 mm for the fine mesh. In both the meshes, hexahedral cells are a bit longer in the streamwise direction to keep the overall cell count at a reasonable limit. Although the general element size is different, near wall resolution is the same of both the meshes. Such a configuration results in the coarse mesh having a total of 5.26 million elements and the fine mesh being made of 9.35 million elements. Table 4.1 gives an overview of the mesh cell details of both the meshes.

Mesh	**General Element Size**	Δx	$\Delta y, \Delta z$	**Total Cells**
Coarse	0.48 mm	0.54 mm	0.48 mm	5.26M
Fine	0.40 mm	0.46 mm	0.40 mm	9.35M

Table 4.1: Overview of both the meshes

Due to the turbulent nature of the flow field, it is not possible to compare instantaneous quantities such as velocity or vorticity for conducting mesh independence. Instead, averaged quantities need to be compared after the initial transients have died out. The Oscillatory Shear Index (OSI) is one such hemodynamic parameter. The following figure shows the OSI distribution on the aneurysm wall for both the meshes at the end of 75 cycles.

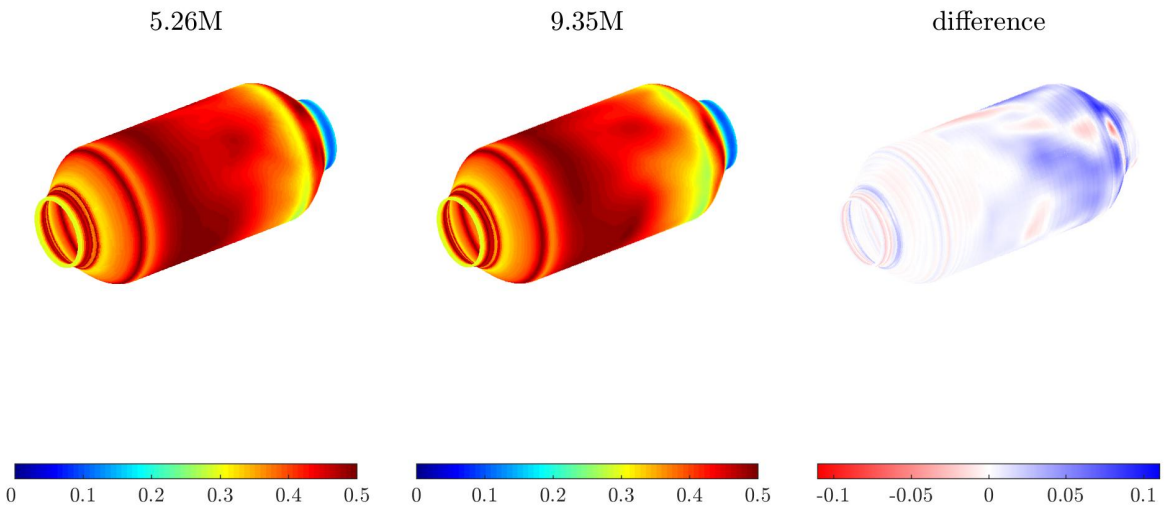

Figure 4.4: OSI distribution for the two meshes and the difference between them. The difference is calculated by interpolating values of the finer mesh onto the coarser mesh. The standard deviation of the local OSI differences so obtained is 1.86% of the total OSI difference scale which indicates a good agreement between the two meshes.

From the figure, it can be seen that there is good agreement between the two meshes qualitatively. To quantify the difference, the standard deviation of the local OSI differences between the two meshes is computed. To do so, OSI values of the finer mesh are interpolated on to the coarser mesh and then difference between the local OSI values is taken. This difference is illustrated in figure 4.6. The standard deviation of this local OSI difference is found to be 1.86% of the total OSI difference scale $(0.5 - (-0.5) = 1)$ and is deemed to be a reasonably small value. Thus, all the cases are simulated with the coarse mesh which leads to a general element size of 0.48 mm for all the cases.

4.3. Temporal Convergence

Fluctuations in the flow field is a trademark characteristic of turbulence. Due to such fluctuations, a certain number of cycles need to be simulated before meaningful data can be extracted from the simulations. One way to verify whether sufficient cycles have been simulated is to check the extent of reproduction of the flow field from cycle to cycle. It is then obvious that comparison of instantaneous quantities over different cycles does not make much sense since there will always be a small difference in the instantaneous values due to the turbulent fluctuations even after sufficient temporal convergence is achieved. Thus, the OSI, which is an averaged hemodynamic parameter, is analysed. Similar to the grid independence study, temporal convergence is tested on the aneurysm geometry with expansion ratio 2 and expansion angle 30°. For the calculation of OSI, the first 15 cycles are disregarded since the flow field transitions only after the first 15 cycles. Figure 4.5 illustrate the OSI distribution on the aneurysm surface after 30(n_{30}), 60(n_{60}) and 75(n_{75}) cycles (in addition to the disregarded initial 15 cycles) and the local OSI difference between them.

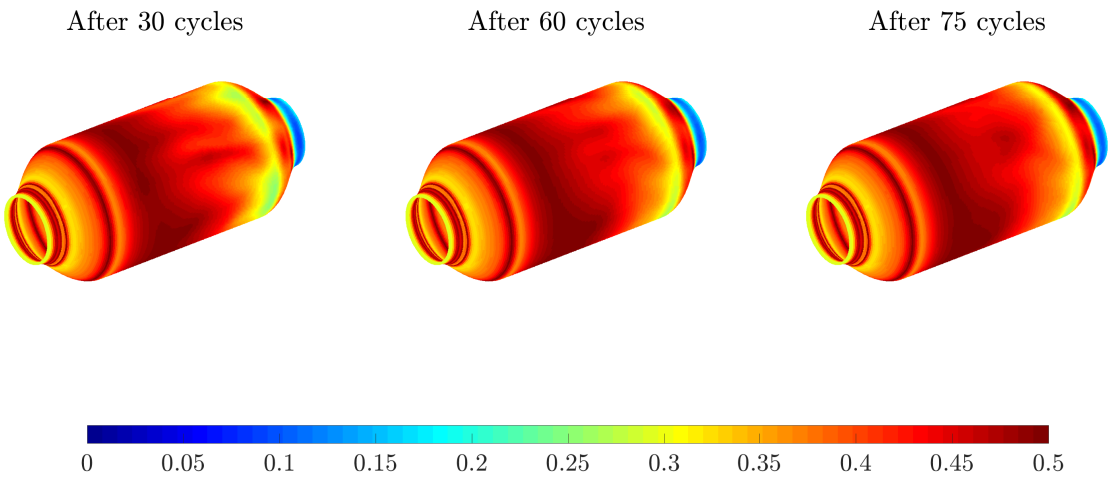

Figure 4.5: OSI distribution after 30, 60 and 75 cycles. Considerable difference exists at the distal end of the aneurysm after 30 and 60 cycles. This difference reduces to acceptable limits by the end of 75 cycles.

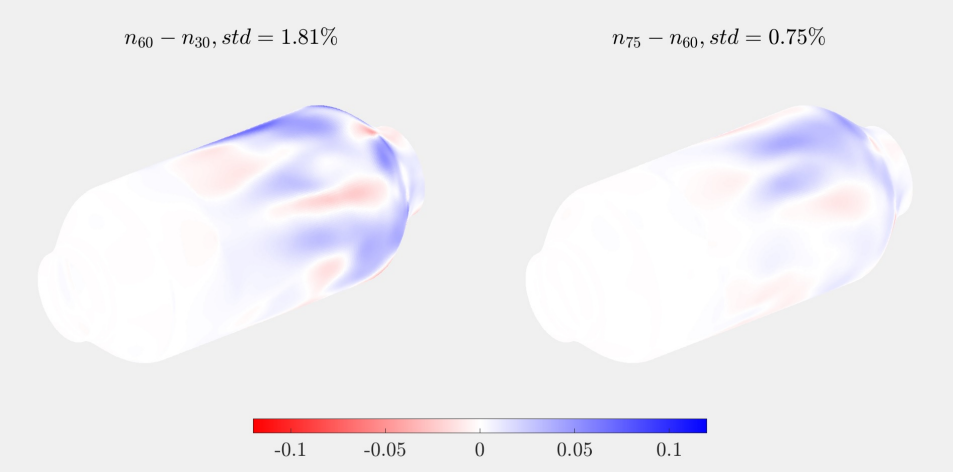

Figure 4.6: Difference in the OSI distribution for the distributions shown in 4.5. The standard deviation of the local OSI difference falls by more than half at the end of 75 cycles.

There is considerable difference in the OSI distribution between n_{30} and n_{60}. The difference can be quantified by calculating the standard deviation of the local OSI differences and equals 1.81% of the total OSI difference scale. However, n_{60} and n_{75} are in reasonable agreement. The standard deviation of the local OSI difference also decreases by more than half to 0.75%. To quantify the convergence behaviour of OSI with the number of cycles simulated, the standard deviation of the local OSI differences between consecutive number of cycles is plotted in 4.7. The standard deviation keeps decreasing with increasing number of cycles. After around 50 cycles, an oscillating behaviour can be observed. This can be thought of as an indicator of sufficient number of cycles simulated. Thus, the choice is made to simulate 60 cycles (and thus total 75 cycles) for all the aneurysm cases. Further, data from 60 cycles ($16^{th} - 75^{th}$) is taken to calculate phase averaged quantities for all the cases.

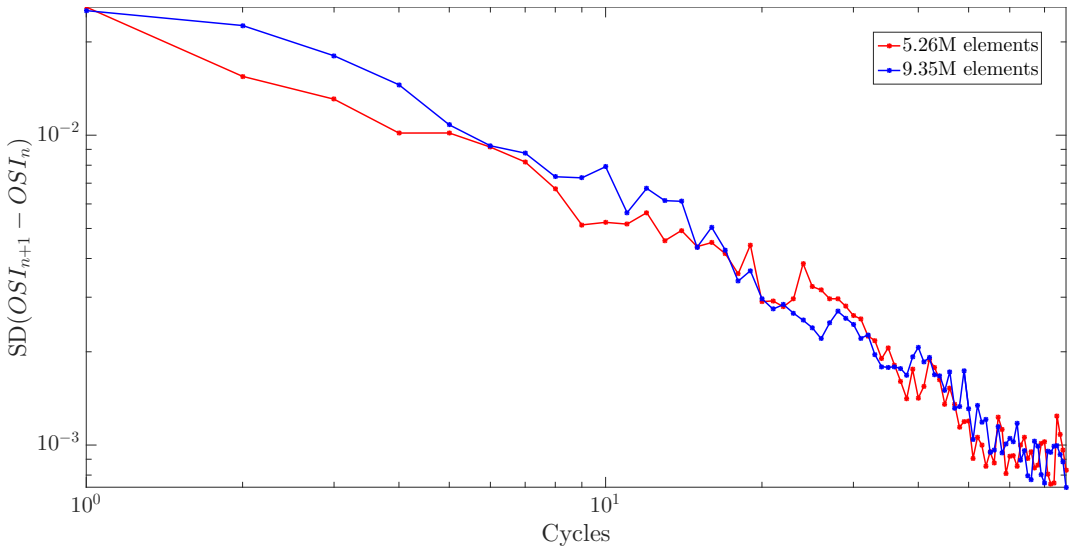

Figure 4.7: Standard deviation of the local OSI differences with increasing number of cycles. Every data point represents the standard deviation between the OSI distribution at the end of two consecutive cycles. The OSI is calculated by considering all the cycles simulated upto that point.

Simulations to test temporal convergence were done on both, the fine and the coarse mesh. For both the meshes, it took 75 cycles to attain the desired temporal convergence. Thus, refining the mesh did not have any effect on the temporal convergence. The behaviour of the standard deviation of the local OSI differences of the fine mesh is also plotted in figure 4.7 for easy comparison. From the figure, it is clear that 75 cycles are required for both the meshes. Since the OSI values also of both the meshes after 75 cycles are in good agreement as illustrated in figure 4.4, the choice to simulate 75 cycles on the coarse mesh for all the geometries is natural.

4.4. Healthy Aorta

To be able to understand the effect on the flow field due to an aneurysm, blood flow in a healthy aorta is simulated. This simulation, like all the aneurysm cases, is also done with a general mesh element size of 0.48 mm. The length of the healthy aorta is taken to be the same as the total length of the flow domain of the aneurysmal cases. From video clips of instantaneous vorticity contours, it is observed that the flow did not transition from the laminar regime and displays no fluctuations from cycle to cycle. Due to the small velocity perturbation in the z direction at the inlet, the flow field is not perfectly axisymmetric. This can be observed from the streamwise velocity contours in the XY plane and ZX plane, as shown in figure 4.8 and 4.9, respectively. Since no fluctuations are present, there is no need to simulate 75 cycles to obtain the desired temporal convergence. Also, the absence of fluctuations allows phase averaging to be done over a lesser number of cycles since the flow field is nearly identical from cycle to cycle; in this case it is done only over 10 cycles. The following figures depict various phase averaged quantities at selected phases.

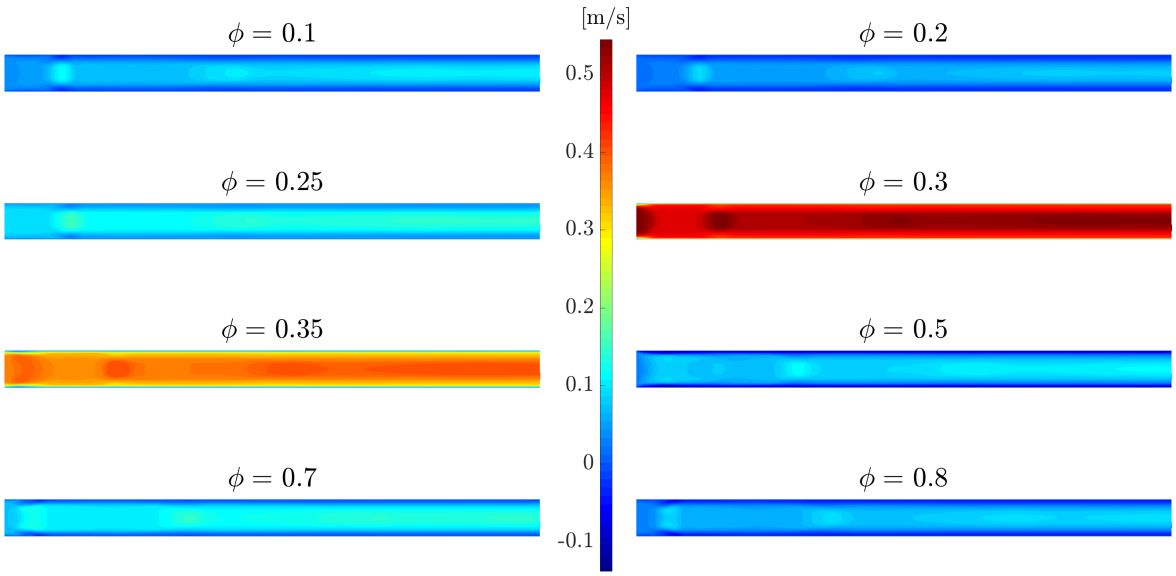

Figure 4.8: Phase averaged streamwise velocity contours in the XY plane (Z = 0) of a healthy aorta at selected phases. The flow field is rather symmetrical which strongly hints towards the absence of turbulence.

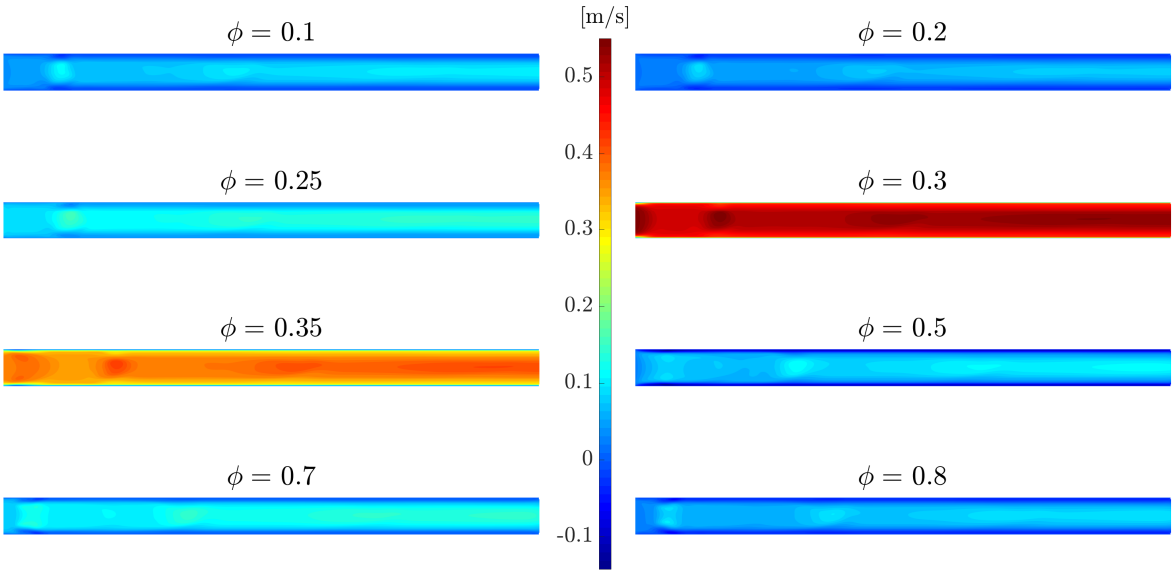

Figure 4.9: Phase averaged streamwise velocity contours in the ZX plane (Y = 0) of a healthy aorta at selected phases. Unlike the flow field in the XY plane, symmetry is absent in the ZX plane. This is due to the 1% velocity perturbation given in the positive z direction at the inlet. Precaution should be exercised to not interpret the absence of symmetry as the presence of turbulence. It should be remembered that for turbulence to exist, differences need to be present on comparing the same phase from cycle to cycle.

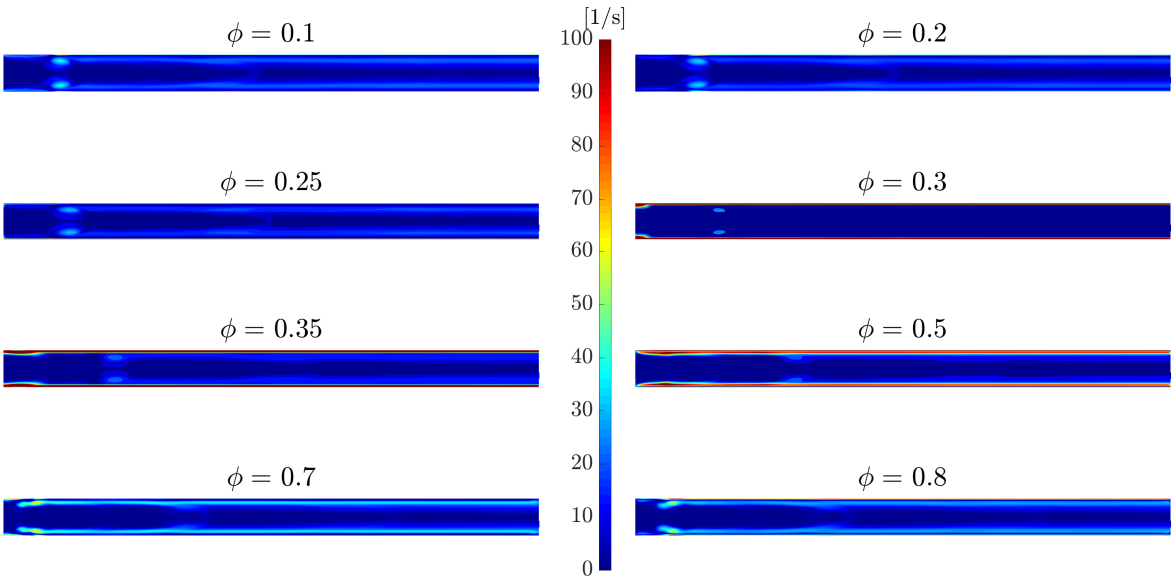

Figure 4.10: Phase averaged vorticity magnitude contours in the XY plane (Z = 0) of a healthy aorta at selected phases. The vorticity field, just like the velocity field, is symmetrical. The pulsatile nature of the flow causes the shear layer near the wall to roll up which leads to the formation of a vortex ring like structure. This occurs just after peak systole ($\phi = 0.7 - 0.8$) when the applied pressure at the inlet suddenly falls giving rise to an adverse pressure gradient in the aorta that causes shear layer to roll up near the arterial wall.

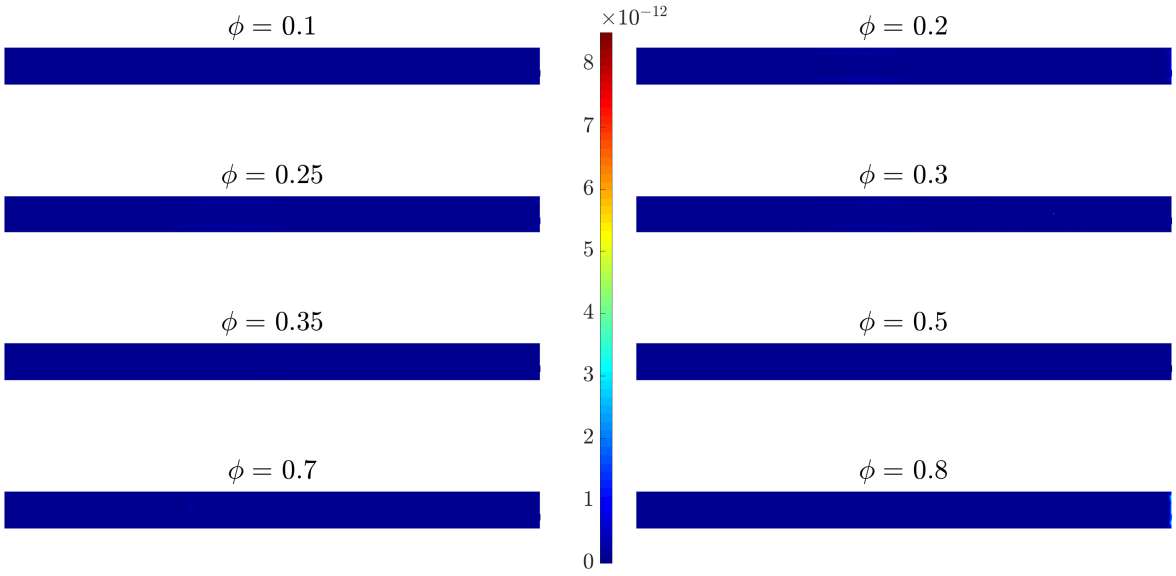

Figure 4.11: Phase averaged turbulence intensity in the XY plane at selected phases. As expected from the corresponding velocity contours, there is no turbulence in the healthy aorta throughout the cardiac cycle.

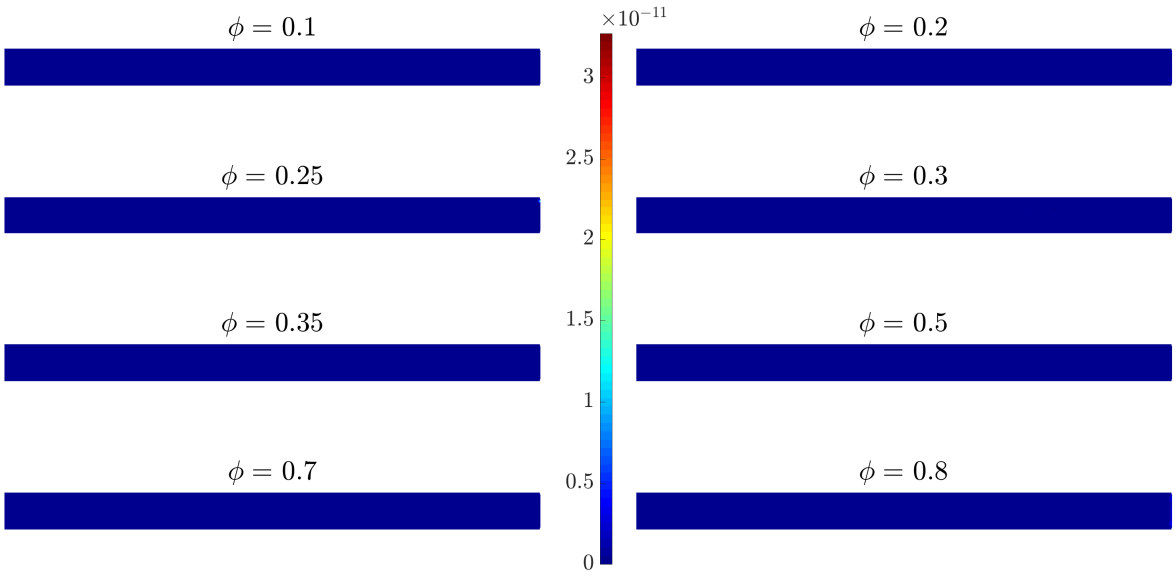

Figure 4.12: Phase averaged turbulence intensity in the ZX plane of a healthy aorta at selected phases. Even though the corresponding velocity contours were not symmetrical, there is still no turbulence present. This is due to the fact that the flow field is the same at every phase instant from cycle to cycle and thus there are no fluctuations at any phase within a cycle.

From the above figures, it is clear that the flow field is free from fluctuations and hence there is no turbulence present. Thus, it can be concluded that the pulsatile nature of blood flow, even with a small velocity perturbation at the inlet, is not sufficient to trigger turbulence. Another important quantity to visualise is the OSI. OSI visualisation in the healthy aorta provides a baseline OSI against which the OSI for the aneurysmal cases can be compared. Figure 4.13 illustrates the OSI distribution, calculated

over a period of 10 cycles, over a healthy aorta.

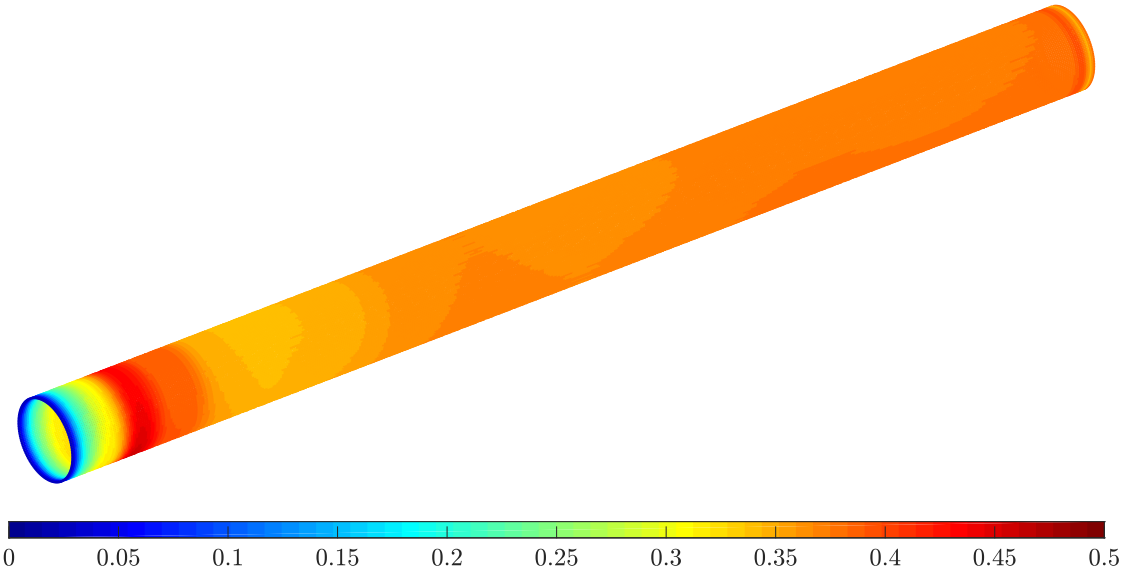

Figure 4.13: OSI distribution on the arterial wall of a healthy aorta. The average OSI is 0.36 which is a rather high value considering that the maximum possible value is 0.5.

At the entrance region, the OSI value is zero since flow is always uni-directional there at the exported phases. Further downstream, the OSI gradually increases which is expected as the flow starts developing. After the flow is developed, the OSI levels out around a value of 0.36. Keeping in mind the fact that the highest possible OSI value is 0.5, 0.36 is still a very high value for a healthy aorta flow. This is due to the temporal acceleration and deceleration associated with the pulsatile nature of blood flow that causes frequent change in the velocity direction near the aorta wall. Nonetheless, the average value of 0.36 should be kept in mind when interpreting results regarding the OSI of the aneurysmal cases.

4.5. Code Validation

Before starting with the simulation of the aneurysm cases, it is important to test if the choices made (as explained in the previous chapter) regarding various simulation aspects are representative of the actual physical process. Additionally, it is even more important to test if the CFD code used, in combination with the simulation choices made, is able to capture all the necessary flow physics occurring in an AAA. ANSYS Fluent is widely regarded to be the most commonly used software in an industrial environment but in particular situations such as flow through an AAA wherein the flow can transition to turbulence and display complex behaviour, its reliability needs to be established. As mentioned earlier, no turbulence model is used in this thesis and thus it is natural to test Fluent against a DNS study that has similar flow features to those expected in an AAA. Apart from flow features, it is desirable to select a study that has as many similarities as possible regarding general simulation aspects such as assumptions and boundary conditions. Keeping the above mentioned requirements in mind, the choice is made

to reproduce the article by Varghese et al [20] which presents results regarding the DNS of pulsatile stenotic flow. Stenosis refers to the condition in an artery in which the flow cross section decreases and then increases back to the original cross section. Both, stenotic and AAA flows, display transitional flow regime at a Reynolds number at which flow is otherwise usually laminar. The following are the common aspects between the article and the current work.

- Blood is assumed to be a Newtonian fluid.
- Arterial wall is assumed to be rigid and the artery cross section to be axisymmetric.
- Inlet flow is uni-axial.
- Mean Reynolds number over one cardiac cycle is 600.

Table 4.2 lists the differences in simulation aspects between [20] and this thesis.

Aspect	Varghese et al [20]	Current Work
Inlet Velocity Waveform	Sinusoidal	Physiological
Perturbation	Geometric	Velocity
Womersley Number	7.5	16.9
Peak Reynolds Number	1000	3150
Solver	Spectral Element	Finite Volume

Table 4.2: Difference in simulation aspects between [20] and this thesis

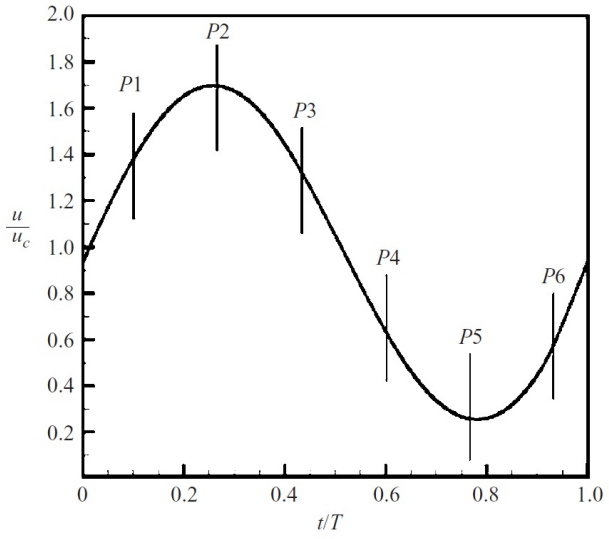

Figure 4.14: Time variation of the axial centreline velocity at the artery inlet in [20]. A sinusoidal waveform is superimposed on a mean flow. Data is ensemble averaged at the 6 phases marked in the figure (P1-P6). The centreline inlet velocity is normalized with u_c: the mean (cycle averaged) inlet centreline velocity. Reproduced from [20].

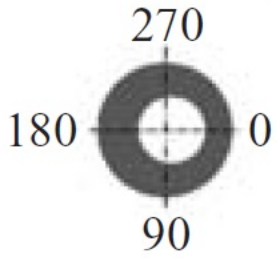

Figure 4.15: Cross sectional view (YZ Plane) of the angular locations at which axial wall shear stress along the length of the arterial wall are plotted in figure 23 in [20].

In the article [20], numerous plots are presented regarding various quantities such as velocity profiles, vorticity contours, time history plots etc. But for a comparison purpose, it is desirable to reproduce a plot that allows for easy comparison. Keeping this is mind, figures 22 and 23 from the article are reproduced here and a comparison of velocity profiles can be found in appendix A.6.

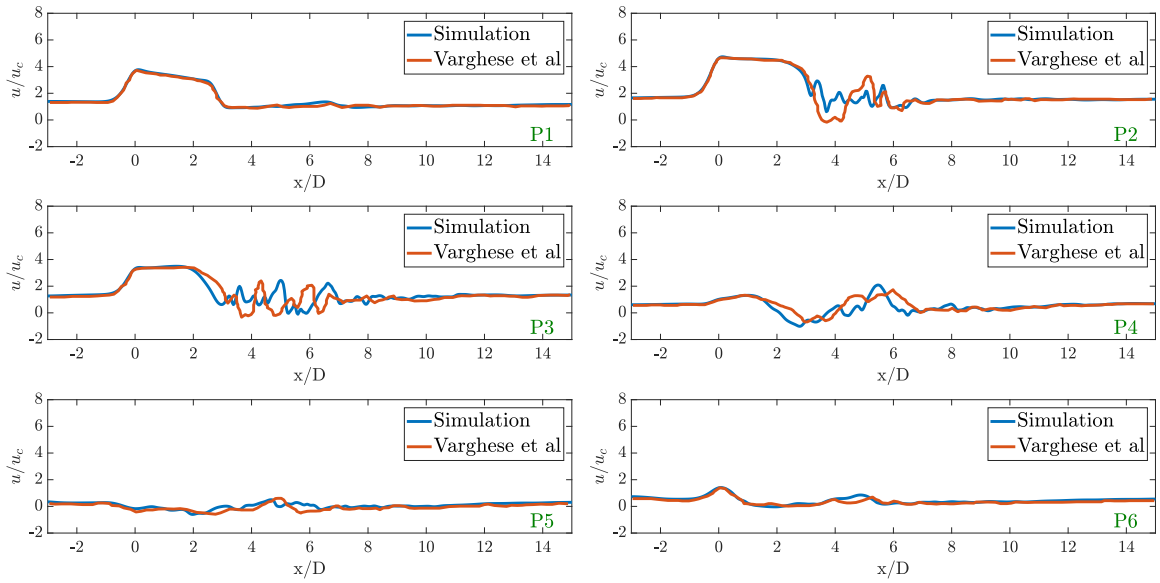

Figure 4.16: Figure 22 of [20] depicting the instantaneous streamwise centreline velocity at the 6 phases. The velocity is normalised with u_c. A good qualitative agreement can be observed at all the phases. During the deceleration phases (P3 - P5), a slight difference can be observed in the values but it is within reasonable limits.

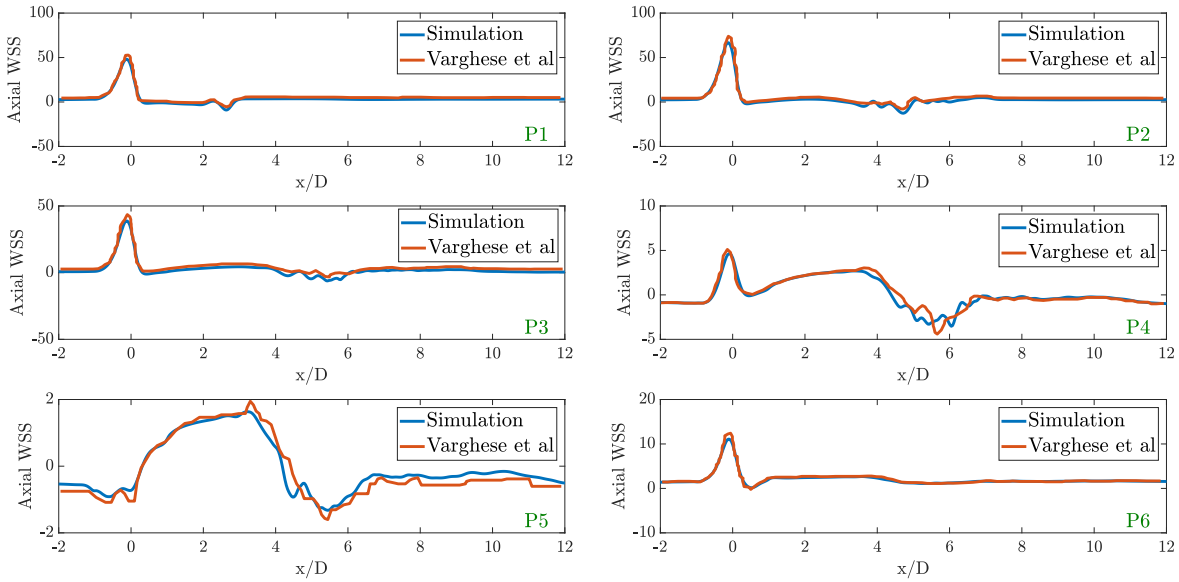

Figure 4.17: Figure 23 of [20] at the angular location of $0°$. The axial wall shear stress, normalised by the time averaged (over entire cycle) values upstream of stenosis, is plotted. A good qualitative agreement can be observed at each of the 6 phases. During the deceleration phases (P3 - P5) when the flow transitions from the laminar regime, a slight but reasonable difference in the values can be observed.

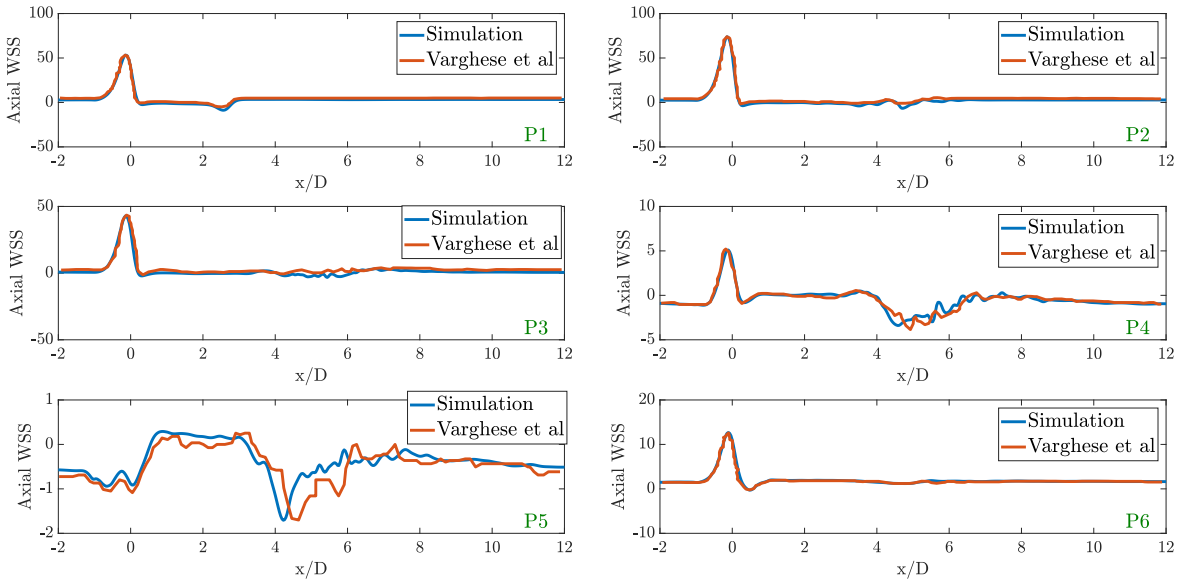

Figure 4.18: Figure 23 of [20] at the angular location of $90°$. The axial wall shear stress, normalised by the time averaged (over entire cycle) values upstream of stenosis, is plotted. A good qualitative agreement can be observed at each of the 6 phases. During the deceleration phases (P3 - P5) when the flow transitions from the laminar regime, a slight but acceptable difference in the values can be observed. Corresponding plot for the location at $270°$ is identical due to symmetry and hence skipped.

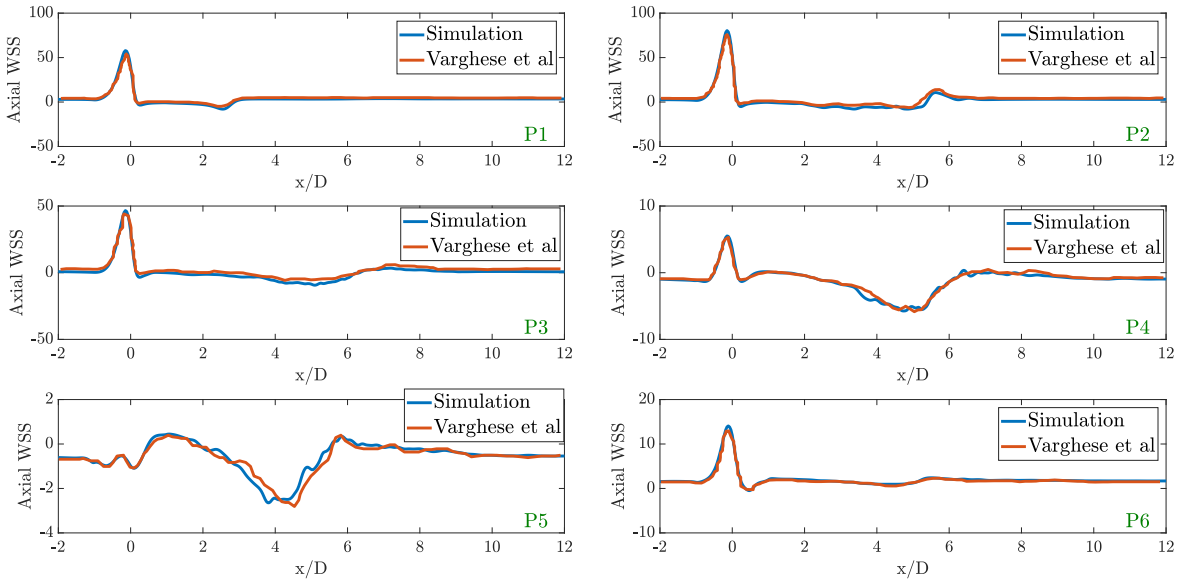

Figure 4.19: Figure 23 of [20] at the angular location of $180°$. The axial wall shear stress, normalised by the time averaged (over entire cycle) values upstream of stenosis, is plotted. A good qualitative agreement can be observed at each of the 6 phases. During the deceleration phases (P3 - P5) when the flow transitions from the laminar regime, a slight but reasonable difference in the values can be observed.

5

Results & Discussion

Simulation results are presented in this chapter. First, detailed results of velocity, vorticity, turbulent kinetic energy (TKE) and OSI are presented to get a general idea of the flow field. Such detailed results are presented only for one 4A geometry as doing so for all 8 geometries is redundant since the flow field across most of the geometries is qualitatively similar. If a 4A geometry displays any peculiar characteristic, it is discussed separately. Throughout this chapter, various 4A geometries will be referred to as cases and the following table summarises the geometric properties of all the cases.

Case	Expansion Ratio (ER)	Expansion Angle (EA)
Case 1	1.5	15°
Case 2	1.5	30°
Case 3	1.5	45°
Case 4	2	15°
Case 5	2	30°
Case 6	2	45°
Case 8	2.5	30°
Case 9	2.5	45°

Table 5.1: Overview of all the cases

Comparison across all the cases is done by plotting the behaviour of certain parameters, such as the OSI, to get an idea of the influence of geometric properties on the flow field. Finally, the cause of turbulent fluctuations is discussed.

5.1. General Flow Field Description

The flow field of every case is visualised through velocity, vorticity and TKE contours. In general, a vortex ring is generated at the expansion region or the proximal neck of the 4A geometry just after the peak systole i.e. when the applied inlet velocity decreases suddenly. The formation of the vortex ring can be thought of as a consequence of the near wall shear layer roll up and the subsequent separation due to the adverse pressure gradient in the aneurysm. Once formed, the vortex ring travels downstream along the length of the aneurysm. The total mass of fluid that the vortex ring transports with itself is referred to as a 'bubble'. An azimuthal instability develops on the ring that grows as the ring advects downstream. Depending on the geometry, the ring either breaks down into smaller vortices due to the azimuthal instability before it exits the aneurysm or it comes in contact with the contracting region near the aneurysm exit (also referred to as the distal neck) and then breaks down. Either way, breakdown of the vortex ring causes turbulence as the exact manner of breakdown is different from cycle to cycle which leads to a fluctuating flow field. Throughout this section, visualisation is carried out for case 5 i.e. for a 4A geometry with an expansion ratio of 2 and an expansion angle of 30°.

5.1.1. Velocity Contours

Figure 5.1 depicts the phase averaged streamwise velocity contours in the XY plane (Z = 0) at 8 selected phases (out of the total 20 exported) of the cardiac cycle. At the start of the cycle, a local high velocity region can be seen near the distal neck side of the aneurysm. This corresponds to the vortex ring generated from the previous cycle. Over the next few phases, the vortex ring passes through the aneurysm. From the velocity contours itself, it cannot be said for certain whether the ring breaks down

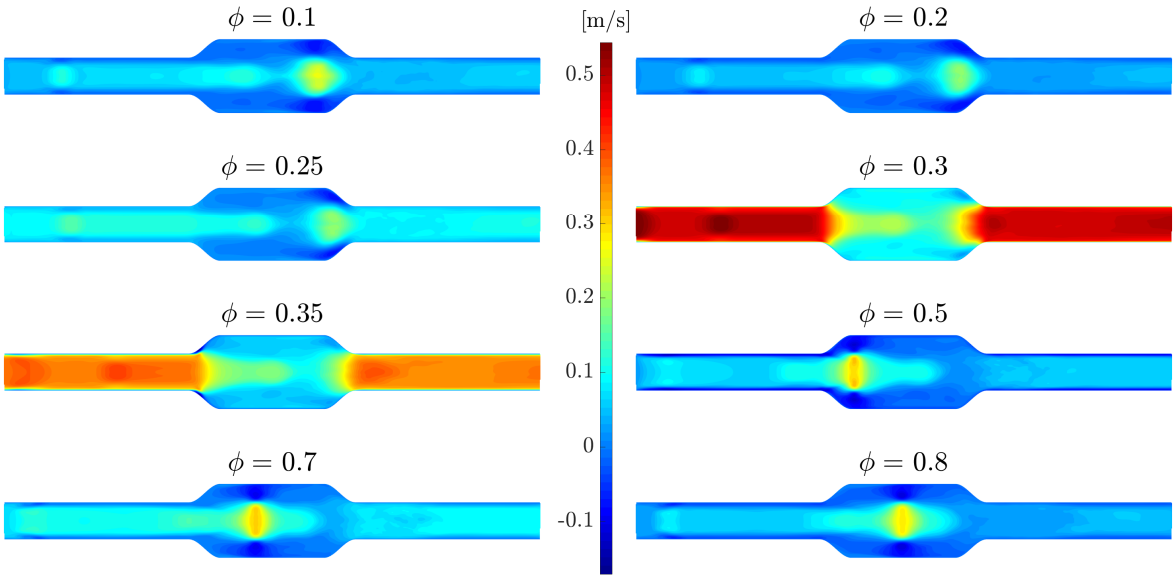

Figure 5.1: Phase averaged streamwise velocity contours at different phases (ϕ) in the XY plane. Retrograde flow can be seen surrounding the vortex ring bubble as it traverses the aneurysm.

before coming in contact with the convergent region of the aneurysm; vorticity contours are plotted in the next subsection for that purpose. The highest inlet and outlet velocity can be seen at ϕ = 0.3 which is the peak systole although due to the expansion in diameter, the flow velocity in the aneurysm region is lower in accordance with the continuity equation. Right after the peak systole, the inlet flow rate decelerates rapidly which leads to the shedding of a vortex ring, as evident at ϕ = 0.5. Over the next few phases, the vortex ring bubble advects downstream towards the exit region or the distal neck of the aneurysm. Retrograde flow can be observed near the wall around the vortex ring bubble which gives an idea of the sense of rotation of the fluid particles in the vortex ring. Looking at the retrograde flow pattern, it can be concluded that in the top half of the flow field the fluid particles rotate in the counter clockwise direction and in the clockwise direction in the bottom half of the field. Detailed aspects of the vortex ring bubble are explained in section 5.5.

5.1.2. Vorticity Contours

Figure 5.2 illustrates the phase averaged vorticity magnitude contours at various phases in the XY plane (Z = 0). Just after the peak systole at ϕ = 0.35, formation of a pair of vortices can be seen. This is actually a vortex ring but in a 2D plane it can be only be visualised as a vortex pair. The vortex ring is shed once every cycle just after the peak systole. The ring then advects downstream along the length of the aneurysm. By the beginning of the next cycle around ϕ = 0.1, the vortex ring approaches the distal neck of the aneurysm and starts breaking up into smaller vortices.

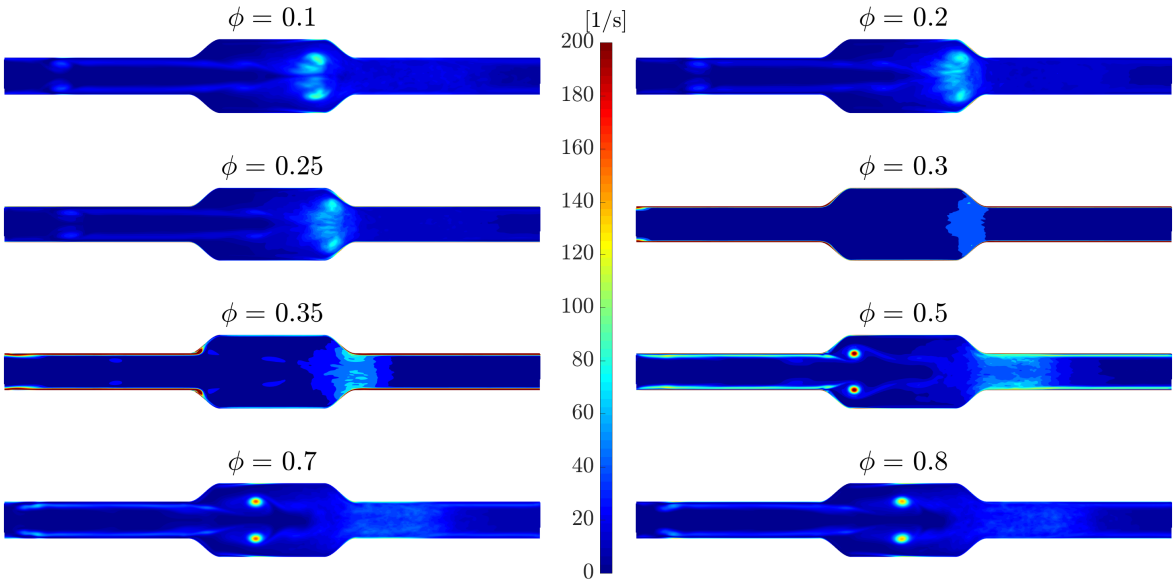

Figure 5.2: Phase averaged vorticity magnitude contours in the XY plane (Z = 0) at selected phases. The vortex ring is seen as a vortex pair in the planar contours (between ϕ = 0.5 and ϕ = 0.8) that breaks down near the exit region of the aneurysm.

For now, it is sufficient to say that the influence of the wall and interaction with the remnants of the flow field from the previous cycle causes the vortex ring to break up into smaller eddies, as evident from the

contour plot at ϕ = 0.25. The break up is initiated by the development of an azimuthal instability that grows as the ring advects downstream. For case 5, the development and progress of the azimuthal instability is illustrated using an iso surface computed via the Q criteria [41] in figure 5.3. Section 5.5 provides a detailed explanation regarding the stability and the break up process of the vortex ring. On interacting with the remnant eddies of the previous cycle, the now distorted vortex ring breaks down into smaller eddies. Meanwhile, a new vortex ring is generated and the entire cycle repeats again.

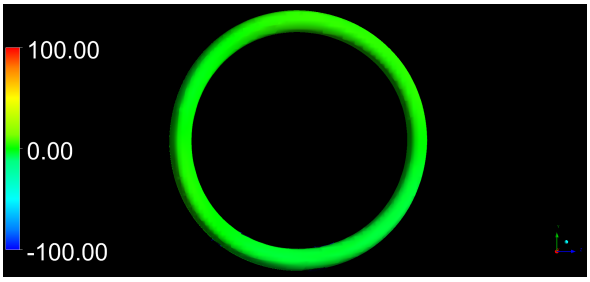

(a) Vortex ring at $\phi = 0.5$. At the time of formation, the vortex ring is perfectly circular.

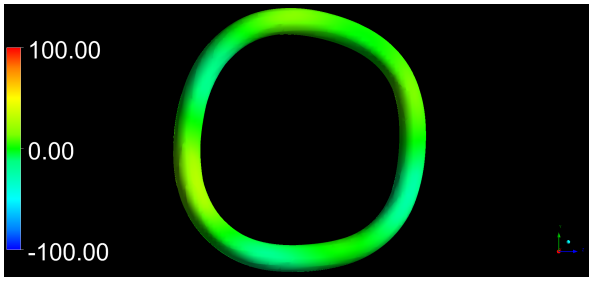

(b) Vortex ring at $\phi = 0.7$; the azimuthal instability has just set in.

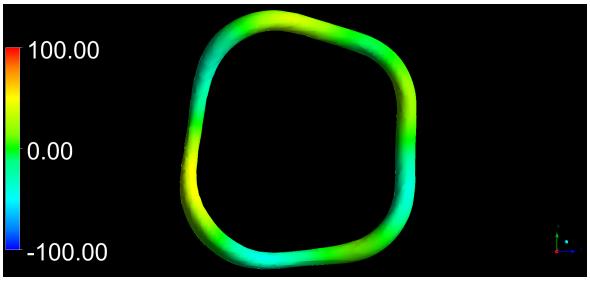

(c) Vortex ring at $\phi = 0.8$. The azimuthal instability has taken a well defined 4 wave shape.

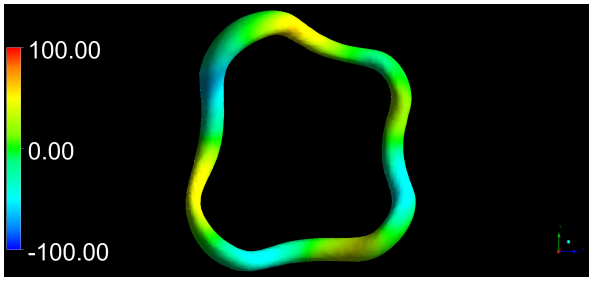

(d) Vortex ring at $\phi = 0.9$. The instability has completely developed before exiting the aneurysm.

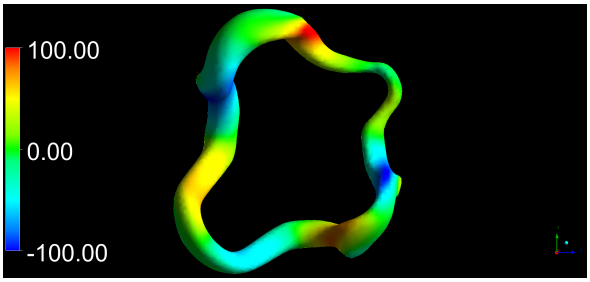

(e) Vortex ring at $\phi = 1$; just before breaking up into smaller vortices.

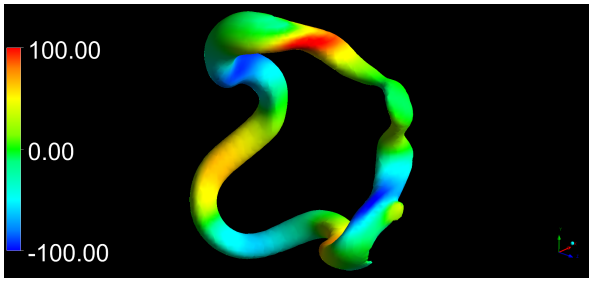

(f) A 3D view at $\phi = 1$ to illustrate the large amplitude of the instability.

Figure 5.3: Development of an azimuthal instability on the vortex ring. The ring is illustrated through an iso-surface obtained using the Q criteria [41] and is coloured in accordance with the contours of streamwise or X vorticity [s^{-1}]. It should be noted that for a clear visualisation of the ring, the images have been edited to filter out the background structures that have the same value of Q criteria as that of the ring. Initially, the vorticity has zero component along the streamwise direction but the azimuthal instability causes a rearrangement of vorticity thereby creating vorticity in the streamwise direction.

5.1.3. Turbulent Kinetic Energy (TKE) Contours

Figure 5.4 depicts the phase averaged turbulence intensity at various phases in the XY plane (Z = 0). The turbulence intensity is calculated by dividing the turbulent kinetic energy (TKE) by the square of the mean bulk flow velocity over the entire cycle i.e by u_{avg}^2. As evident from the figure, the intensity is concentrated at the exit region of the aneurysm. The vortex ring formation process and its initial advection is the same from cycle to cycle. Hence there are no inter cycle flow field differences at the same phase in the expansion region of the aneurysm and thus, no turbulent fluctuations are present. As the vortex ring travels further downstream, it breaks down into many smaller vortices which eventually pass out of the aneurysm and decay. This breakdown process and subsequent decay varies from cycle to cycle at every phase which leads to turbulence. The turbulent fluctuations die out well before the outlet of the flow domain indicating that the decay of smaller vortices is complete well before they can reach the outlet.

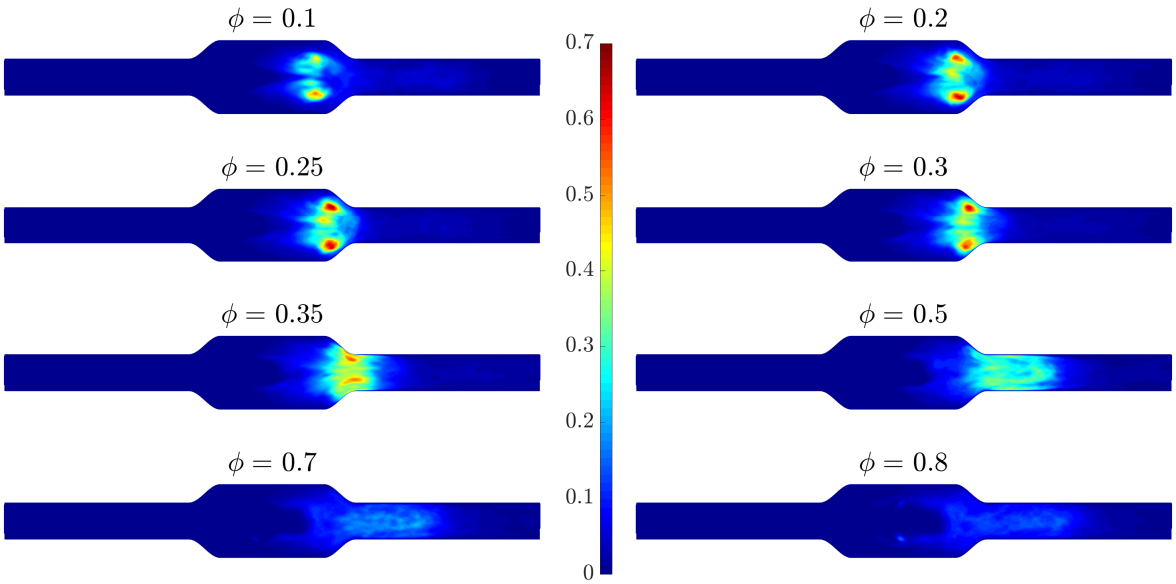

Figure 5.4: Phase averaged turbulence intensity contours at different phases in the XY plane (Z = 0) at selected phases. The turbulence intensity is maximum in the exit region of the aneurysm. Near the contraction, the vortex ring breaks down into smaller eddies that subsequently decay and this process does not happen in the same exact manner every cycle which leads to differences at the same phase within different cycles. This results in turbulent fluctuations around the exit region of the aneurysm.

5.1.4. Particle Residence Time

An intraluminal thrombus (ILT) is a commonly found feature in AAAs [42]. The term ILT refers to the formation of a blood clot in the aorta and in the context of AAAs, it can be attributed to the disruption of normal laminar blood flow. Several researchers have discussed the importance and the impact of an ILT in an AAA. In their article, Vorp et al [43] highlight that the presence of an ILT results in a decrease of the local wall strength. This is a consequence of the ILT acting as a local barrier against the oxygen

flux from the lumen to the inner layers of the aortic wall which leads to local hypoxic conditions and hence wall degeneration. From a fluid mechanics point of view, a spatial region in an AAA susceptible to the formation of an ILT can be identified by observing blood flow and marking areas of recirculation or 'dead flow' regions. A recirculating region will not be replenished with fresh blood every cycle and thus the arterial tissue adjacent to such a region will become hypoxic and ultimately degenerate. In this thesis, a particle residence time study is conducted and recirculating regions are identified with the help of tracer particles. The entire solution field is marked with tracers having the same physical properties as that of blood and then simulations are done for 20 cycles with continuous fresh blood injection at the inlet. Thus, the tracer particles can be thought of as old blood. A contour plot of the mass fraction of tracer particles illustrates the dead flow regions. Regions with high tracer mass fraction indicate that the blood at the start of 20 cycles has still not been flushed out of the aneurysm. The arterial tissue surrounding such a region will be depleted of oxygen and have lower wall strength. Figure 5.5 illustrates the mass fraction of tracer particles (old blood) after 5,10,15 and 20 cycles.

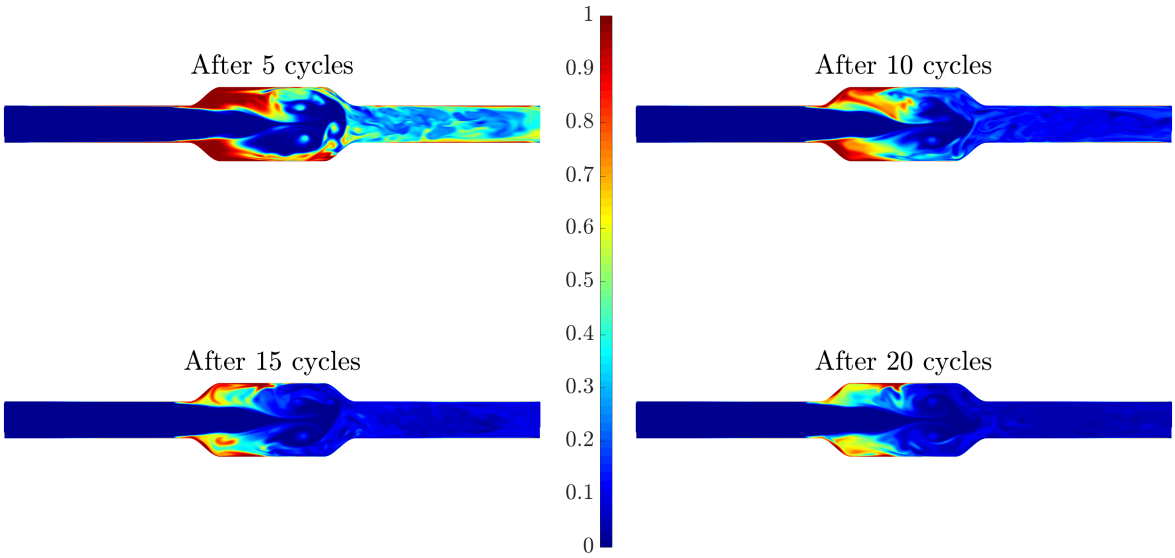

Figure 5.5: Tracer particle mass fraction contours after 5,10,15 and 20 cycles. The entire solution field is 'marked' with tracer particles having the physical properties of blood and then simulations are done for 20 cycles with continuous fresh blood injection at the inlet. The aim of doing so was to identify dead flow regions as the tracer particles (which can be thought of as old blood) will not wash out from such regions easily. Regions illustrated with dark blue depict fresh blood and regions illustrated with red depict the initially marked tracer particles (old blood).

Regions depicted with red indicate tracer particles and regions indicated with blue indicate fresh blood. Naturally, a higher concentration of blue indicates that the mass fraction of fresh blood in that region is higher and vice versa for red. Another way to study particle residence time is to monitor the mass fraction of tracer particles flushed out of the flow domain with an increasing number of cycles. Figure 5.6 depicts the area weighted cycle averaged mass fraction of the tracer particles at the outlet of the flow domain against the number of cycles simulated. It can be seen that even after 20 cycles, around

5% of the total mass fraction at the outlet is composed of tracers or old blood. This implies that there are still pockets of old blood present in the aneurysm. The overall trend can be approximated reasonably with an exponential curve.

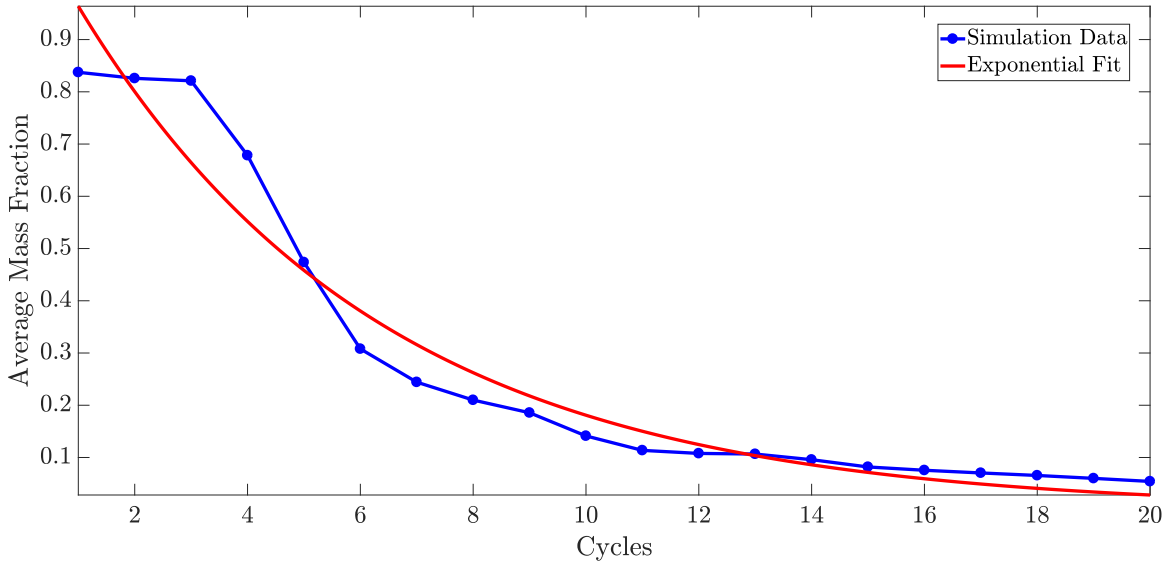

Figure 5.6: Trend of area weighted cycle averaged mass fraction of the tracer particles at the flow domain outlet with number of cycles simulated. Even after 20 cycles, all the tracer particles have not been washed out completely from the aneurysm. An exponential fit gives a reasonable approximation of the actual value trend against time.

The severity of the dead zones can be estimated from studying both, figure 5.5 and 5.6 together. From 5.6, it can be seen that after 20 cycles, the average mass fraction of the tracer particles/ old blood being flushed out is just around 5%. From figure 5.5 it can be seen that there is very little change in the mass fraction of the old blood near the expansion region after 15 and 20 cycles. Moreover, nearly 50% of the mass fraction in this region is still comprised of old blood but figure 5.6 doesn't reflect this. This suggests that the old blood present near the proximal neck is stuck in a strong recirculating region and will not flush out even after a longer period of time. This will lead to local hypoxic conditions and thus the arterial tissue will degenerate thereby reducing its mechanical strength.

5.1.5. Comparison between the XY and ZX Plane

As mentioned earlier in chapter 4, velocity and vorticity are exported in both the XY and ZX plane. The primary purpose of doing so was to be able to compare the flow field in both the planes and thus potentially identify any peculiar features in the flow field. Till now, all the contour plots shown have been plotted in the XY plane. To carry out a comparison of the flow field in both the planes, the mean of the phase averaged TKE within the aneurysm is plotted as a function of the phase within a cycle. This is done in both the XY plane and the ZX plane and then the variation of the mean phase averaged TKE is compared for both the planes. Figure 5.7 depicts such a comparison. First, the trend of the mean phase averaged TKE is plotted individually for both planes. As a reference, the inlet velocity waveform

is also shown so that the occurrence of peak turbulence or its decay can be related to the applied inlet velocity. Finally, the periodic kinetic energy (PKE) (energy that is contained in the structures which are produced every cycle in the exact same fashion) is plotted in both the XY as well as the ZX plane for easy comparison.

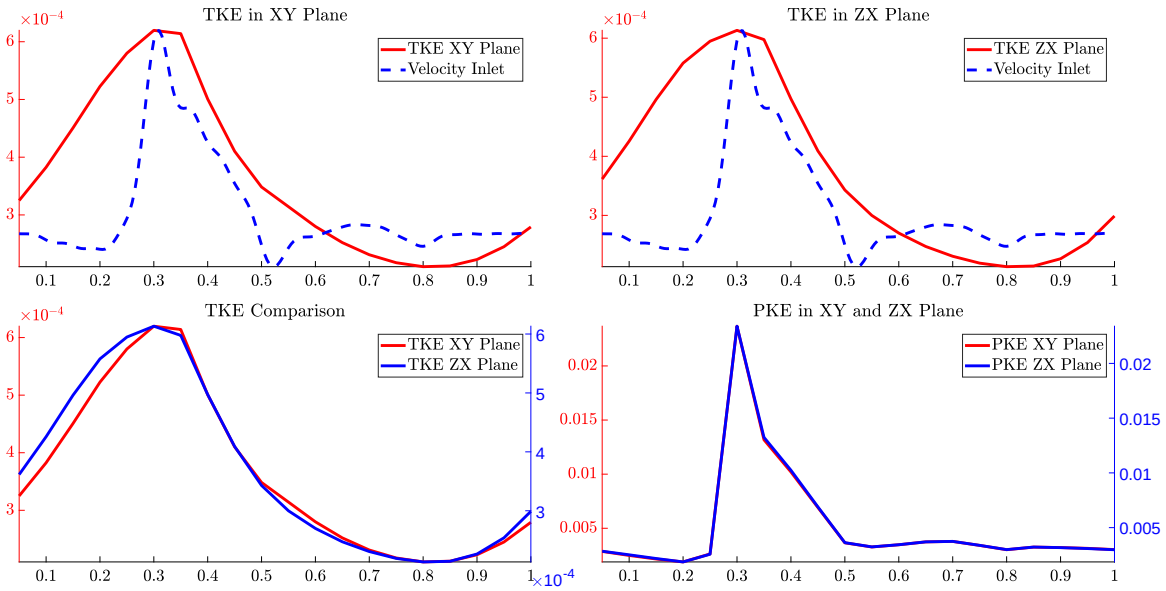

Figure 5.7: Mean phase averaged TKE $[m^2/s^2]$ and PKE $[m^2/s^2]$ comparison between XY and ZX plane in the aneurysm. The color of each line plot corresponds to the color of the y axis it is associated with. The X axis in all the figures represents the phase (t/T) in a cycle. In the top two figures, the inlet velocity waveform is shown just for reference. From the top two figures, it can be seen that the peak TKE occurs at peak systole in both the XY and the ZX plane. This implies that the vortex ring breaks down completely just around the peak systole and just before a new vortex ring is shed. In the bottom two figures, TKE and PKE for both the planes are plotted together for easy comparison. It can be seen that the trend in both planes is quite similar but not identical due to the absence of axisymmetry or the presence of turbulence. Hence, it is safe to conclude that contours in the ZX plane will be similar to those in the XY plane and are thus not shown for every variable in this thesis.

From the above figure, it can be seen that both the TKE and PKE follow a similar trend in both the planes. It is interesting to note that the peak TKE in the aneurysm occurs at peak systole or just before a new vortex ring is shed. This implies that the vortex ring breaks down just before the instant when a new vortex ring of the next cardiac cycle is shed. Since the plots are similar for both the planes, it is safe to conclude that contours in the ZX plane will be similar to those in the XY plane and are thus not shown for every variable in this thesis. The above shown plots are meant only for the purpose of inter-planar comparison and should not be used to draw any conclusion regarding the magnitude of turbulence present in the aneurysm since the plots are averaged over the entire planar surface and thus do not represent the local variation or extrema of TKE.

5.1.6. Pressure

Phase averaged static pressure along the centreline of the entire flow domain is plotted in figure 5.8. Since a zero outflow static gauge pressure boundary condition was prescribed at the outlet, all the lines converge to zero pressure at the outlet. The two dashed vertical lines indicate the streamwise extent of the aneurysm. From figure 5.8, it can be observed that at peak systole ($\phi = 0.3$), an overall large favourable pressure gradient exists in the entire flow domain. Within the aneurysm, the slope of this gradient decreases which is expected since the expansion in flow area leads to a decrease in the velocity. But during the deceleration phases that immediately follow peak systole ($\phi = 0.35 - 0.50$), an adverse pressure gradient can be seen in the aneurysm. It is this adverse pressure gradient that causes the shear layer to roll up, separate from the arterial wall and form a vortex ring, as illustrated earlier in figure 5.2.

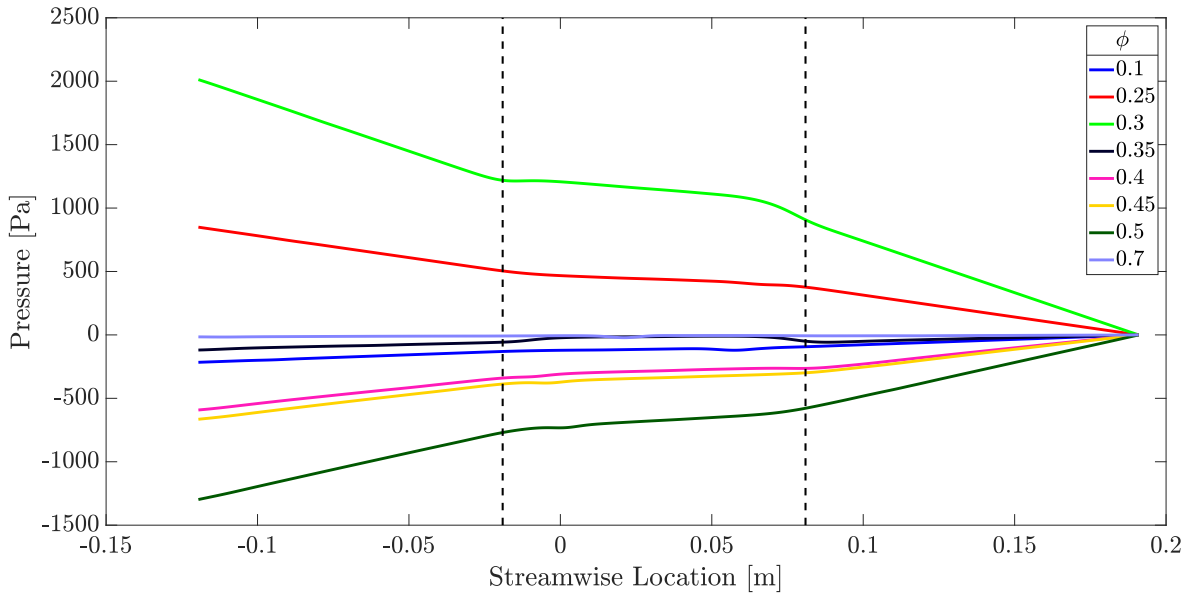

Figure 5.8: Phase averaged centreline pressure at selected phases. The two dashed vertical lines indicate the streamwise extent of the aneurysm. An adverse pressure gradient exists during the deceleration phases ($\phi = 0.35 - 0.50$) that follow peak systole. It is during these phases that the shear layer rolls up and separates from the arterial wall to form a vortex ring.

5.1.7. OSI and Wall Shear Stress (WSS)

Numerous researchers have investigated wall shear stress (WSS) in AAAs and tried to predict rupture sites on the basis of WSS; a good overview is given in the review article by Vorp [6]. The general conclusion that can be drawn from all the existing research is that the aneurysm surface usually displays lower mean WSS than the proximal and the distal neck. Figure 5.9 depicts the mean (over 60 cycles) WSS magnitude and OSI for case 5.

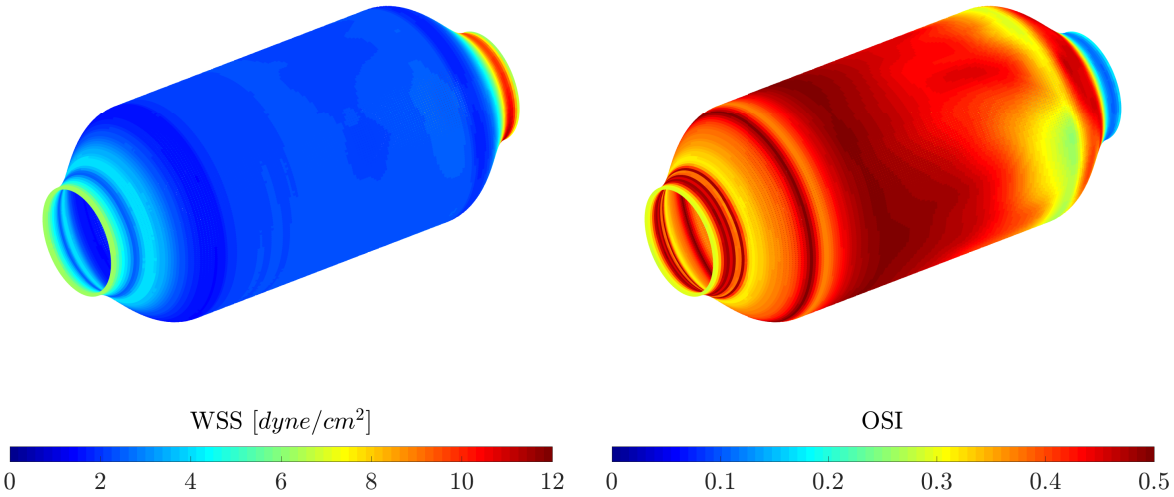

Figure 5.9: Mean (over 60 cycles) WSS magnitude and OSI for case 5.

From the figure, it can clearly be seen that the maximum mean WSS is present at the distal neck of the 4A geometry. Further, the aneurysm surface itself experiences significantly less WSS than the proximal or the distal neck. Both these observations were also reported in the study done by Le et al [44]. As for the mean OSI, the proximal neck displays a higher value than the distal neck. This too was observed in [44]. The OSI has a surprisingly low value at the distal neck which is perhaps due to the fact that at the exit of the 4A geometry, the contraction in the flow cross section forces blood to exit the aneurysm thereby ensuring that the WSS vector is more or less in the same direction every cycle. It is interesting to note that the maximum mean WSS is around 12 $dyne/cm^2$. This is approximately equal to the value that Giddens et al [11] mention as the upper limit for no further increment in the diameter of the abdominal aorta. For case 5, the highest value is at the distal neck and in order to reduce this value, the arterial wall will further inflate at that end thereby increasing the size of the aneurysm. This also suggests that once formed, a 4A geometry grows preferentially from the distal neck rather than the proximal neck. Further, Vorp's [6] observation that WSS is orders of magnitude lower than wall normal static pressure is verified and presented in appendix A.5.

5.2. Comparison between Various Cases

Now that the general flow field has been discussed, it is a good idea to highlight and discuss the differences present in the flow field of the various cases. All the geometries are referred to as indexed cases in this section and the reader is referred to table 5.1 for a quick overview of the geometrical features of every case.

5.2.1. Turbulence

As explained in section 5.1.3, breakdown of the vortex ring causes turbulent fluctuations in the flow field. This holds for all the cases except in cases 1 and 4 where no turbulence is observed at any phase of the cycle throughout the flow domain. This suggests that the vortex ring in these geometric configurations does not break down and simply passes through the aneurysm. To confirm this, contours of vorticity are plotted. Figure 5.10 illustrates the phase averaged vorticity contours for case 1.

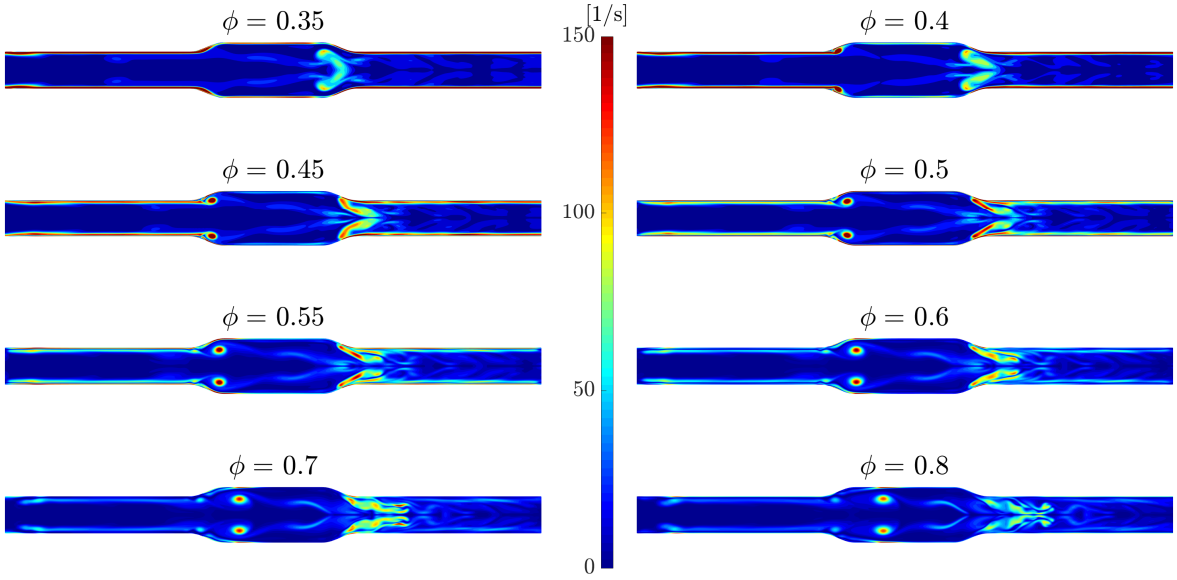

Figure 5.10: Phase averaged vorticity contours for Case 1 at selected phases. It can be seen that the vortex ring does not break down into smaller vortices but is rather differentially tilted when it approaches the exit region of the aneurysm. The ring is forced to rearrange itself as free shear layers on exiting the aneurysm.

From the figure, it can clearly be see that the vortex ring does not breakdown into smaller vortices within the aneurysm. As the vortex ring approaches the exit ($\phi = 0.20$), an azimuthal instability develops that grows as the vortex ring advects downstream. This instability causes the mid section of the ring to tilt in the streamwise direction which can be observed from figure 5.10. It is better illustrated in figure 5.11 that depicts the tilting through the iso surface of Q criteria [41], which is used in all the figures henceforth to illustrate the vortex ring. By the time the vortex ring reaches the exit of the aneurysm, systolic acceleration of the next cycle ($\phi = 0.3$) has already begun. Systolic acceleration coupled with the spatial acceleration due to the contraction in the flow cross section stabilizes the flow field. This ensures that instead of breaking down, the tilted vortex ring is forced to exit. The contraction of the flow cross section forces the mid region of the ring to exit first (which results in further tilting) followed by the outer regions of the ring. Hence, by the time the entire ring flows out of the aneurysm and enters the healthy aorta, all the vorticity is rearranged in space to now lie concentrated in free shear layers instead of a well defined circular ring. This can clearly be seen in the phase $\phi = 0.6$ in figure 5.10. This entire process repeats in the exact same fashion from cycle to cycle and thus the flow field is free of any turbulence.

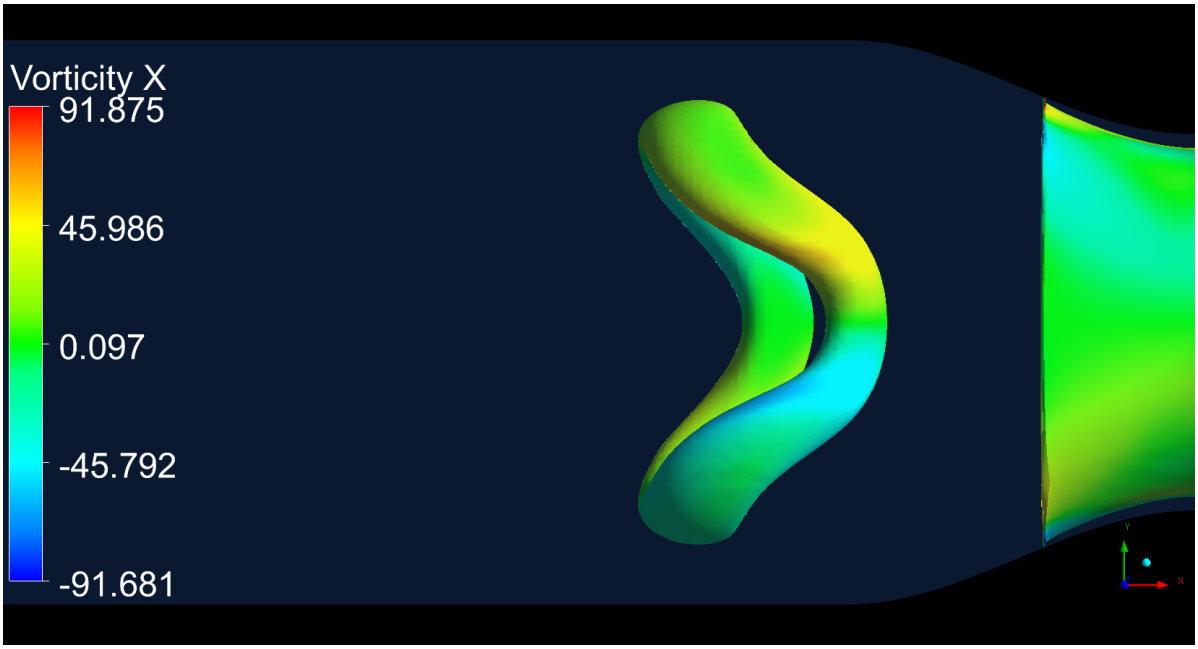

Figure 5.11: Q criteria iso surface of case 1 at $\phi = 0.3$. The tilting of the mid section of the ring can clearly be seen due to the development of the azimuthal instability. The iso surface is coloured by the streamwise vorticity to illustrate that the tilting process leads to creation of vorticity in the streamwise direction.

A similar process also occurs for case 4 and hence is not illustrated separately. It is interesting to note that for both case 1 and case 4, the EA equals $15°$ but the ER equals 1.5 and 2, respectively. This suggests that turbulence is a stronger function of EA than ER which is not completely surprising considering the fact that a smaller EA results in a gentler sloped adverse pressure gradient compared to higher EA pressure gradients. This leads to the consequence that a smaller disturbance destabilizes the flow for higher EA cases than for lower EA cases. It is also interesting to note that for both case 1 and 4, a similar azimuthal instability with only 2 waves develops. In all the other cases, the number of waves was at least 3. This suggests that a ring with a higher number of waves is more unstable as compared to a ring with lower number of waves. Further discussion on this matter is postponed until section 5.3.

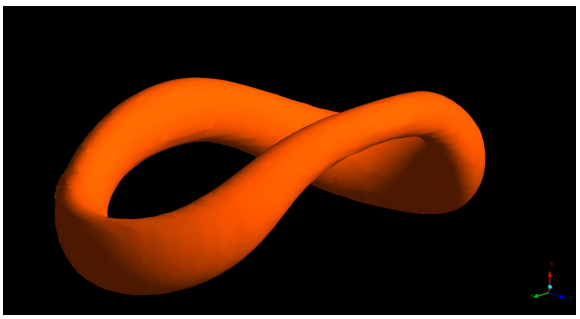

Figure 5.12: Azimuthal instability for case 1. 2 waves have developed on the ring.

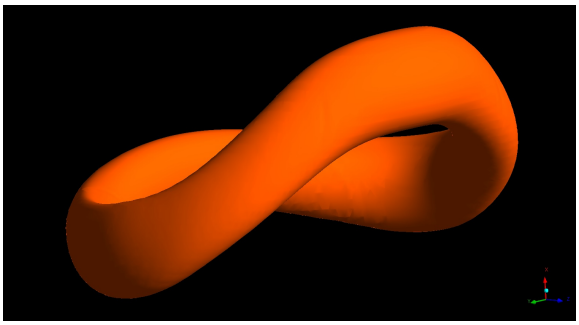

Figure 5.13: Azimuthal instability for case 4. Like case 1, 2 waves have developed on the ring.

5.2.2. OSI

To compare the OSI across all the cases, the surface average of the OSI distribution on the aneurysm surface is calculated for every case. Figure 5.14 illustrates the variation of the surface averaged OSI against expansion angle (EA) for various expansion ratios (ER). Although no clear trend for the averaged OSI can be observed from the plot, there are some interesting things that deserve attention. Across all the cases, the highest average OSI is for case 1 (ER of 1.5 and EA of 15°). This is totally unexpected as case 1 has the smallest ER and smallest EA across all the cases and thus, physically it represents an aneurysm that should be of least concern. Further, the average OSI of case 4 is less than the average OSI of a healthy aorta which suggests that the oscillatory nature of the wall shear stress vector is of greater concern in a healthy aorta than an intermediate stage 4A. Lastly, the average OSI for a 4A geometry with ER of 1.5 and EA of 45° is higher than the corresponding EA case with ER of 2.5. This suggests that if the severity of 4As was solely judged on the basis of OSI, then a smaller diameter aneurysm would appear to be more severe than a bigger diameter aneurysm.

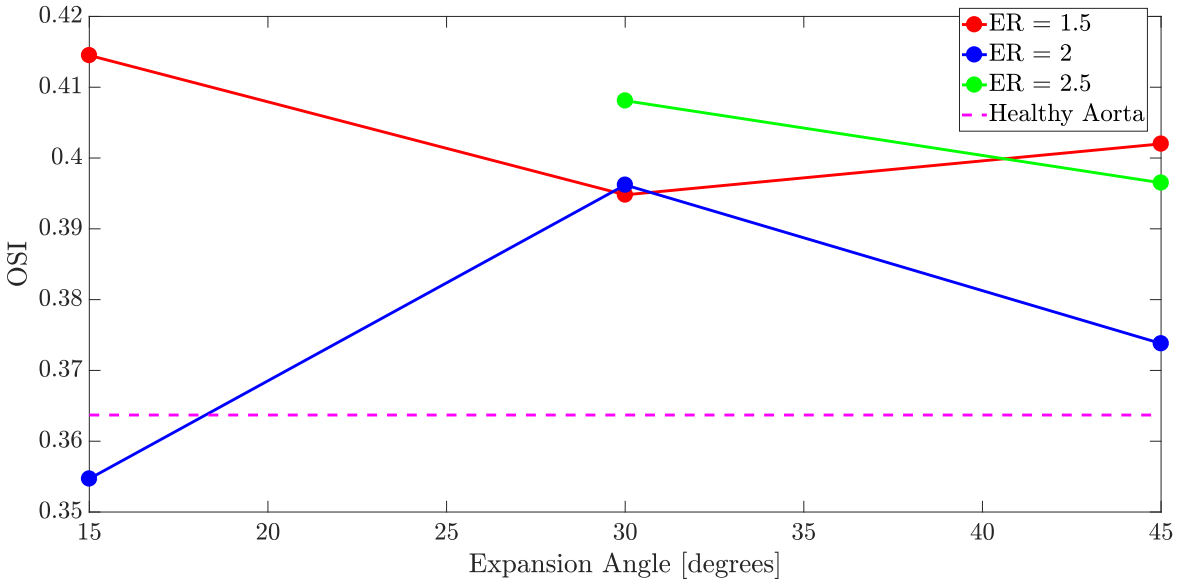

Figure 5.14: Surface averaged OSI as a function of expansion angle (EA) for different expansion ratios (ER). No clear trend in the values of the OSI can be observed. The average OSI for a healthy aorta is also shown for comparison purpose.

Thus, the above plot clearly highlights the shortcomings of a single hemodynamic parameter. Of course, it is possible that with some other configurations of the 4A geometry or some other values of Re/α, the OSI may present a clear trend but nothing can be said with absolute certainty. The above plot can also be interpreted in the sense that it is not always necessary for the biggest diameter aneurysm to pose the greatest threat; smaller diameter aneurysms can also rupture as pointed out earlier in section 1.2. Either way, the complexities involved in understanding aneurysms are clearly highlighted.

5.2.3. Particle Residence Time

As explained in section 5.1.4, ILTs tend to form in AAAs which cause the deterioration of the arterial wall and consequently a decrease in the wall strength. Thus, it is natural to conclude that an AAA with a larger ILT has a higher chance of rupture. From video clips, it was seen that in general, the inflection or the expansion and the contraction regions of a 4A geometry had the highest mass fraction of old blood after 20 cycles and thus posed the highest risk for an ILT formation. To carry out a quantitative comparison across all the cases, the area weighted average mass fraction of old blood is monitored in 4 high risk regions of every case, as illustrated in figure 5.15.

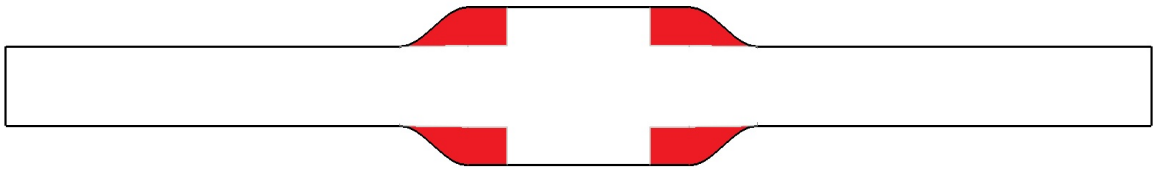

Figure 5.15: Regions monitored for 20 cycles in every case for the area weighted average of old blood mass fraction.

By the end of 20 cycles, the region that has the highest spatial average mass fraction of old blood in every case is compared against the highest spatial average region of all the other cases. Figure 5.16 illustrates such a comparison.

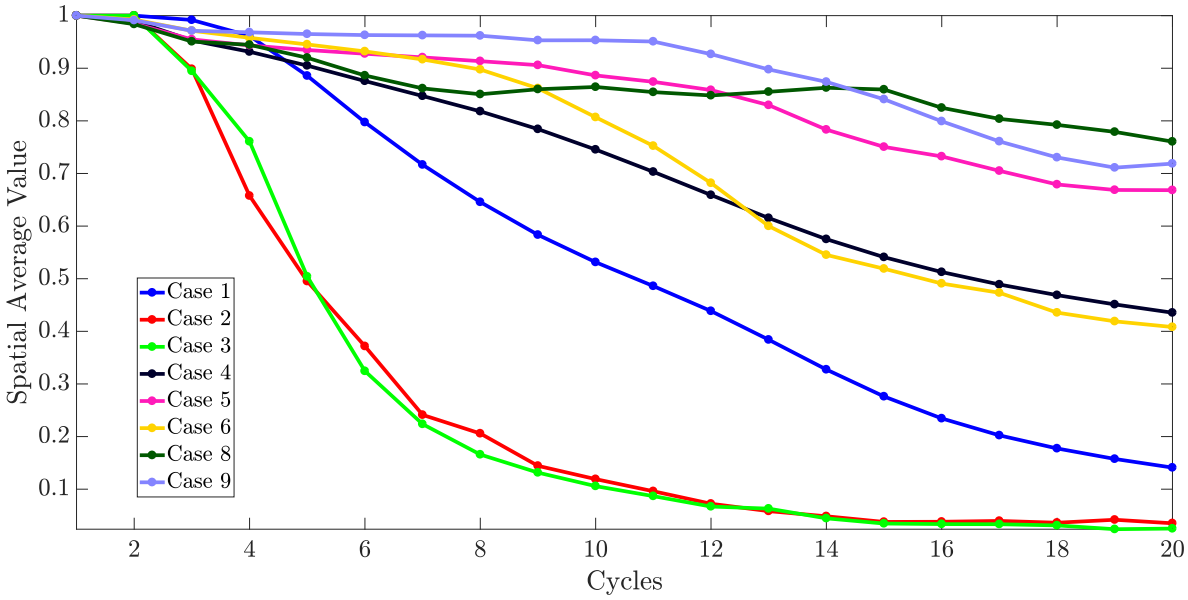

Figure 5.16: Spatial average of old blood for every case against number of cycles simulated. In general, cases with higher ER have a higher mass fraction of old blood present in the regions highlighted in figure 5.15.

It can be seen that by the end of 20 cycles, case 8 has the highest spatial average value of old blood in any one of the regions highlighted in figure 5.15. In general, as the ER of a 4A geometry increases,

the amount of old blood stuck in a recirculating region also increases. Further, there is a considerable difference in the time history of the spatial average value between case 1 and case 2/3. This is due to the absence of turbulence in case 1. Turbulence enhances the mixing of old and new blood and since case 2/3 have the least ER, turbulent fluctuations occupy the majority bulk of the flow domain. Hence, almost all the old blood is flushed out of the aneurysm for cases 2 and 3 but since case 1 is free of turbulence, old blood is flushed out much more slowly. A qualitative estimate of the extent of a potential ILT or a recirculation region can also be obtained from the mean (cycle averaged) velocity contours of the flow field. Figure 5.17 depicts such a plot for case 5.

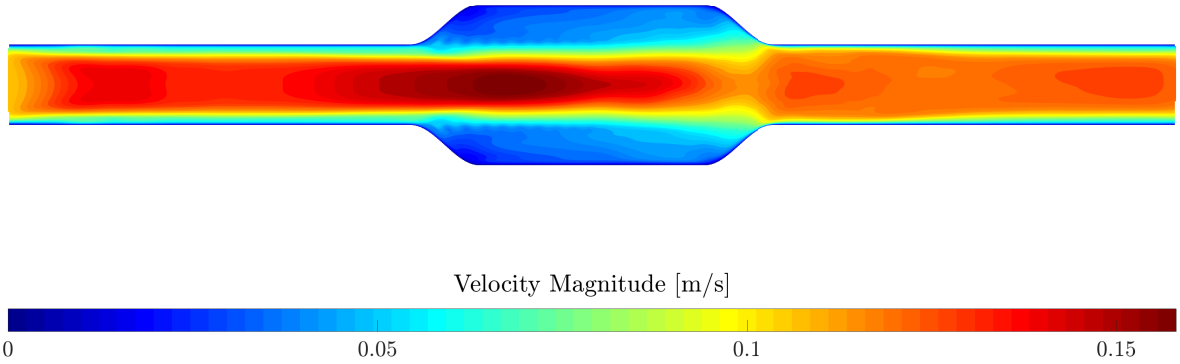

Figure 5.17: Mean (over 60 cycles) velocity magnitude contour plot for case 5. Extrmeley low velocity regions can be seen around the inflection regions of the 4A geometry. It can be seen that blood mostly passes through like a jet thus resulting in the creation of dead flow regions.

Doyle et al [45] carried out an experimental study in which they constructed silicone 4A geometries similar to the ones considered in this thesis and then inflated them with air until rupture. In almost all of the cases, the inflection region of the geometries ruptured and not the maximum diameter regions. Of course, since the experiment concerned only inflating the silicone models with air, the normal pressure within the geometry is responsible for causing rupture. Nonetheless, Vorp [6] stated in his review article that the normal pressure is many orders of magnitude higher than the flow induced WSS and thus is the deciding factor in causing rupture. Also, we now know that the inflection regions are highly susceptible to the formation of an ILT that weakens the vessel wall and the severity of an ILT increases with the ER of the 4A geometry. Combining all these observations we can conclude that as an aneurysm grows, the likeliness of it rupturing increases but not at the region of maximum diameter, as suggested by the current clinical practice, but rather at the regions of inflection. Nonetheless, the need to operate on a large diameter aneurysm is justified.

5.2.4. TKE and OSI Relation

One of the objectives framed for this thesis in section 1.5 was to correlate the effect of change in turbulence to a hemodynamic parameter such as the OSI. Figure 5.18 illustrates the average OSI and the average turbulence intensity trend as a function of ER for different EA. It should be noted that values for EA = 15° have been skipped since both the cases for such an EA show no turbulence.

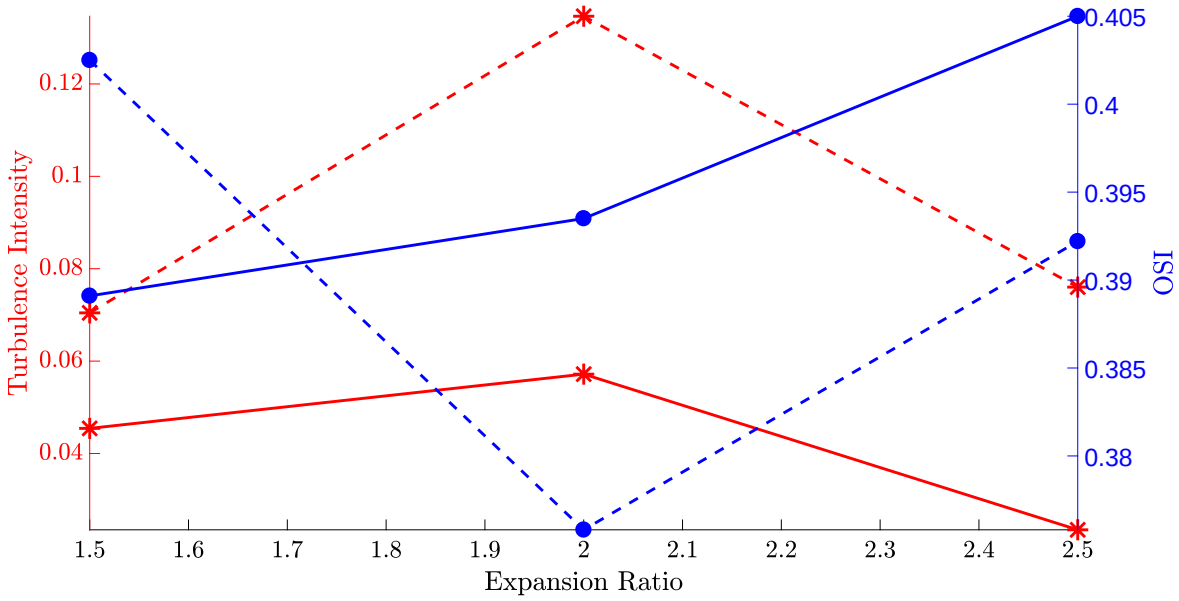

Figure 5.18: Average OSI and average turbulence intensity variation as a function of ER for two EAs. Note that values for the two cases with an EA of 15° have been skipped since there is no turbulence present in them. The color of any line plot corresponds to the color of the y axis it is associated with. Solid lines represent the cases with EA = 30° and dashed lines represent the cases with EA = 45°. No clear co-relation between turbulence and OSI can be seen.

From the figure, no clear correlation can be drawn between turbulence intensity and the OSI. For the case of EA = 30°, the average OSI increases on increasing the ER but the turbulence intensity increases first and then decreases. For the case of EA = 45°, the OSI decreases and then increases with an increase in ER whereas it is exactly the opposite for turbulence intensity. A possible reason for the apparent independence of OSI and turbulence intensity is that since turbulence in all the cases is in the bulk of the fluid, the velocity vectors near the wall are relatively unaffected by it. This is further supported by the fact that the highest OSI across all the cases is observed for case 1 (not plotted in figure 5.18) that is completely free of turbulence.

5.3. Discussion

It is now clear that turbulence in 4A geometries is due to the breakdown of a vortex ring that is shed just after the peak systole every cardiac cycle. In instances wherein the flow field remained free of turbulence such as in case 1 and case 4, the vortex ring did not break down. It is then only natural to question the stability of such vortex rings and the underlying mechanism of the formation and growth of

the azimuthal instability that destabilizes the vortex ring. Discussion regarding various aspects of the vortex ring is presented in section 5.5. For now, attention is turned towards the generation of turbulence in every case.

From video clips of instantaneous vorticity magnitude in the XY plane, it was realised that although the breakdown of the vortex ring is the cause of turbulent fluctuations, the manner in which the ring breaks down differs from case to case. In general, for cases with ER = 1.5 (except case 1), the ring completely broke down at approximately half the streamwise length (L_h) of the 4A geometry. For cases with ER = 2 (except case 4), the ring breaks down in the vicinity of the distal neck. For the cases with ER = 2.5, the ring does not break down until just after colliding with the distal neck. It is surprising to note that for cases with ER = 2.5, the distal neck causes the vortex ring to break whereas in section 5.2.1 it was seen that the ring did not break down in case 1 and case 4 partly due to the spatial acceleration the distal neck provides. To understand the cause of such differences, the flow field is investigated from a time scale perspective. 3 time scales can be defined for the general pulsatile blood flow through a 4A geometry.

- Vortex ring formation time scale (t_v) - This is the frequency of the formation of a vortex ring and thus scales with the frequency of the cardiac cycle. Since one ring is shed per cycle, this time scale is constant at 0.8s for all the cases considered in this thesis.
- Advective time scale (t_a) - This is the time it takes for a vortex ring to traverse the length of the 4A geometry assuming it does not break up by the time it reaches the distal end. Thus, t_v scales with the streamwise length (L_h) and the translational velocity U of the vortex ring.
- Stability time scale (t_s) - This is the time it takes for the ring to break up into smaller vortices from the instant of the onset of the azimuthal instability.

Depending on the value of t_a and t_s, the following scenarios are possible

- $t_s < t_a$ - In this case, the vortex ring will break down into smaller vortices before it is able to exit the aneurysm. All the cases except the ones with ER = 2.5 display such a relation between t_s and t_a.
- $t_s > t_a$ - In this case, the ring traverses the entire streamwise length of the aneurysm without breaking up and ends up colliding with the distal neck, as in the cases with ER = 2.5. It should be noted that such a relation between t_a and t_s should not be understood as the absence of an azimuthal instability but rather as the insufficient growth of the azimuthal instability leading to a delay in the break up of the ring.
- $t_s \approx t_a$ - In this case, the ring breaks just before colliding with the distal neck. Such a situation is not observed (within visual limits) amongst any of the cases considered in this thesis.

To get an idea as to how t_a varies from case to case, the streamwise length (L_h) of the aneurysm in each case is calculated. L_h of the aneurysm refers to the straight horizontal section of each 4A geometry

case between the expansion and contraction regions. Thus, L_h can be calculated by subtracting the length over which the aneurysm expands/ contracts from the total 4A length of 100 mm. The streamwise length, non dimensionalised by the inlet or healthy aorta diameter d_0, in every case is given in table 5.2.

Case	ER	EA	L_h/d_0
Case 1	1.5	15°	2.68
Case 2	1.5	30°	3.68
Case 3	1.5	45°	4.04
Case 4	2	15°	0.81
Case 5	2	30°	2.81
Case 6	2	45°	3.54
Case 8	2.5	30°	1.95
Case 9	2.5	45°	3.04

Table 5.2: Overview of all the L_h

It can clearly be observed from 5.2 that the L_h of a 4A geometry increases with increase in EA at the same ER. It should also be noted that L_h decreases as the ER increases at a constant EA. Both these trends are a result of the constant total aneurysm length criteria across all the cases. The difference between various cases with respect to the L_h is better understood through the visualisation of every 4A geometry in figures A.8 - A.10. To get an estimate of t_a, an estimate of the translational velocity U of the vortex ring is required. For the vortex rings generated in all the cases in this thesis, U is comprised of 2 components: self induced translational velocity and the bulk flow velocity. It is reasonable to assume that at the instant of ring formation, U will approximately be the same across all the cases. Since $t_a \sim L_h/U$, the advective time scale will be bigger for those cases with a higher value of L_h and smaller for cases with a lower value of L_h. As for the estimate of t_s, it can be assumed that it will be of the same order of magnitude across all the cases. Assumptions taken regarding t_a and t_s are further elaborated upon in section 5.5. Thus, from the L_h values presented in table 5.2, the tendency of the vortex ring to break down within the 4A geometry can be expected to be the highest for cases with a higher value of L_h. This is also observed in the simulations; breakdown of the vortex ring in cases 2 and 3 occurs approximately at half the length of L_h and for case 5 and 6 it occurs near the distal neck of the aneurysm. But for case 8 and 9, which but have the smallest values of L_h out of all the cases for their respective EA, the vortex ring does not break and instead collides with the distal neck of the 4A geometry. On approaching extremely close to the distal neck, which is nothing but an axisymmetric inclined wall, a shear layer structure (SLS) of the opposite sense of vorticity is ejected from the inclined wall. The interaction of this structure with the vortex core destabilizes the flow field and causes the ring to immediately break down. This kind of interaction of a vortex ring with an inclined wall is also reported by Lim [46] and Verzicco et al [47]. Figure 5.19 illustrates the ejection of the shear layer structure.

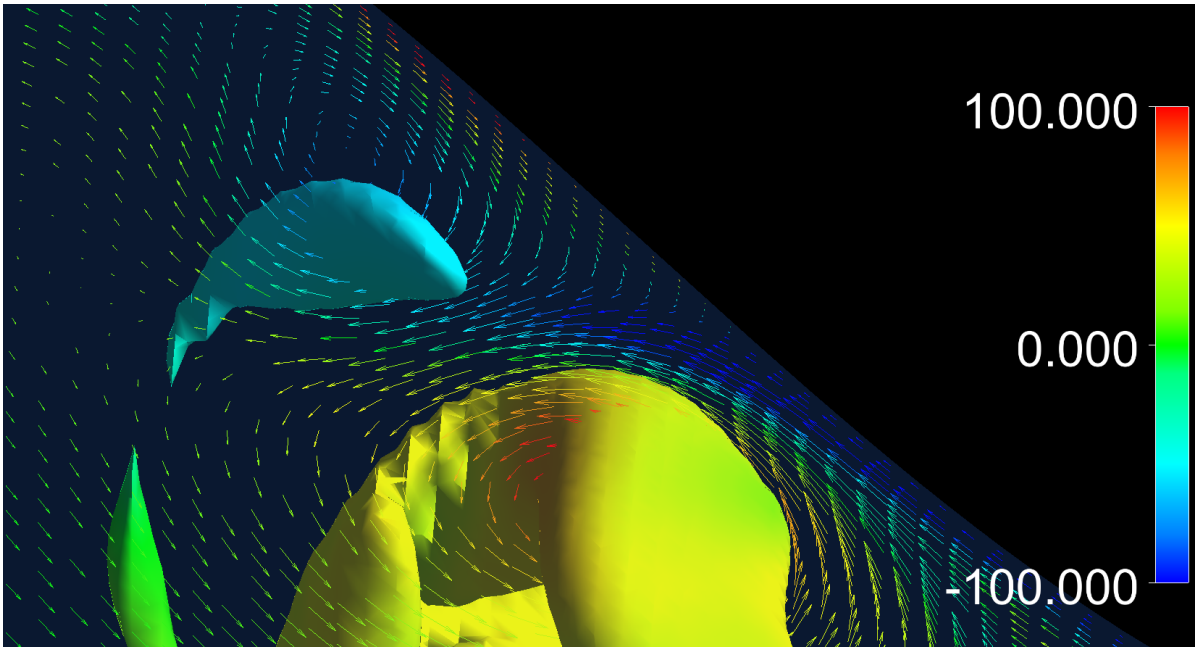

Figure 5.19: Ejection of a shear layer structure (SLS) from the distal neck. The iso surfaces are coloured by the Z vorticity [s^{-1}] vector (perpendicular to the plane of the paper). The velocity vector is also plotted in the XY plane (Z = 0) to further illustrate the sense of rotation of fluid particles. It can clearly be seen that the fluid particles in the SLS (blue color) have an opposite sense of rotation as compared to the particles in the vortex ring (green color). The interaction of these two opposite vortical structures causes a breakdown of the ring.

It is interesting to note that case 1 and 4, wherein the vortex ring did not break at all, do not display such an ejection of shear layer despite the collision of the vortex ring with the distal neck. A possible reason for this different behaviour from that of case 8 and 9 is that the vortex ring undergoes temporal acceleration (seen in video clips of instantaneous vorticity contours) in addition to the spatial acceleration at the distal neck for cases 1 and 4. This basically means that by the time the vortex ring comes in close approach to the distal neck in case 1 and 4, systolic acceleration of the next cycle begins which does not allow the ring to spend enough time in the vicinity of the inclined wall thereby not allowing it to induce a strong enough shear layer of opposite vorticity. Hence, there is no ejection of a shear layer structure and the ring does not break down but instead simply passes through the distal neck. But for case 8 and 9, the vortex ring comes in close vicinity of the distal neck during the diastole of the same cycle and is hence not temporally accelerated. It can be deduced that the difference in phase (systole/diastole) for case 1/4 and 8/9 at the time of collision with the distal neck is due to the difference in L_h. Thus, the importance of t_a can now be clearly understood.

5.4. Simulation of Semi Infinite Domain

Since the breakdown of the vortex ring in case 8 and 9 is induced by the ejection of a SLS from the distal neck, it is only natural to wonder about the vortex ring stability in the absence of the distal neck. Although it is known that a reduction in the flow cross section usually stabilizes the flow field, its effect

on complex structures such as a vortex ring is uncertain. Moreover, in cases 5 and 6, the ring breaks down in close vicinity of the distal neck suggesting that there is a possibility of the distal neck having a destabilising effect on the vortex ring. To investigate this, new geometries were created for all cases in which the converging section at the aneurysm end was removed and the dilated aorta was sufficiently extended in the axial direction to resemble a semi infinite domain. Cases with an ER of 1.5 and 2 are extended to $20d_0$ from the end of the expansion region and cases with an ER of 2.5 are extended to $15d_0$. Although such an extension does not depict possible physical conditions, it allows for the investigation of t_s without any influence of L_h. Figure 5.20 illustrates the extended flow domain for case 5.

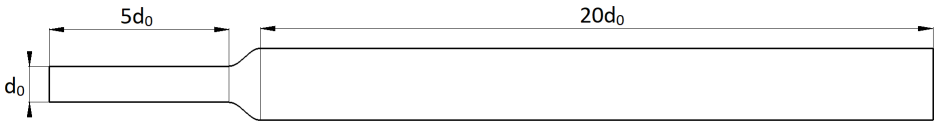

Figure 5.20: Flow domain extension for case 5 to $20d_0$.

Simulating 75 cycles as done for the aneurysmal cases is too computationally expensive and also excessive since the objective of the semi infinite domain simulations is to only study t_s. Thus, only 30 cycles are simulated in all the cases and the averaging procedure is done over the last 5 cycles. All the rest of the simulation aspects for the extended cases are the same as those for the aneurysmal cases. To investigate t_s, the mean (over 5 cycles) turbulence intensity along the centreline of the entire flow domain is plotted and shown in figure 5.21.

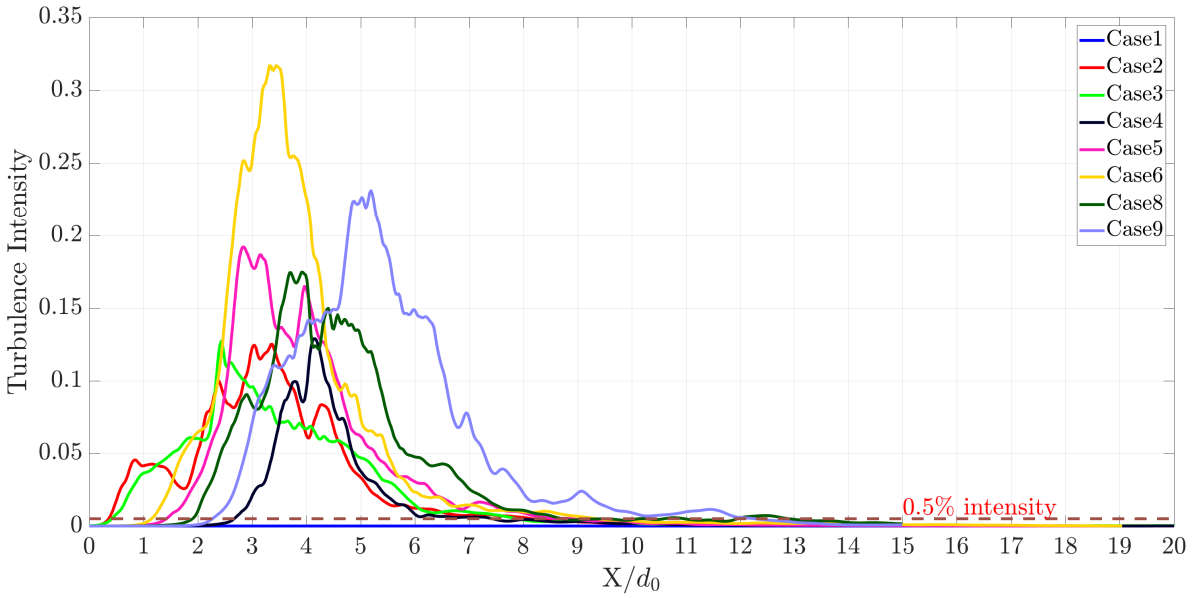

Figure 5.21: Mean centreline turbulence intensity for all the extended domain cases. Peak intensity corresponds to the axial location of the ring breakdown. Across all the cases, breakdown occurs between $2d_0$ and $5d_0$. The flow relaminarizes by axial distance $10d_0$ for all the cases.

In the figure, a similar general trend can be seen amongst all the cases: turbulence intensity, along the centreline of the dilated aorta, first rises till a maximum and then decreases. The peak of the turbulence intensity curve can be approximately assumed as the axial location at which the vortex ring breaks down [35]. Like the corresponding aneurysmal geometry, case 1 did not show any turbulent fluctuations. It was observed that the vortex ring gradually decayed along the streamwise length. Surprisingly, unlike its aneurysmal counterpart, case 4 displays turbulent fluctuations. The vortex ring breaks into smaller vortices at a distance just higher than $4d_0$ along the centreline. Since $L_h < 4d_0$ in case 4 (table 5.2), it can now be deduced that $t_a < t_s$ and hence the vortex ring simply passes through the aneurysm. In general, all the cases show peak turbulence between $3d_0$ and $5d_0$. Again referring to table 5.2, it is now fairly straightforward to realize that the vortex ring in cases 8 and 9 too did not break within the aneurysm due to the insufficient length of L_h. For all the other cases, breakdown of the ring occurred more or less at the same axial location as in the corresponding aneurysmal geometries which suggests that the flow field in both the scenarios is similar. Thus, the presence of converging walls has an effect on the stability of the vortex ring only in cases 4,8 and 9; for all the other cases breakdown of the ring occurs as it would have in the corresponding 4A cases.

As explained earlier, the breakdown process of the vortex ring is brought about by the onset of an azimuthal instability on the vortex ring. As the final aspect of the flow field in semi infinite domains, the number of waves developed on the ring is compared against the number of waves developed in the corresponding aneurysmal cases. Across all the cases, it was found that the number of waves developed is the same for both, the semi infinite domain and the corresponding aneurysmal case, with the only difference being the orientation of the waves. This strongly suggests that the onset of the instability and its subsequent growth is heavily influenced by the geometric parameters of the 4A geometry and the interaction of the vortex ring with the remnants of the flow field of the previous cycle rather than the presence of a convergent section at the distal end of the 4A geometry.

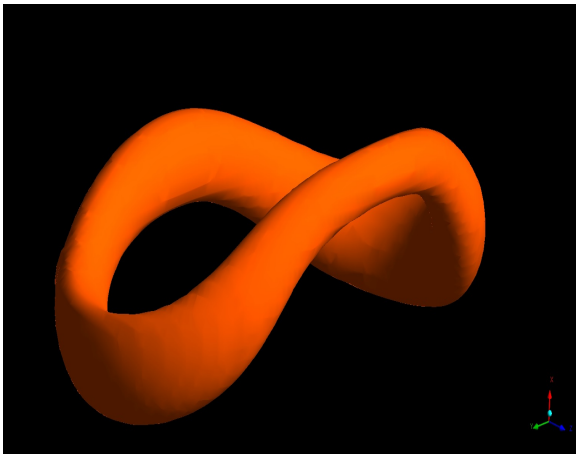

Figure 5.22: Isometric view (Axial direction up) of the azimuthal instability for case 1. 2 waves have developed on the ring. The color chosen is just for an illustration purpose.

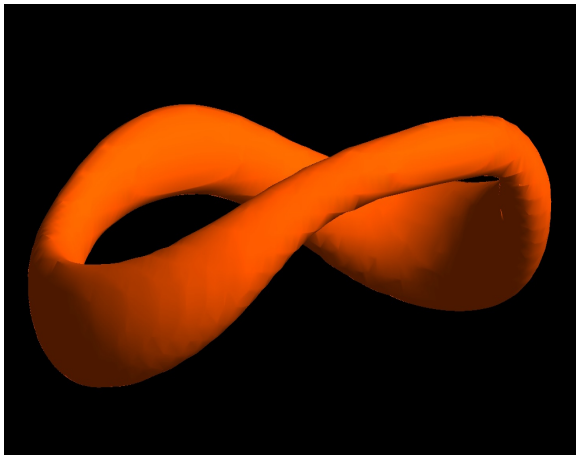

Figure 5.23: Azimuthal instability for extended domain case 1 (case 1L). Like its aneurysmal counterpart, 2 waves have developed on the ring. The color chosen is just for an illustration purpose.

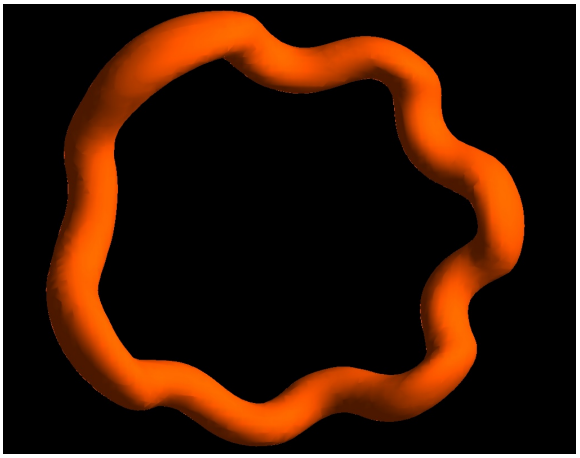

(a) Fully developed azimuthal instability for case 3.

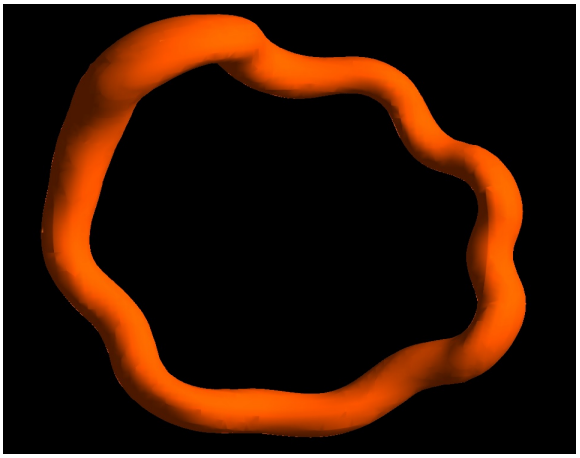

(b) Fully developed azimuthal instability for case 3L.

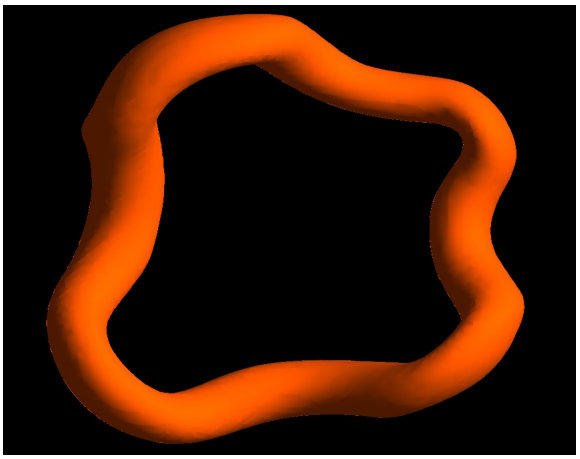

(c) Fully developed azimuthal instability for case 5.

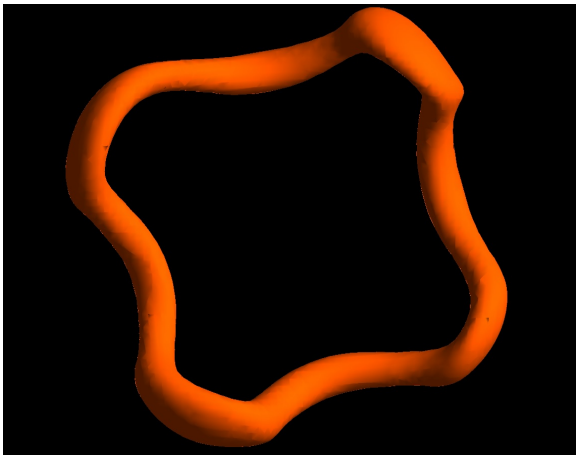

(d) Fully developed azimuthal instability for case 5L.

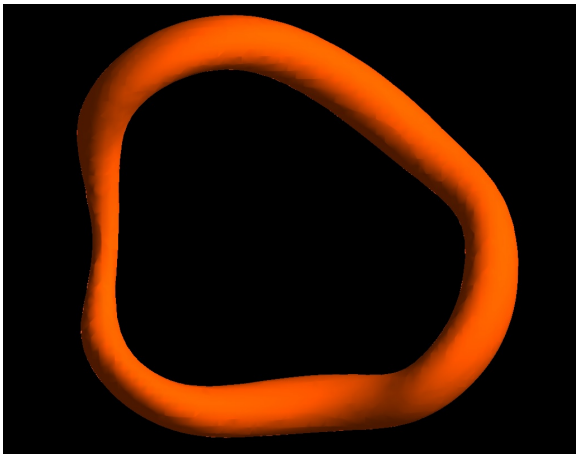

(e) Fully developed azimuthal instability for case 8.

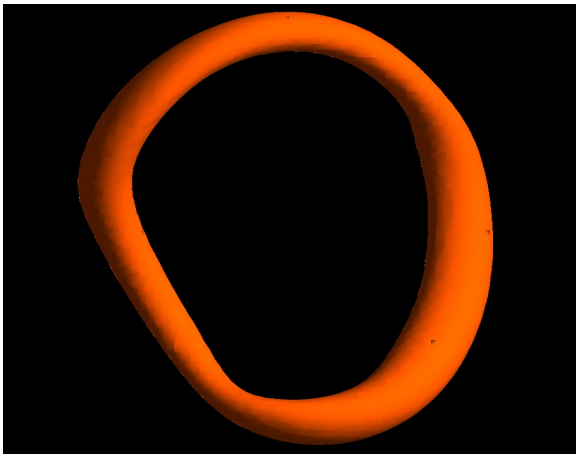

(f) Fully developed azimuthal instability for case 8L.

Figure 5.24: Comparison of the fully developed azimuthal instability on the vortex ring for selected aneurysmal cases and the corresponding semi infinite domains. The semi infinite domain cases are suffixed with the letter 'L'. As evident, the number of waves developed in both, aneurysmal case and extended domain case, is the same; only the orientation of the waves is different. All the views are in the YZ plane and the color used is just for an illustration purpose.

5.5. Characteristics of the Vortex Ring

Over the better part of the past century, numerous researchers have investigated vortex rings. A detailed overview of the research done so far is beyond the scope of this text but the interested reader can refer to the review by Shariff and Leonard [48]. The majority of the research done so far was concerned with the formation and propagation of laminar vortex rings in an unbounded domain. The vortex ring formed in a 4A geometry is an example of a ring formed in a radially confined domain and as such is fundamentally different from a ring formed in an unbounded domain. Investigation of such vortex rings has unfortunately not received attention despite their natural occurrence in various situations. Thus it is not surprising to know that the evolution of a vortex ring in a specific domain such as a 4A geometry has not been investigated yet. Various aspects in this scenario are different from the traditionally investigated vortex rings such as the radial confinement of the flow domain, pulsatile flow field and interaction of the vortex ring with the arterial walls. At the same time, some aspects are common with the vortex ring research done so far; the systolic acceleration is similar to the impulse provided by a piston in laboratory generated rings and the healthy aorta is equivalent to the nozzle that contains the fluid slug which would eventually form the vortex ring. Each of these aspects is individually treated in the following subsections with the help of previous research and a qualitative attempt is made to realize the combined effect of all these aspects on the vortex ring. It should be noted that the figures plotted in the following subsections are in the XY plane and illustrate selected cases only as all the cases display a similar trend and thus plotting for all the cases is not necessary. Further, in situations where the EA is expected to create a difference, all three EA for ER of 2 are illustrated i.e case 4,5 and 6. In situations where the ER is expected to play a role, all three cases with EA of $30°$ are plotted i.e case 2,5 and 8. For situations in which a global trend is expected, all the aforementioned 5 cases are plotted.

5.5.1. Structure of the Vortex Ring

As shown in figure 5.3 (at $\phi = 0.5$), a perfectly circular ring is formed at the time of formation. It should be kept in mind that a reasonably large volume of fluid, referred to as a 'bubble', is transported with the ring. Maxworthy's article [49] is taken as a reference to compare the geometrical aspects of the vortex ring formed in a 4A geometry to the aspects of a ring formed in an unbounded domain. As done in [49], plots of Z vorticity (ω_z) and Y velocity (v) at $\phi = 0.5$ are made to get an idea about geometric parameters such as the ring diameter (d) and the core diameter (a), respectively. $\phi = 0.5$ is particularly chosen throughout this subsection as the ring is perfectly circular then and thus can be expected to be structurally similar to a circular laminar ring. Of course, small differences will still be present due to the confined domain. Further downstream (and thus at a later phase), an azimuthal instability sets in which distorts the ring. Hence, it cannot be then analysed in a similar way as unconfined rings. The v velocity plot is made against normalized distance measured from the core center in the axial (X) direction. The distance between the maximum and minimum of v represents the core diameter a. The ω_z plot is made against normalized distance measured from the core centre along the Y axis till the ring center. The

location of the peak of ω_z is the core centre and thus, the vortex ring diameter d can be calculated. The vorticity and velocity distribution of a Lamb Oseen vortex are also plotted to illustrate the structural similarity between the two. To avoid unnecessary confusion, the plots made here are for case 5 only; similar procedure can be followed for other cases to obtain an estimate of a and d.

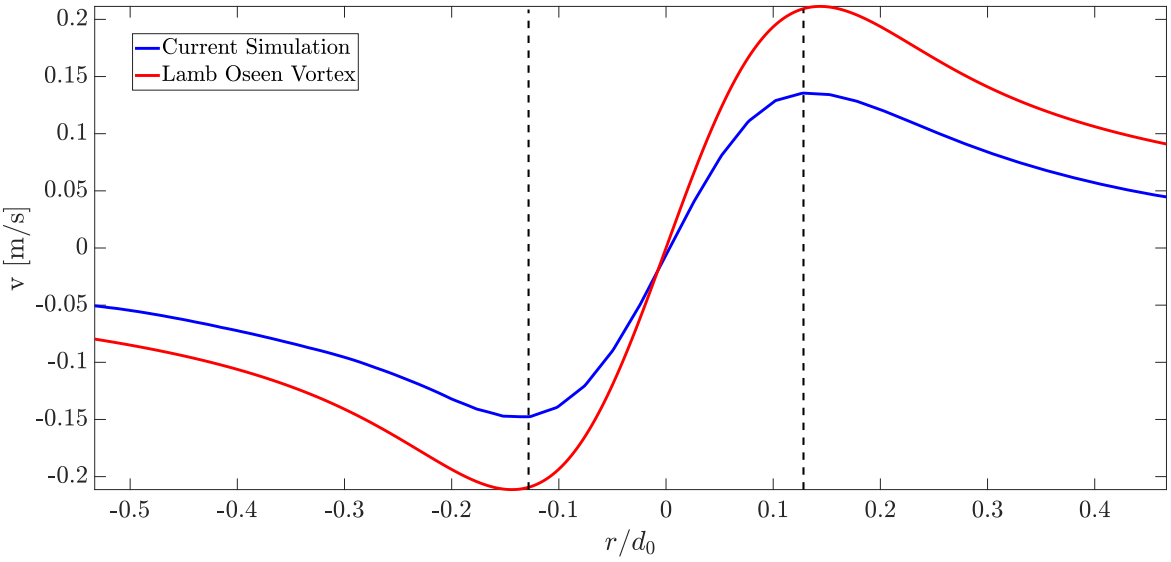

Figure 5.25: Measurement of v along axial distance at the vortex centre for case 5 at $\phi = 0.5$. The distance between the two extrema, highlighted by the two dashed black lines, is an indication of the vortex core diameter (a). The axial distance, from the center of the core ($r = 0$), is normalised with the healthy aorta diameter. From the figure, $a \approx 0.26 d_0$. The velocity variation is similar to that of a Lamb Oseen vortex of the same core diameter.

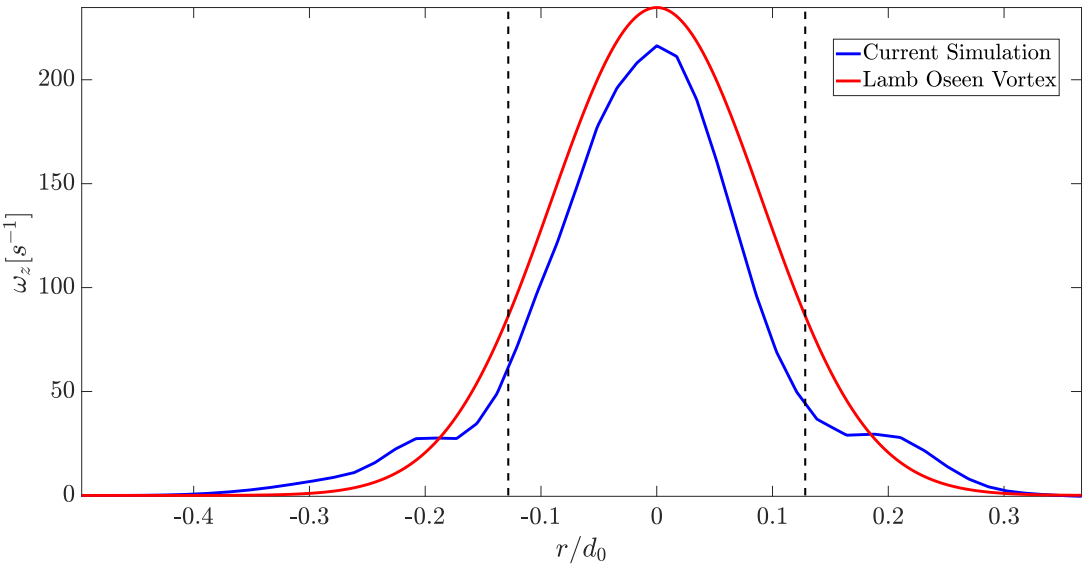

Figure 5.26: Z vorticity (ω_z) distribution along the normalised distance from the center of the ring along the Y axis for case 5 at $\phi = 0.5$. The vorticity peak corresponds to the core centre. The dashed black lines indicate the core diameter as obtained from figure 5.25. From the figure, ring radius $r \approx 0.497 d_0$ which leads to a ring diameter $d \approx 0.993 d_0$. The vorticity distribution is similar to that of a Lamb Orseen vortex.

From the above figures, the core diameter (a) is $0.26d_0$ and the ring diameter (d) is $\approx 0.993d_0$ for case 5 at $\phi = 0.5$. Maxworthy also reported that only about 50% of the total circulation resides in the core of the ring; the rest of the circulation is distributed throughout the ring bubble. This is verified for different cases in figure 5.27.

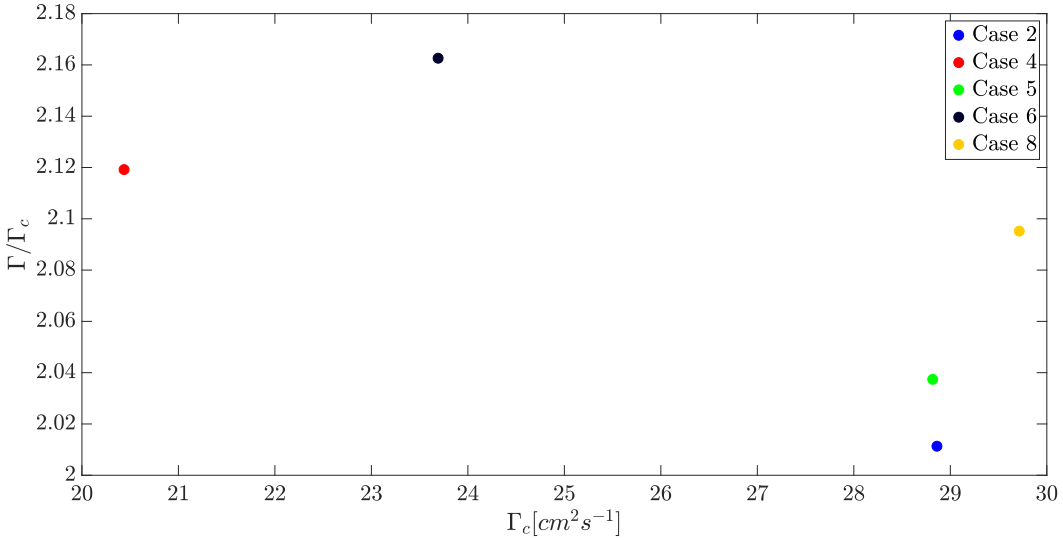

Figure 5.27: Ratio of total circulation Γ to core circulation Γ_c at $\phi = 0.5$. It can be seen that Γ is approximately twice of Γ_c. Γ_c is plotted on the X axis to give an idea of the absolute values.

Another interesting aspect to compute is the ratio of the ring diameter (d) and the healthy aorta diameter (d_0). Maxworthy observed that this ratio depends very weakly on the Re of the ring but more on the length of the ejected fluid slug. A more relevant finding to the vortex rings considered in this thesis is that he observed $d > d_0$ in all his cases. Figure 5.28 depicts this ratio for various cases.

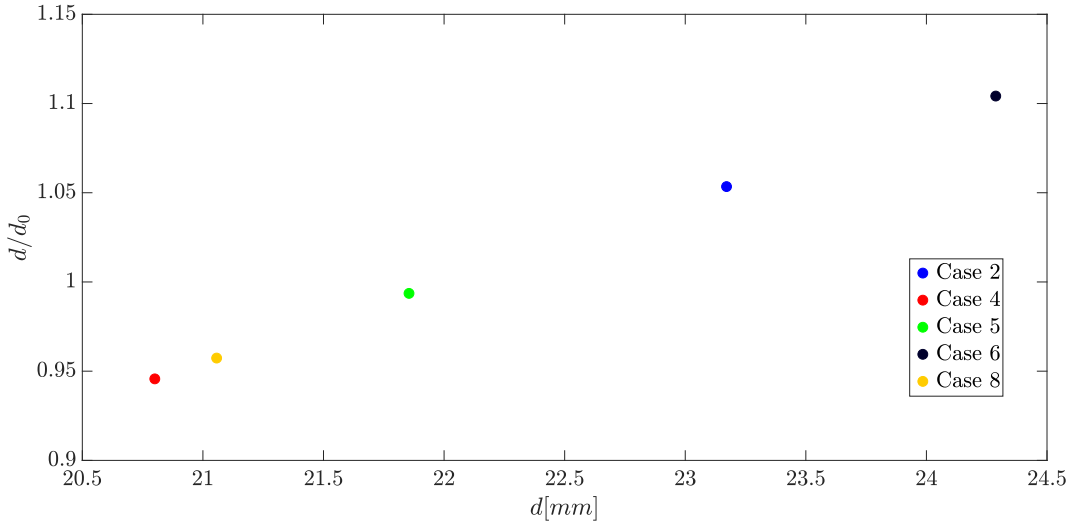

Figure 5.28: Ratio d/d_0 as a function of d for various cases at $\phi = 0.5$. d/d_0 is not greater than 1 for all the cases which is in contrast with Maxworthy's observation.

From the figure, it can be seen that Maxworthy's observation does not really hold for the rings generated across all the cases. A possible reason for this is that due to the confined domain, vorticity of opposite sense is induced on the nearby wall [50] which exerts a force on the near wall vortex core thus reducing the diameter of the vortex ring. A final interesting aspect to visualise is the trajectory of the vortex core centre in the XY plane. Maxworthy observed that initially the distance between the vortex cores increased upto a certain limit and then decreased to finally maintain a constant value. A detailed analysis of this behaviour can be found in Didden's article [51]. As for the cause of such a trend, Didden [51] points to the influence of the nozzle wall in his experiments stating that after a certain distance from the nozzle, the wall influence becomes negligible thereby allowing the vortex ring to have a constant diameter. Such an influence is not directly present in a confined domain such as a 4A geometry but a similar mechanism exists due to the axisymmetric walls. From video clips of vorticity contours, it was noticed that the vortex cores formed in various cases, specially at lower EA, do resemble the trend observed by Maxworthy and Didden. Figure 5.29 displays the vortex core centre trajectory for 3 cases having the same ER of 2 but different EA.

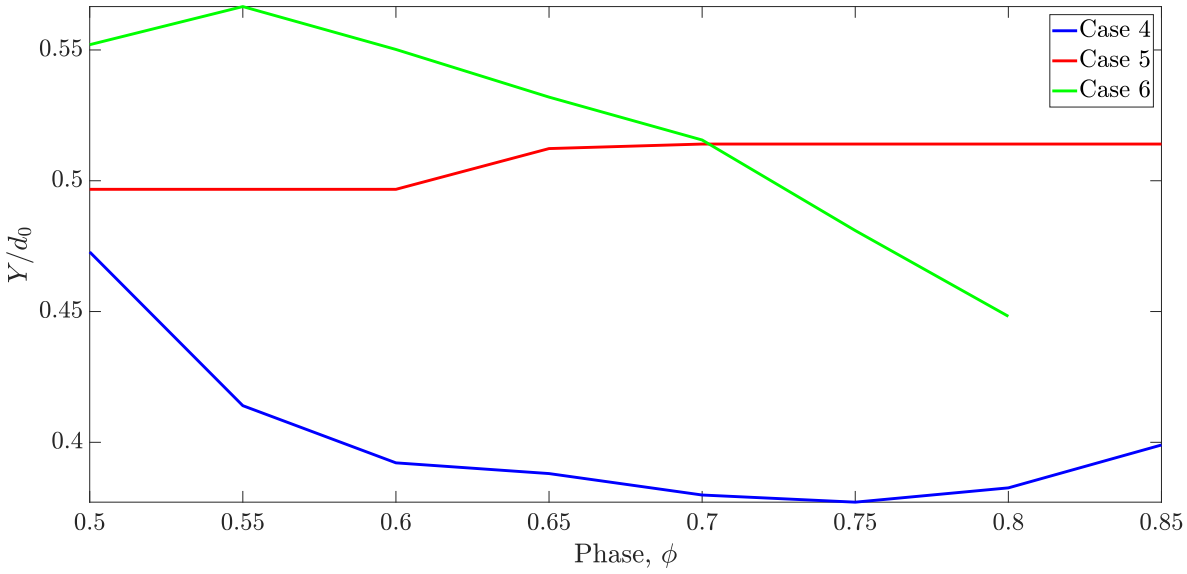

Figure 5.29: The trajectory of the vortex core in the XY plane with phase progression. Three cases of the same ER but varying EA are depicted as cases with different EA are expected to clearly exhibit a dynamic trajectory. Trajectory only till $\phi = 0.85$ is plotted since after this the ring breaks up. For case 6, the vortex ring breaks earlier at $\phi = 0.8$.

It can be seen that the change in the vortex centre trajectory is maximum for an EA of $15°$ and minimum for an EA of $30°$. A possible explanation for this is that at a lower EA, a gentler sloped adverse pressure gradient exists than at a higher EA which allows the shear layer to travel along the arterial wall for a slightly longer distance before it eventually separates and rolls up into a vortex. This delayed separation at a lower EA is illustrated in figure 5.30. Also, Stewart et al [50] mention in their article that due to the radial confinement, surface vorticity is induced on the confined wall having opposite sign of the near wall vortex core. This opposite sign vorticity is also induced in the 4A cases as shown in figure 5.31.

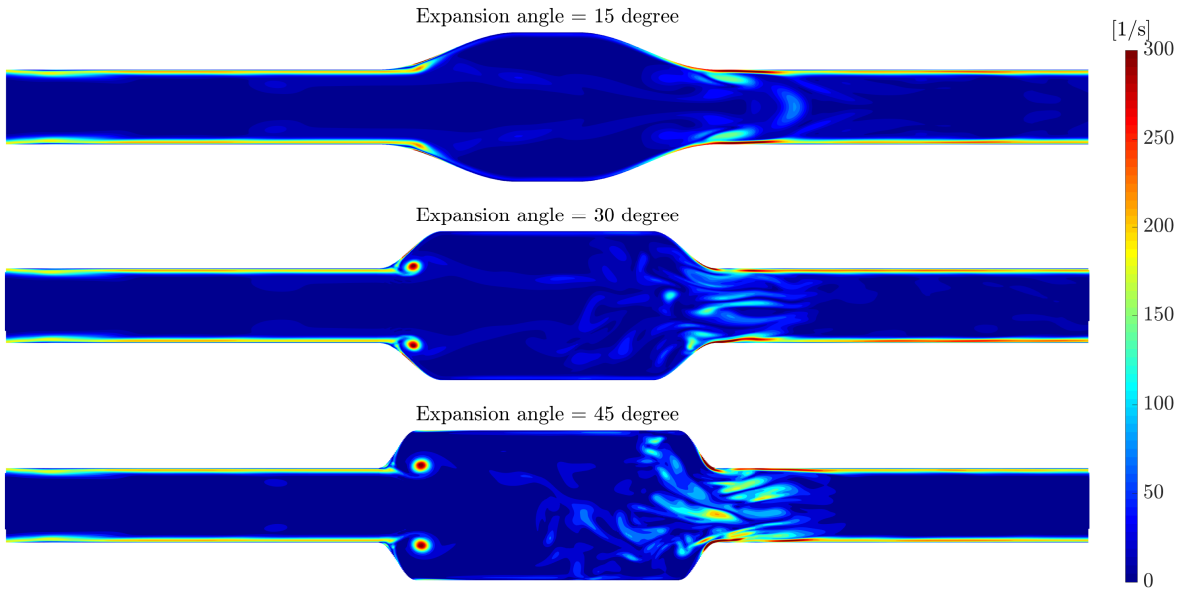

Figure 5.30: Separation of rolled up shear layer at $\phi = 0.4$ for the cases with an ER of 2 illustrated through vorticity contours. The shear layer has not separated for the EA of 15° (case 4), is in the process of separating for $30°$ (case 5) and has completely separated for $45°$ (case 6).

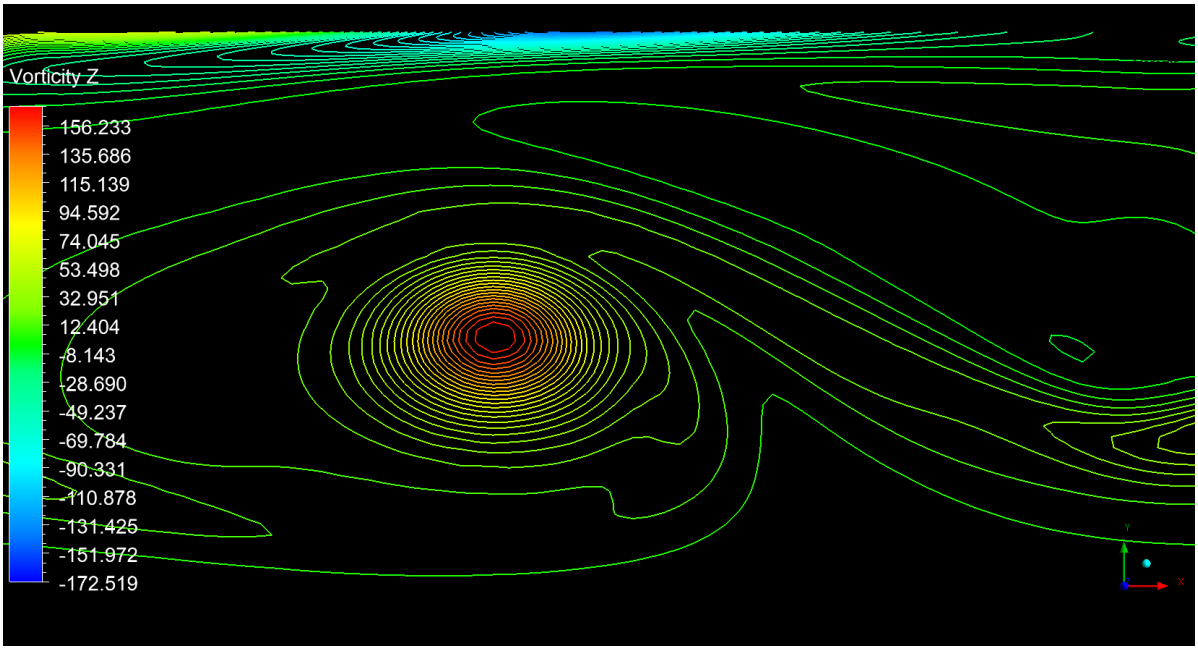

Figure 5.31: Contour plot of induced surface vorticity on the arterial wall. The induced vorticity has opposite sign of the near wall vortex core. Contours depicted are of Z vorticity.

Initially, at the time of roll up and formation of the vortex ring, the vortex ring is adjacent to the inclined radial wall of the expansion region of the 4A geometry. Thus, the induced vorticity on the arterial wall pushes the vortex core away until the distance between the core and the arterial wall attains a constant value. Since the vortex ring formed for cases with EA = 15° is closer to the aneurysm wall (as

it separates from the wall later), the change in their core trajectory is the highest. Case 6 surprisingly also shows a continuous change in the core trajectory. This is perhaps due to the early onset and growth of the azimuthal instability that causes the ring to break up as early as at $\phi = 0.8$.

5.5.2. Stability of the Vortex Ring

As illustrated earlier in figure 5.24, an azimuthal instability develops on the vortex ring for all the cases. The number of waves developed varies from case to case but in general, it decreases as the ER increases. Such an azimuthal instability has been the subject of numerous investigations [52–59] and it is beyond the scope of the current text to present a detailed discussion on it. The interested reader should refer to the monograph by Saffman [60] for a detailed quantitative treatment of the instability. However, a brief qualitative treatment of the instability is presented here.

Maxworthy [61] was one of the first authors to report this instability in 1972. From his experiments, he observed that the appearance of this instability depended on the initial Reynolds number $Re_0 = U_0 a_0/\nu$ where U_0 is the initial bubble translational velocity and a_0 is the initial bubble diameter. For $Re_0 \gtrsim 600$, the ring developed the azimuthal instability that grew in amplitude as the ring advected downstream. For case 5, $Re_0 \approx 0.11 * 0.024 * 1056/0.0035 \approx 800$ and it is reasonable to assume that the vortex rings generated in other cases too will have a similar Re_0. Thus, going by Maxworthy's criteria, occurrence of the azimuthal instability is expected in all the cases. Further, Maxworthy attributed this instability to the formation of an unstable layer/ interface formed on the outside of the ring as a result of vorticity of opposite sign, formed on the nozzle wall, being swept into the vortex core. Figure 5.32 illustrates this process wherein negative vorticity is swept into a positive vorticity core. Although such an explanation seems to be reasonable, an effort to quantitatively study the destabilizing effect of the unstable interface was never made and this theory was not pursued further by anyone.

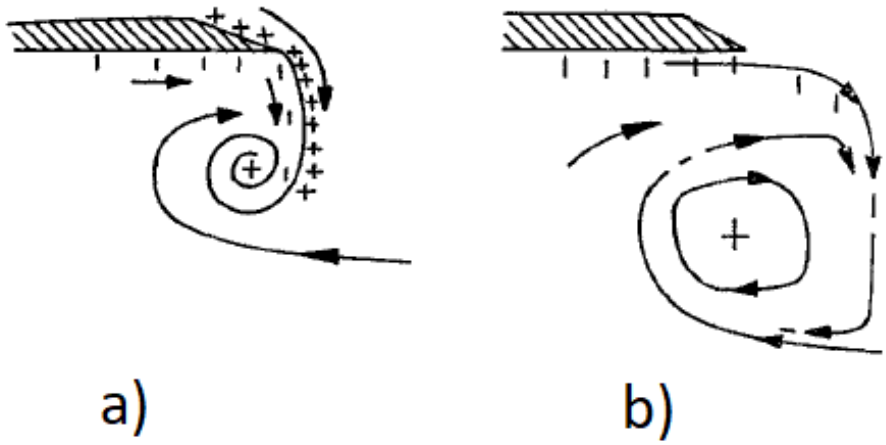

Figure 5.32: Vorticity of negative sign being swept into the positive vorticity core that leads to the creation of an unstable interface at the outer edge of the vortex ring. Reproduced from [61].

Around the same time as Maxworthy, Widnall and co-workers [52–54] carried out a series of numerical investigations on the azimuthal instability. Their approach was somewhat based on the idea of investigating the stability of a vortex pair subject to perturbation waves of infinitesimal amplitude. It is possible to take such an approach as from a local frame of reference, the core of a thin vortex ring looks like a straight tube. It should be noted that the infinitesimal perturbation waves are commonly referred to as Kelvin waves as Kelvin was the first one to investigate the stability of a Rankine vortex subject to such waves in 1880 [62]. Apart from inducing a translational velocity on itself, a vortex ring also induces a local straining field in the meridional plane or the XY plane for the cases considered in this thesis. Such a strain field breaks the circular symmetry of the vortex ring core and causes the core streamlines to become elliptical with the streamlines oriented at $45°$ to the principal stretching axis, as illustrated in figure 5.33. Although figure 5.33 is intended to illustrate the straining caused by a point vortex on another counter rotating point vortex, the straining effect will be present to a similar extent in a thin vortex ring. This strain field modifies the base flow field and can cause a resonance between two Kelvin modes whose azimuthal wavenumbers differ by 2 [55]. This leads to the amplification of the perturbations thus destabilising the vortex ring. The axial wavelength of the perturbations is typically lesser than the distance between the vortex pair (equal to the vortex ring diameter in this thesis) which is in stark contrast with Crow's instability; another instability usually observed in a vortex pair in which the wavelength is an order of magnitude higher than the distance between the vortex pair. Thus, the observed instability mechanism is referred to as a short wave instability and Crow's instability is referred to as a long wave instability. Since an essential ingredient of the short wave instability is the deformation of circular streamlines to elliptical streamlines in the vortex ring core, it is also sometimes referred to as an elliptical instability [55].

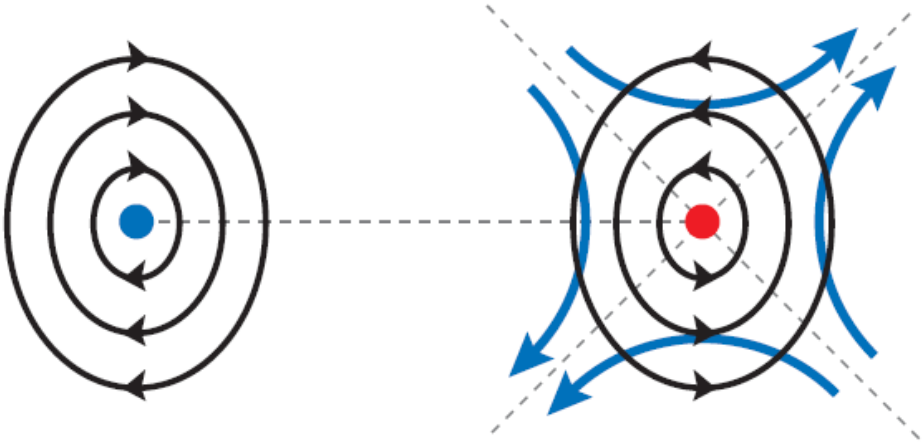

Figure 5.33: Straining of circular streamlines to elliptical streamlines around a point vortex (red) due to the presence of a counter rotating point vortex (blue). Black arrows depict the streamlines and the coloured arrows depict the strain induced. Reproduced from [55].

It should be kept in mind that a direct quantitative comparison of the observed instability in the current work is not possible with the analysis carried out by previous researchers since the assumptions frequently used such as thin core rings and inviscid fluid are not valid for the 4A vortex rings. Nonetheless, laboratory generated vortex rings also display the azimuthal instability [49] which indicates that even when the aforementioned assumptions are not strictly valid, the underlying physics is the same; the assumptions only simplify the mathematical calculations involved. The final breakdown of the ring occurs when the ring interacts with the remnants of the previous flow field that have random vorticity instead of a somewhat organised vorticity such as in the distorted ring. Also, just before complete breakdown secondary vorticity develops along the circumference of the vortex ring. Due to this secondary vorticity, streamwise vortices are shed in the wake of the vortex ring, as illustrated in figure 5.34. The interaction of these streamwise vortices with the distorted ring further promotes its breakdown.

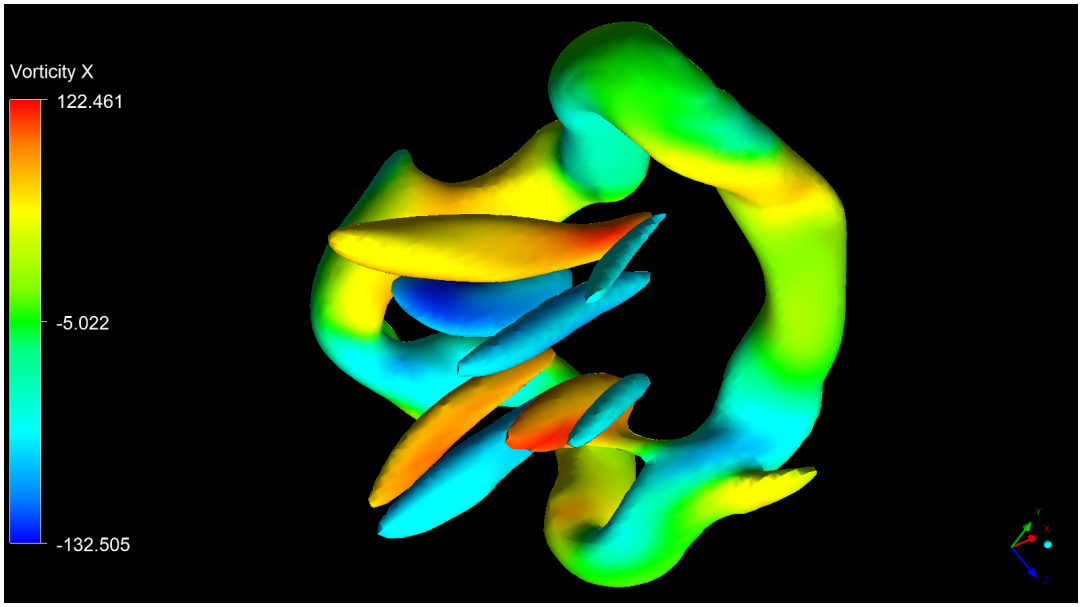

Figure 5.34: Shedding of streamwise vortices in the wake of the vortex ring. The secondary vorticity can be seen at the sharp kinks on the circumference of the vortex ring. Visualisation is done through streamwise vorticity coloured iso surface of Q criterion.

5.5.3. Evolution of the Vortex Ring

According to Maxworthy [61], the volume of fluid moving along with the ring is considerably larger than just a circular disc of thickness equal to the vortex core. As mentioned earlier, the entire fluid volume is referred to as a bubble. Maxworthy showed in his article that vorticity is distributed throughout the bubble volume and not just in a thin core, as suggested by classical thin core models. The vorticity distribution for case 5 was illustrated earlier in figure 5.26 from which Maxworthy's observation is confirmed for a confined ring also. It was also reported in [61] that the translation speed of the bubble decreases exponentially as it moves downstream. This primary reason for the exponential decrease is that the bubble size increases due to entrainment of irrotational fluid thereby resulting in the spread

of available vorticity over a larger bubble volume. Irrotational fluid flows over the bubble surface and dissipates surface vorticity. It then has insufficient total pressure to flow completely over the bubble surface and thus ends up being entrained from the rear side thereby increasing the bubble volume. Maxworthy also noted that vorticity was being rejected to a wake which, due to its distance from the bubble had no effect on its translational motion. Thus, the bubble velocity keeps decreasing as it travels downstream. Figures 5.35 and 5.36 illustrate the increase in size of the bubble and the increase in vortex core diameter due to entrainment of irrotational fluid, respectively.

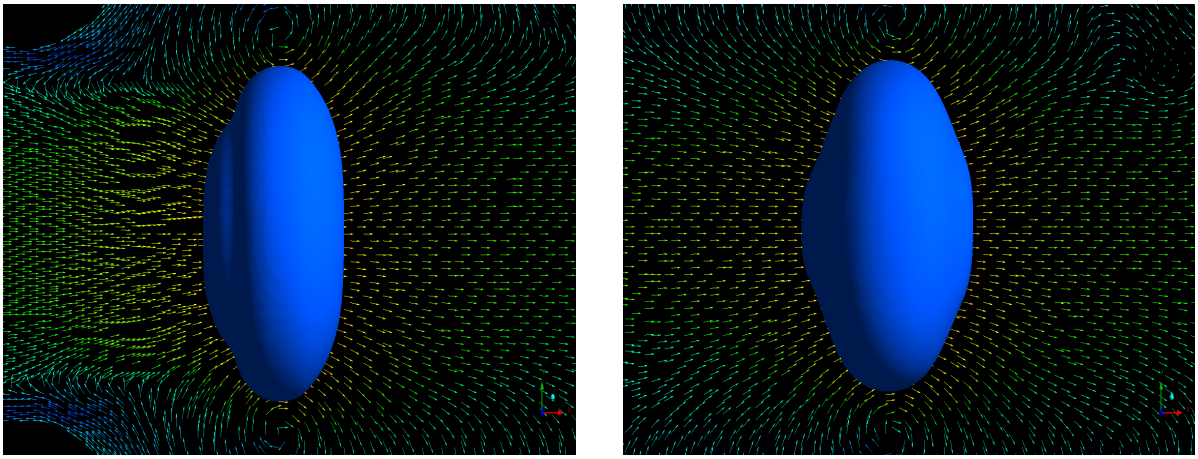

(a) $\phi = 0.5$ (b) $\phi = 0.7$

Figure 5.35: Increase in the volume of fluid or vortex 'bubble' as it travels downstream. The bubble is illustrated through an iso surface of axial velocity.

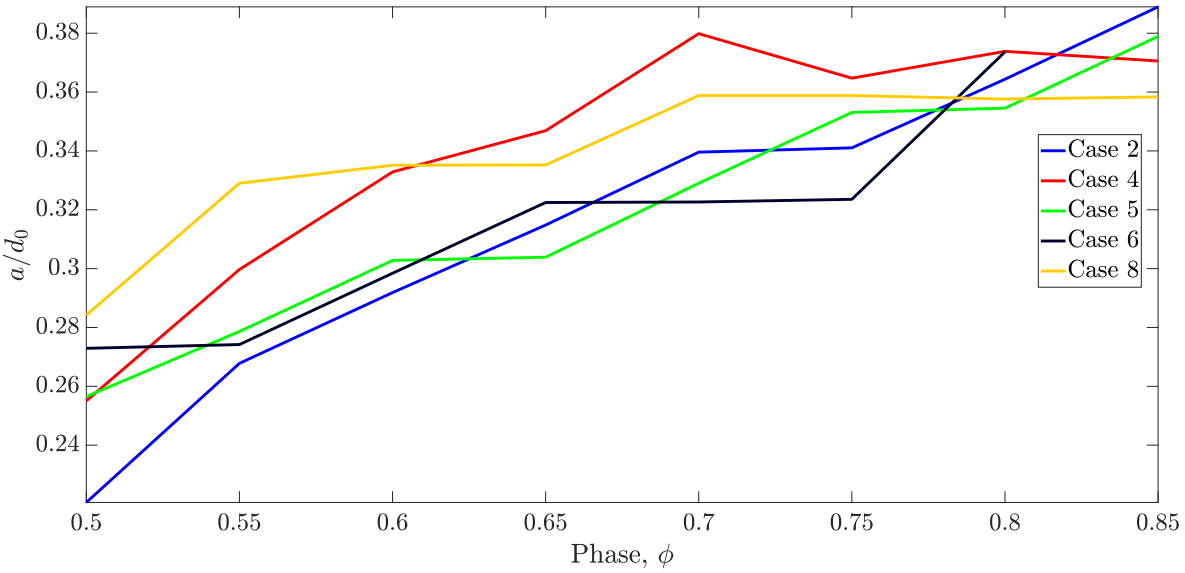

Figure 5.36: Increasing vortex core diameter with phase progression in a cardiac cycle. The core diameter (a) is normalized with the healthy aorta diameter (d_0). The entrainment of surrounding irrotational fluid results in the enlargement of the core. Phases only till $\phi = 0.85$ are shown since after this the ring breaks up. For case 6, the vortex ring breaks earlier at $\phi = 0.8$.

From the figures, it is clear that observations reported for unconfined vortex rings regarding their evolution are also observed for vortex rings formed in 4A geometries. But it is also important to account for the effect of the axisymmetric walls on the vortex rings in 4A geometries. As mentioned earlier, Stewart et al [50] show that the chief difference between confined and unconfined vortex rings is that surface vorticity of opposite sign is induced by the near wall vortex core on the walls of a confined domain. The interaction of the opposite sign vorticities leads to cross diffusive annihilation resulting in a decrement of vorticity and thereby circulation of the vortex core as the ring travels downstream. Naturally, a more confined domain will lead to higher interaction and thus a faster circulation decay. The circulation of the vortex core formed in selected cases is plotted in figure 5.37.

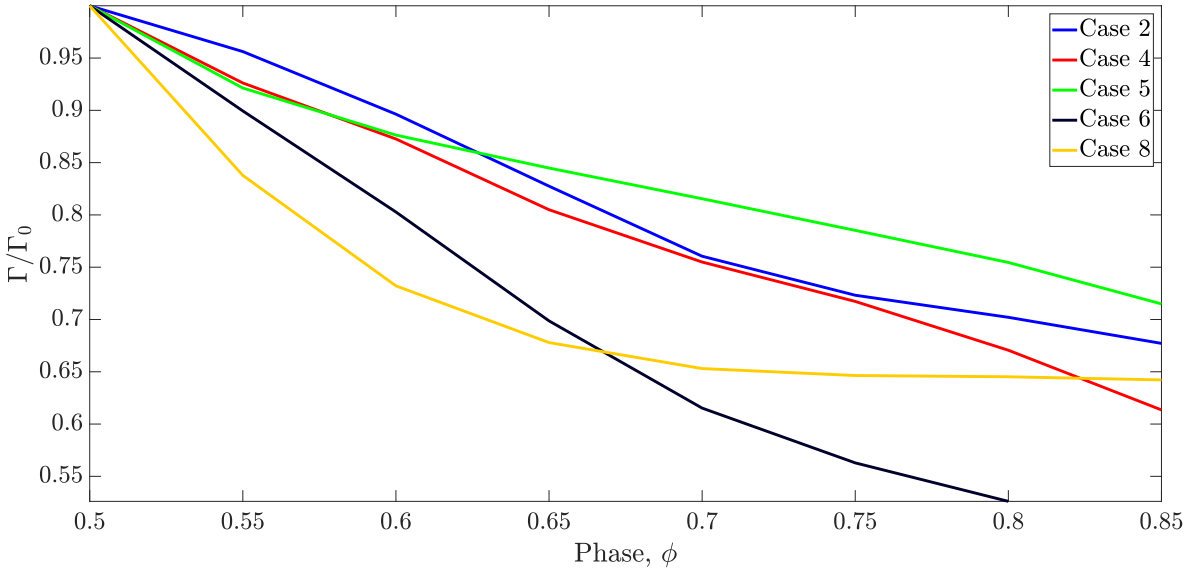

Figure 5.37: Vortex core circulation decay trend with phase progression in a cardiac cycle. The circulation value of each case is normalised with the maximum circulation (Γ_0) observed for the respective case. Phases only till $\phi = 0.85$ are shown since after this the ring breaks up. For case 6, the vortex ring breaks earlier at $\phi = 0.8$.

A clear decay of the circulation around the vortex core can be seen. A direct comparison of the decay rate across the illustrated cases is not really possible due to growth of the azimuthal instability which is different in every case. It is also important to realize that figure 5.37 depicts the total circulation reduction rate. This includes both, decay due to interaction with the opposite sign wall vorticity (shown in figure 5.31) and due to increase in bubble size (shown in figure 5.35). The growth of the azimuthal instability can also contribute to the decay rate as waves grow in amplitude in preferential directions (thereby coming in close approach to the wall) which will lead to a higher decay in that part of the ring. The amount of vorticity lost due to each factor can only be obtained through a detailed quantitative model which can be developed in a future study.

6

Conclusions & Recommendations

This chapter presents the conclusions and future outlook of this thesis. All the results, observations and inferences are summarised in section 6.1. Possible avenues for further investigation and ideas for building up on the current work are presented in section 6.2.

6.1. Conclusion

The objective of this project was to investigate turbulence in an AAA and how the geometric parameters, namely expansion ratio (ER) and expansion angle (EA), affect turbulence. In order to do so, 8 geometries with varying ER and EA were created keeping the physicality of the values in mind. The consequent impact of turbulence on a hemodynamic parameter such as the Oscillatory Shear Index (OSI) is also investigated. The following conclusions can be drawn from the results presented in the previous chapter.

1. A vortex ring is shed once every cardiac cycle just after peak systole. The breakup of this ring into smaller vortices causes fluctuations in the flow field which leads to turbulence.

2. The breakup of the vortex ring is initiated by the onset of an azimuthal instability. The number of waves formed on the ring vary from case to case but in general show a strong dependence on the expansion ratio of the aneurysm.

3. The vortex ring does not break down in all the cases simulated. In particular, it does not break down for the two cases with an expansion angle of 15°. This suggests that there seems to be a critical expansion angle threshold below which the vortex ring does not break.

4. The underlying mechanism of the vortex ring breakdown is different from case to case and depends on the geometric parameters of the AAA. In general, if the AAA has a reasonably long streamwise length, the ring breaks down well within the AAA but for shorter AAAs the breaks down occurs at the aneurysm exit after interaction with the distal neck.

5. There seems to be no clear co-relation between turbulence and the OSI. This can be attributed to the fact that turbulence in AAAs is in the bulk of the domain and thus, the velocity field near the wall is unaffected by it. Thus, turbulence and OSI appear to be well decoupled from each other.

6. The highest region of mean (cycle averaged) wall shear stress is found at the distal neck and not at the region of maximum diameter. Rather, the aneurysm surface displays significantly less WSS than the proximal or distal neck which further demonstrates the shortcoming of the threshold diameter criteria in clinical practice.

7. The inflection regions, in particular the expansion region of an AAA, are highly susceptible to the formation of an intraluminal thrombus (ILT) or a dead flow region. Formation of an ILT leads to local hypoxic conditions that deteriorate the surrounding arterial tissue thereby increasing the risk of rupture. In general, the severity of an ILT increases with the expansion ratio of an AAA.

6.2. Recommendations for Future Research

The current thesis can further be extended with the following ideas

1. Only the geometric parameters of an AAA were varied in this thesis. Flow parameters such as the Reynolds number and the Womersley number can also be varied to see the impact on turbulence. Although the values taken for the flow parameters in this thesis represent the average value, they can be considerably different in specific scenarios such as under exercise conditions.

2. Blood is assumed to behave in a Newtonian fashion and although the non Newtonian nature is reasoned to be negligible in the current problem (section 2.4), it can lead to a slightly different flow field. A non Newtonian study could highlight the differences in the flow field and whether the differences are within reasonable limits for blood flow in AAAs.

3. The elastic nature of the arterial wall can be included to see its effect on the flow field. A combined flow structure interaction (FSI) study will be required to allow for the remodelling of the arterial wall in response to the flow field and then observe the effect on the flow field as a result of the remodelling process. In this way, the simulation will mimic reality as closely as possible.

4. It is highlighted that turbulence in AAAs is a consequence of the breakdown of the vortex ring that is shed once every cycle. Although a detailed qualitative discussion is presented in section 5.5 regarding the general structure of the ring and the onset of an azimuthal instability, an attempt to present a quantitative model depicting the same is not made. A quantitative model will lead to

a better understanding of the motion of a vortex ring in axisymmetric wall bounded pulsatile flow fields.

5. It was shown that for the 3 values of ER simulated, the average turbulence intensity first increases and then decreases with an increase in ER. Since only 3 values of ER are simulated, the exact trend is not clearly highlighted. More values of ER can be simulated at a constant EA to better illustrate this trend. Likewise, more values for EA can also be simulated keeping the ER constant.

6. In this thesis, the inlet velocity is perturbed to trigger turbulence. Other forms of perturbation such as an inlet swirl component or a geometric perturbation can also be tested to trigger turbulence.

A

Appendix

A.1. Parameters for all harmonics used in Fourier decomposition

It was shown in section 3.4.1 that the inlet velocity can be represented through a sum of 19 Fourier harmonics. The parameters of all the 19 harmonics in equation 3.14 are shown in the table below.

$n[-]$	$M_n[cm^3/s]$	ϕ_n	$n[-]$	$M_n[cm^3/s]$	ϕ_n
0	5.7707	0	10	0.5080	+0.1822
1	5.7439	-2.2214	11	0.7770	-1.8666
2	5.2869	+1.9232	12	0.6569	+2.1061
3	4.6235	-0.2006	13	0.4597	+0.1344
4	2.1714	-2.3405	14	0.2820	-1.4256
5	1.3435	+2.8339	15	0.3636	+3.0315
6	1.2711	+1.0875	16	0.3414	+0.8361
7	1.5537	-0.8632	17	0.3171	-1.3357
8	1.0586	-3.1250	18	0.1604	+2.8307
9	0.6109	+1.5654	19	0.7770	+1.1774

Table A.1: Parameters of all the 19 Fourier harmonics

A.2. Inlet Velocity Profile UDF for all 4A cases

```
#include "udf.h"

#define pi 4*atan(1)
#define R 11e-3
#define mf 2.9772
#define T 0.8
#define A pi*pow(R,2)

real q, umax;

DEFINE_PROFILE(x_velocity,t,i)
{
  real pos[ND_ND], y, z, r, time;
  face_t f;
  begin_f_loop(f,t)
  {
    F_CENTROID(pos,f,t);
    time = CURRENT_TIME;
    y = pos[1];
    z = pos[2];
    r = sqrt(pow(y,2) + pow(z,2));
    q = 5.7707 +\
    5.7439*cos(2.*pi*1.*(time/T) - 2.2214) +\
    5.2869*cos(2.*pi*2.*(time/T) + 1.9232) +\
    4.6235*cos(2.*pi*3.*(time/T) - 0.2006) +\
    2.1714*cos(2.*pi*4.*(time/T) - 2.3405) +\
    1.3435*cos(2.*pi*5.*(time/T) + 2.8339) +\
    1.2711*cos(2.*pi*6.*(time/T) + 1.0875) +\
    1.5537*cos(2.*pi*7.*(time/T) - 0.8632) +\
    1.0586*cos(2.*pi*8.*(time/T) - 3.1250) +\
    0.6109*cos(2.*pi*9.*(time/T) + 1.5654) +\
    0.5080*cos(2.*pi*10.*(time/T) + 0.1822) +\
    0.7770*cos(2.*pi*11.*(time/T) - 1.8666) +\
    0.6569*cos(2.*pi*12.*(time/T) + 2.1061) +\
    0.4597*cos(2.*pi*13.*(time/T) + 0.1344) +\
    0.2820*cos(2.*pi*14.*(time/T) - 1.4256) +\
    0.3636*cos(2.*pi*15.*(time/T) + 3.0315) +\
    0.3414*cos(2.*pi*16.*(time/T) + 0.8361) +\
    0.3171*cos(2.*pi*17.*(time/T) - 1.3357) +\
```

```
    0.1604*cos(2.*pi*18.*(time/T) + 2.8307) +\
    0.1001*cos(2.*pi*19.*(time/T) + 1.1774);
    q = (6.0/3.0)*q;
    umax = (6.0*q*1e-6*mf)/(5.0*A);
    F_PROFILE(f,t,i) = umax*(1.0 - pow(r/R,10));
  }
  end_f_loop(f,t)
}

DEFINE_PROFILE(z_velocity,t,i)
{
  face_t f;
  begin_f_loop(f,t)
  {
    F_PROFILE(f,t,i) = umax*5.0*0.01/6.0;
  }
  end_f_loop(f,t)
}
```

A.3. Validation Case Inlet Velocity UDF

The validation case [20] had a sinusoidal inlet velocity waveform. As shown in section 2.1, solution to a purely oscillatory axisymmetric flow exists. Thus, equation 2.16 is prescribed as the inlet velocity. C routine to compute Bessel function of complex arguments is adopted from [63].

```
#include "udf.h"
#include "math.h"
#include "complex.h"
#include "stdlib.h"

#define pi 4*atan(1)
#define R 11e-3
#define d 22e-3
#define T 4.08
#define A 2/3
#define alpha 7.5
#define  MAXK  20

double u_c;
double HALF = 0.5, ONE = 1.0, FPF = 5.5;
double z[2], z1[2],z2[2];
int nu = 0;
```

```
18
19  void CDIV(double *Z1, double *Z2, double *Z) {
20    double D;
21    D=Z2[0]*Z2[0]+Z2[1]*Z2[1];
22  if (D > 1e30) {
23       Z[0]=0.0; Z[1]=0.0; return;
24    }
25    if (D == 0) return;
26    Z[0]=(Z1[0]*Z2[0]+Z1[1]*Z2[1])/D;
27    Z[1]=(Z1[1]*Z2[0]-Z1[0]*Z2[1])/D;
28  }
29
30
31  void CMUL(double *Z1, double *Z2, double *Z) {
32    Z[0]=Z1[0]*Z2[0] - Z1[1]*Z2[1];
33    Z[1]=Z1[0]*Z2[1] + Z1[1]*Z2[0];
34  }
35
36
37  void IZPower(double *z, int n, double *z1) {
38    double temp[2],temp1[2]; int i;
39  if (n==0) {
40       z1[0]=1.0;
41    z1[1]=0.0;
42    }
43  else if (n==1) {
44       z1[0]=z[0];
45    z1[1]=z[1];
46    }
47  else {
48    temp1[0]=z[0]; temp1[1]=z[1];
49    for (i=2; i<=n; i++) {
50      CMUL(temp1,z,temp);
51      temp1[0]=temp[0];
52      temp1[1]=temp[1];
53    }
54      z1[0]=temp[0];
55    z1[1]=temp[1];
56    }
57  }
58
```

```
  double Fact(int k) {
    int i; double f;
    f=ONE;
    for (i=2; i<=k; i++)  f *= ONE*i;
    return f;
  }

/****************************************
*           FUNCTION  GAMMA(X)          *
* ------------------------------------ *
* Returns the value of Gamma(x) in double *
* precision as EXP(LN(GAMMA(X))) for X>0. *
****************************************/
double Gamma(double xx) {
  double cof[6];
  double stp,x,tmp,ser;
  int j;
  cof[0]=76.18009173;
  cof[1]=-86.50532033;
  cof[2]=24.01409822;
  cof[3]=-1.231739516;
  cof[4]=0.120858003e-2;
  cof[5]=-0.536382e-5;
  stp=2.50662827465;
  x=xx-ONE;
  tmp=x+FPF;
  tmp=(x+HALF)*log(tmp)-tmp;
  ser=ONE;
  for (j=0; j<6; j++) {
    x += ONE;
    ser += cof[j]/x;
  }
  return (exp(tmp+log(stp*ser)));
}

void CBESSJ(double *z, int nu, double *z1)  {
/*-------------------------------------------------
                        inf.     (-z^2/4)^k
    Jnu(z) = (z/2)^nu x Sum  -----------------
                        k=0  k! x Gamma(nu+k+1)
   (nu must be >= 0). Here k=15.
```

```
100 ------------------------------------------------------*/
101   int k;
102   double sum[2],tmp[2],tmp1[2],tmp2[2],tmp3[2];
103   tmp[0]=2.0; tmp[1]=0.0;
104   CDIV(z,tmp,tmp1);
105   IZPower(tmp1,nu,tmp3);
106   sum[0]=0.0; sum[1]=0.0;
107   /*calculate Sum*/
108   for (k=0; k<=MAXK; k++) {
109     /* calculate (-z^2/4)^k*/
110     IZPower(z,2,tmp);
111     tmp[0]=-tmp[0]; tmp[1]=-tmp[1];
112     tmp1[0]=4.0; tmp1[1]=0.0;
113     CDIV(tmp,tmp1,tmp2);
114
115     if (z[1]==0) {              /*case real number*/
116       tmp[0]=pow(tmp2[0],k);
117     tmp[1]=0.0;
118     }
119   else                         /*case complex number*/
120       IZPower(tmp2,k,tmp);
121
122   /* divide by k!*/
123     tmp1[0]=Fact(k); tmp1[1]=0.0;
124   if (z[1]==0) {
125       tmp2[0]=tmp[0]/tmp1[0];
126     tmp2[1]=0.0;
127     }
128     else
129     CDIV(tmp,tmp1,tmp2);
130     /* divide by Gamma(nu+k+1)*/
131     tmp1[0]=Gamma(ONE*(nu+k+1)); tmp1[1]=0.0;
132
133   if (z[1]==0) {
134       tmp[0]=tmp2[0]/tmp1[0];
135     tmp[1]=0.0;
136     }
137     else
138       CDIV(tmp2,tmp1,tmp);
139     /* actualize sum*/
140     sum[0] += tmp[0];
```

```
141     sum[1] += tmp[1];
142
143   }
144   /* multiply (z/2)^nu by sum*/
145   CMUL(tmp3,sum,z1);
146
147 }
148
149 DEFINE_PROFILE(x_velocity,t,i)
150 {
151   double pos[ND_ND], yi, zi, r, time;
152     face_t f;
153   begin_f_loop(f,t)
154   {
155     F_CENTROID(pos,f,t);
156     time = CURRENT_TIME;
157     yi = pos[1];
158     zi = pos[2];
159     r = sqrt(pow(yi,2) + pow(zi,2));
160     u_c = 0.09;
161     z[0] = cos(3*pi/4)*alpha*2*r/d;
162     z[1] = sin(3*pi/4)*alpha*2*r/d;
163     CBESSJ(z,nu,z1);
164     double _Complex num = z1[0] + _Complex_I*z1[1];
165
166     z[0] = cos(3*pi/4)*alpha;
167     z[1] = sin(3*pi/4)*alpha;
168     CBESSJ(z,nu,z1);
169     double _Complex den = z1[0] + _Complex_I*z1[1];
170
171     double _Complex term = num/den;
172
173     F_PROFILE(f,t,i) = u_c*(1.0 - pow(r/R,2)) + (u_c*A*creal(1 - term)*sin(2*pi*((
      time/T)+0.1)));
174   }
175   end_f_loop(f,t)
176 }
```

A.4. Velocity Profiles at different Womersley Numbers

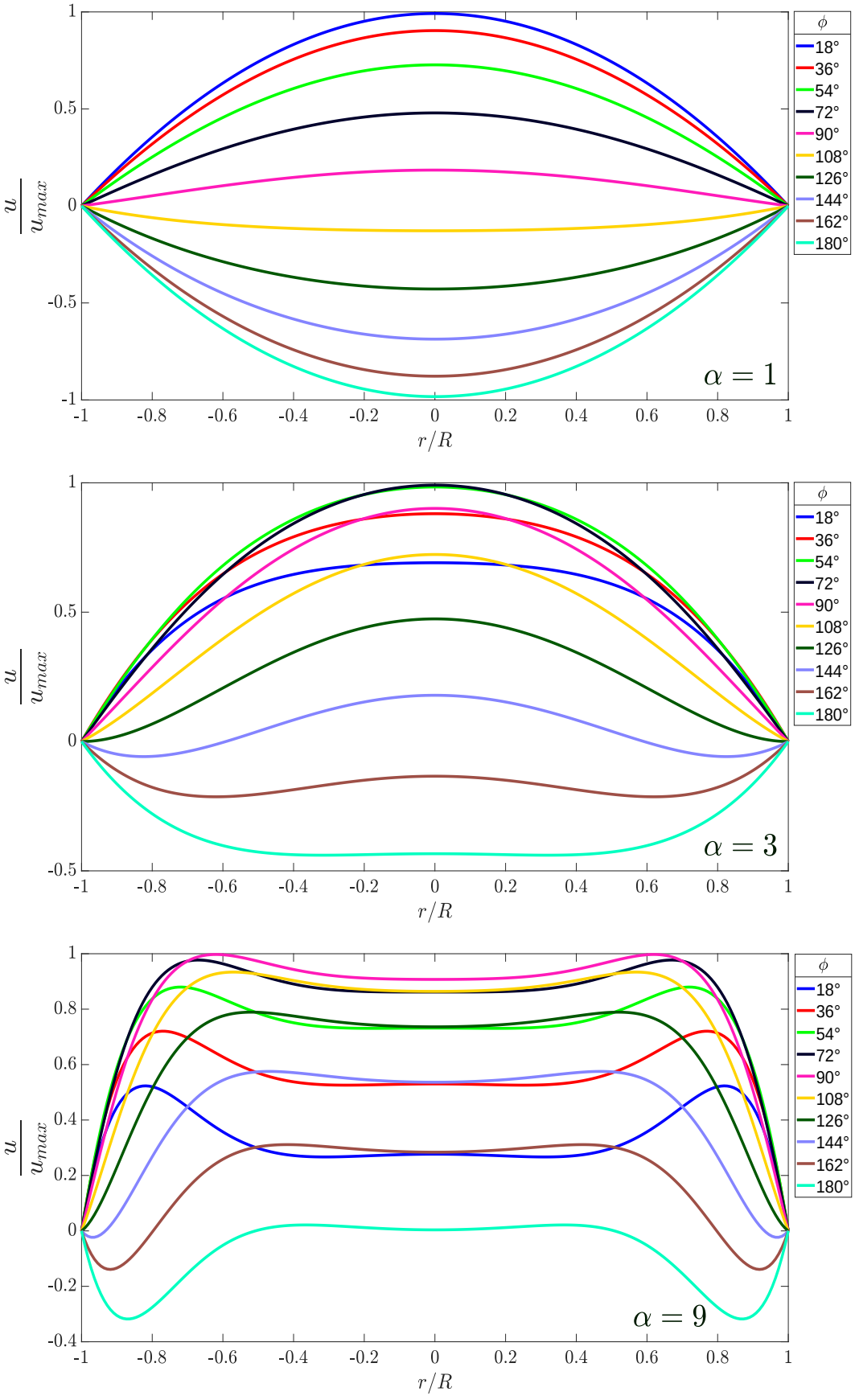

Figure A.1: Normalised velocity profiles at different phases of a purely oscillatory axisymmetric flow for various Womersley numbers (α). As α increases, the spatial variation of the velocity profile deviates increasingly from that of a parabola and flattens out at the centre.

A.5. Pressure & WSS Comparison

It was mentioned in section 2.5.4 that the wall normal pressure is multiple orders of magnitude higher than the flow induced WSS. Figures A.2 - A.5 compare the two for case 5 at selected phases. It can be clearly be seen that on an average, pressure is 2 to 3 orders of magnitude higher than the WSS thereby validating Vorp's [6] observation.

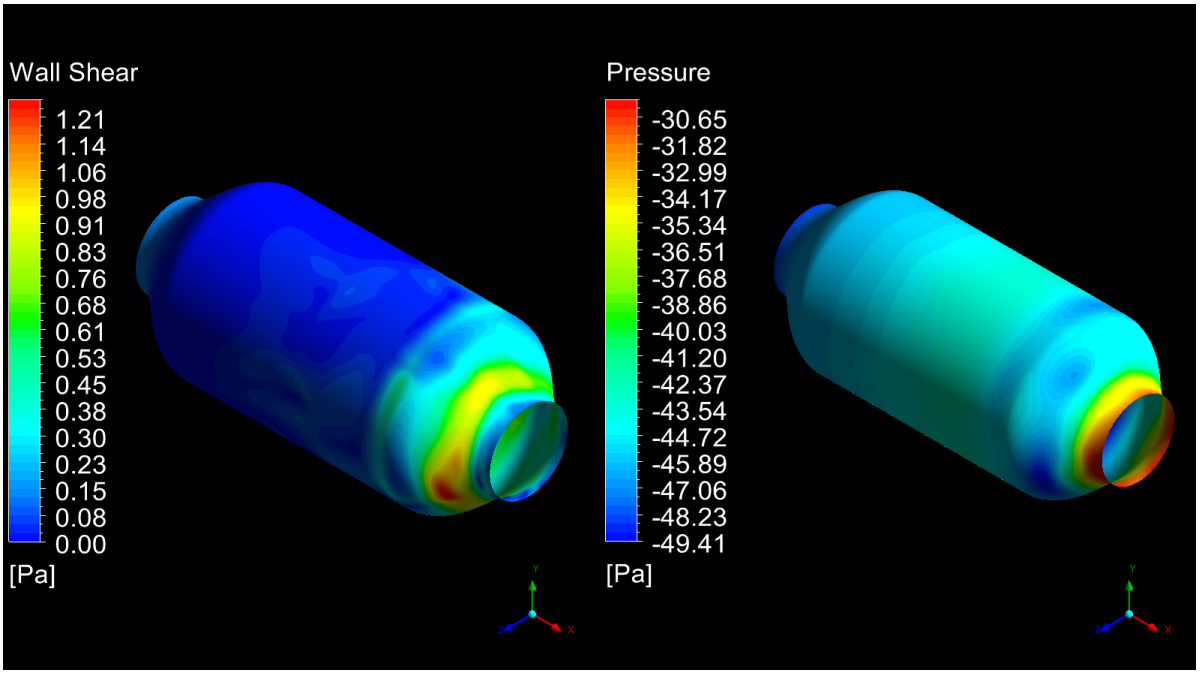

Figure A.2: Comparison between Pressure and WSS just before systolic acceleration ($\Phi = 0.2$)

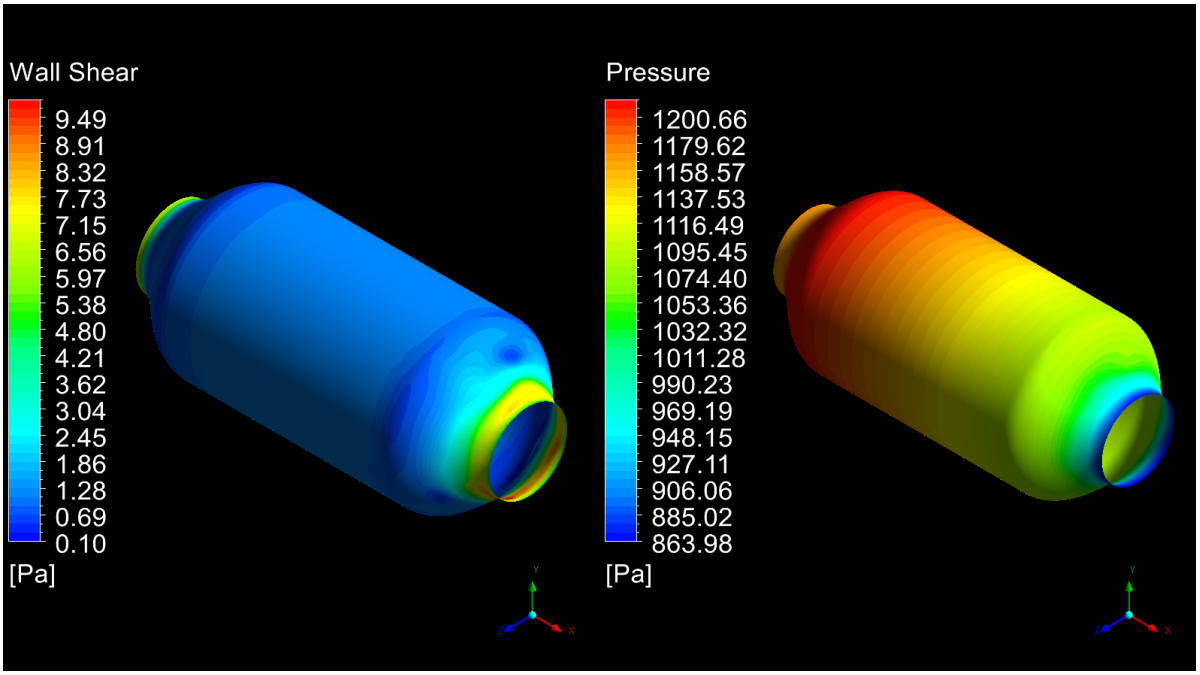

Figure A.3: Comparison between Pressure and WSS at peak systole ($\Phi = 0.3$)

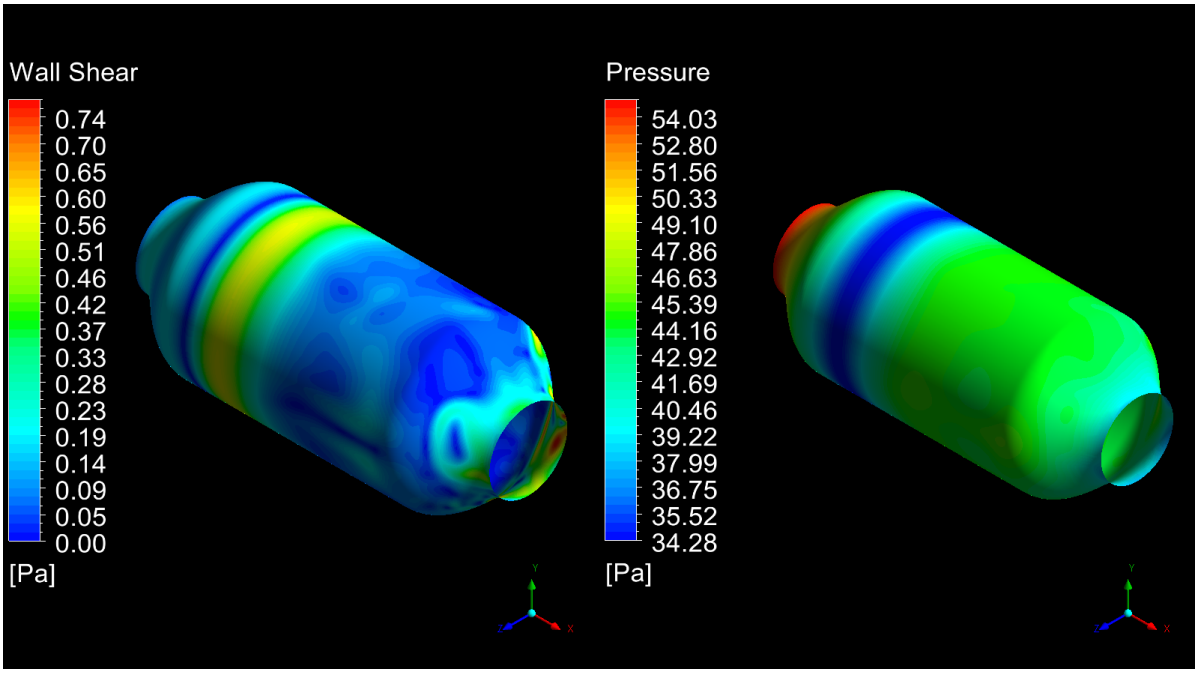

Figure A.4: Comparison between Pressure and WSS at $\Phi = 0.6$. The axisymmetric band of low pressure depicts the location of the vortex ring.

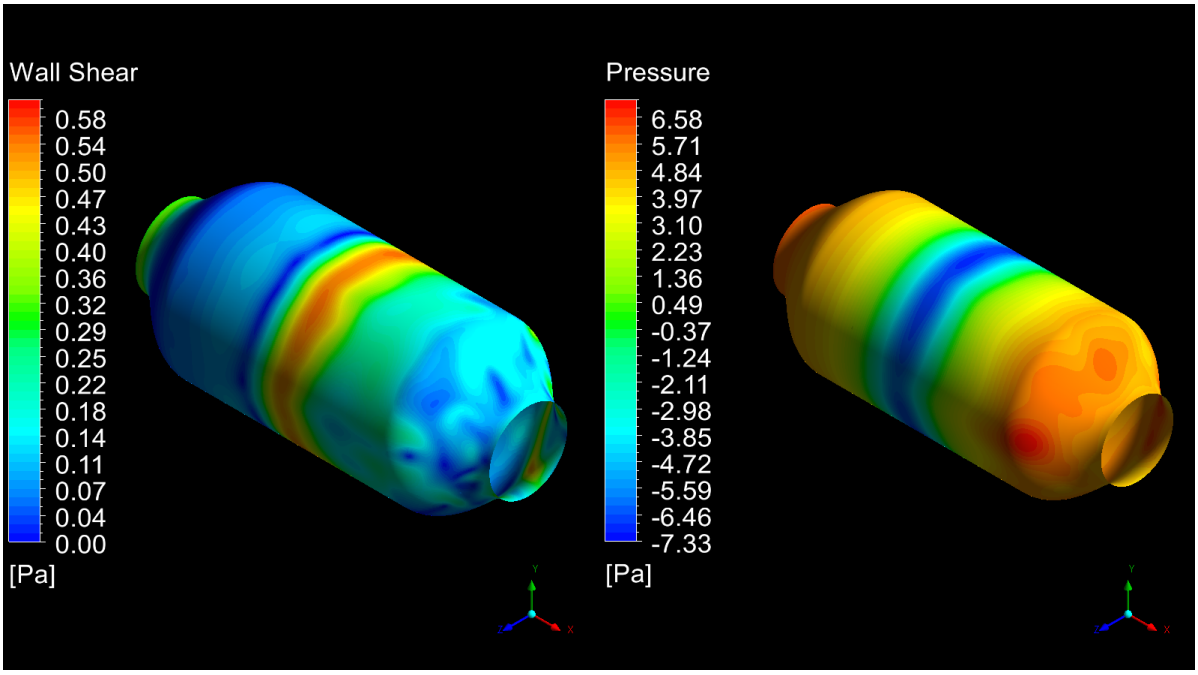

Figure A.5: Comparison between Pressure and WSS at $\Phi = 0.8$. The previously perfectly axisymmetric band of low pressure is now a bit distorted due to the growth of the azimuthal instability.

A.6. Additional Validation Results

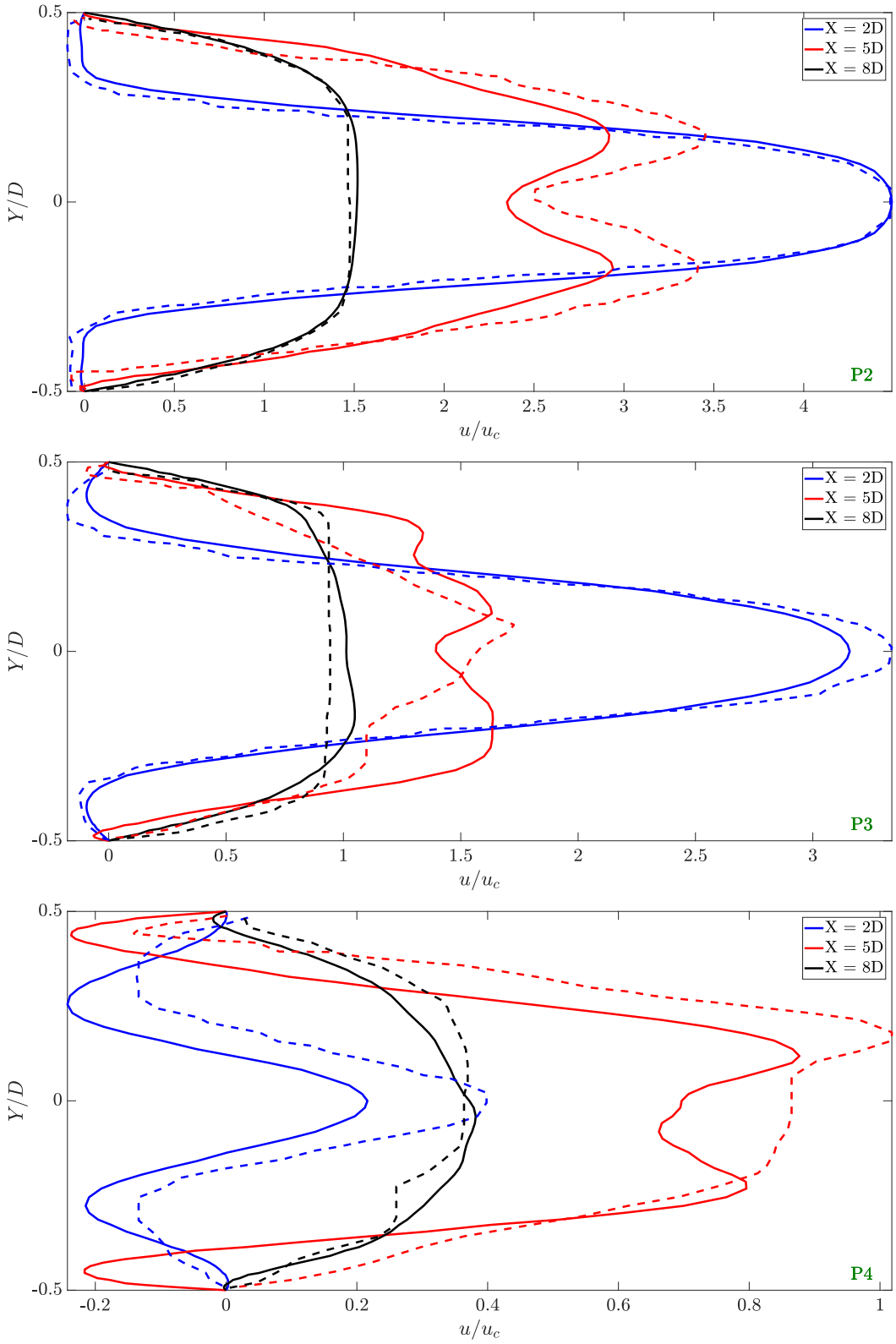

Figure A.6: Velocity profiles in the XY plane at various streamwise locations at phase 2,3 and 4. The authors' [20] profiles are indicated with dashed lines. At each location, good qualitative agreement can be seen.

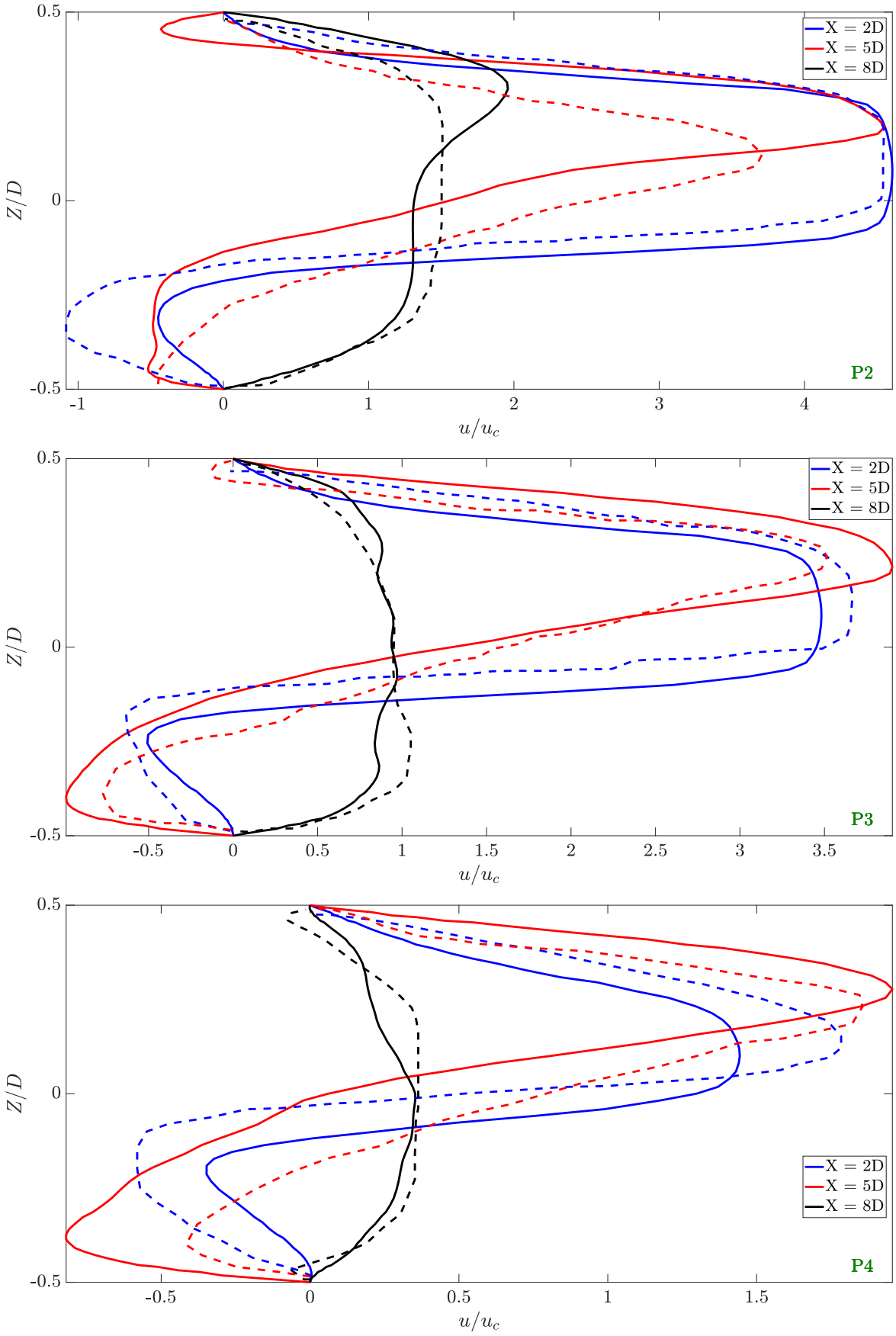

Figure A.7: Velocity profiles in the ZX plane at various streamwise locations at phase 2,3 and 4. The authors' [20] profiles are indicated with dashed lines. At each location, good qualitative agreement can be seen. It should also be noted that in the previous figure as well as the current figure, the authors' profiles were reconstructed from very low resolution plots and thus the agreement might actually be better than shown.

A.7. Overview of all the 4A Geometries

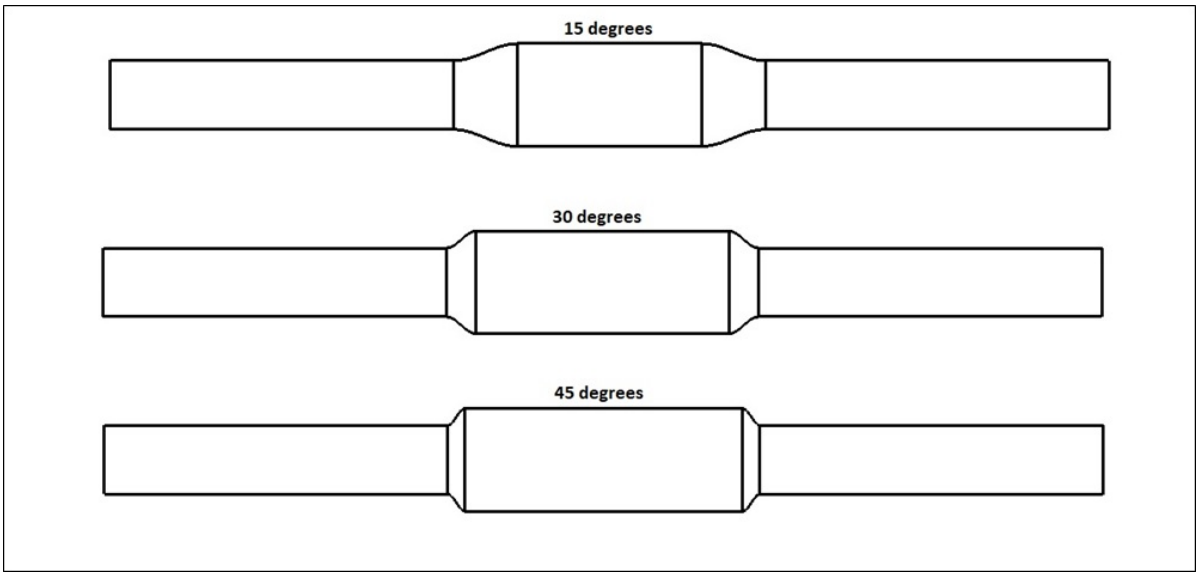

Figure A.8: 4A Geometries for ER = 1.5.

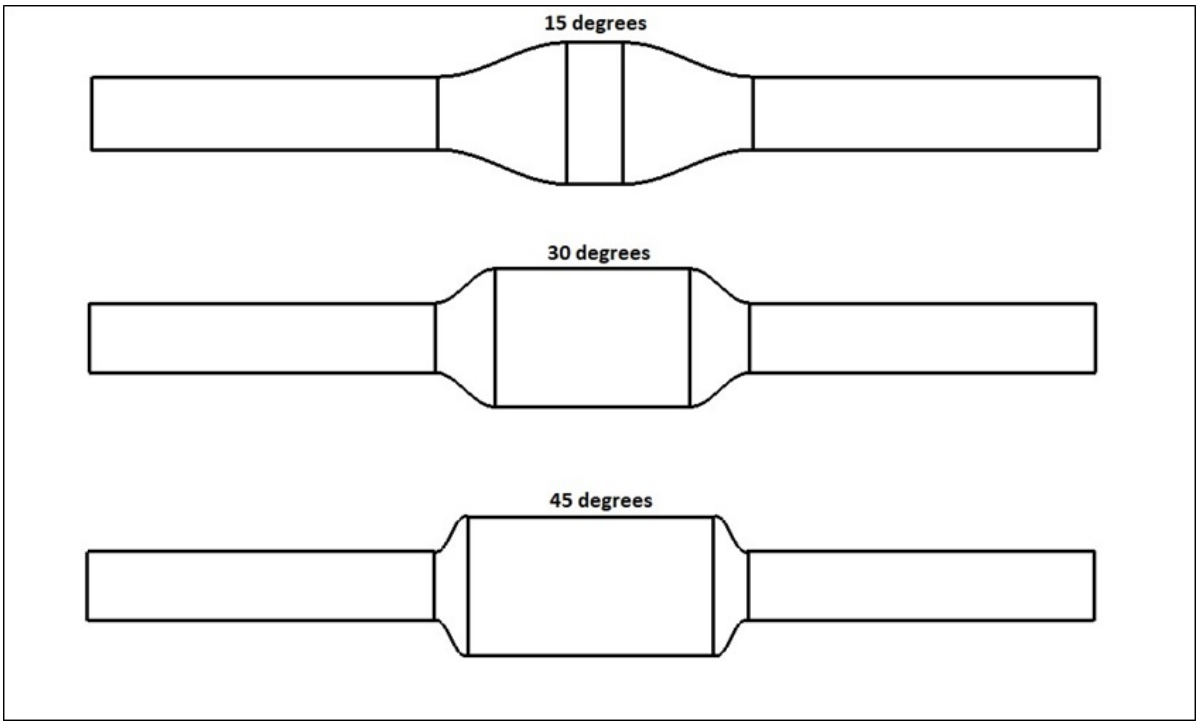

Figure A.9: 4A Geometries for Expansion Ratio = 2

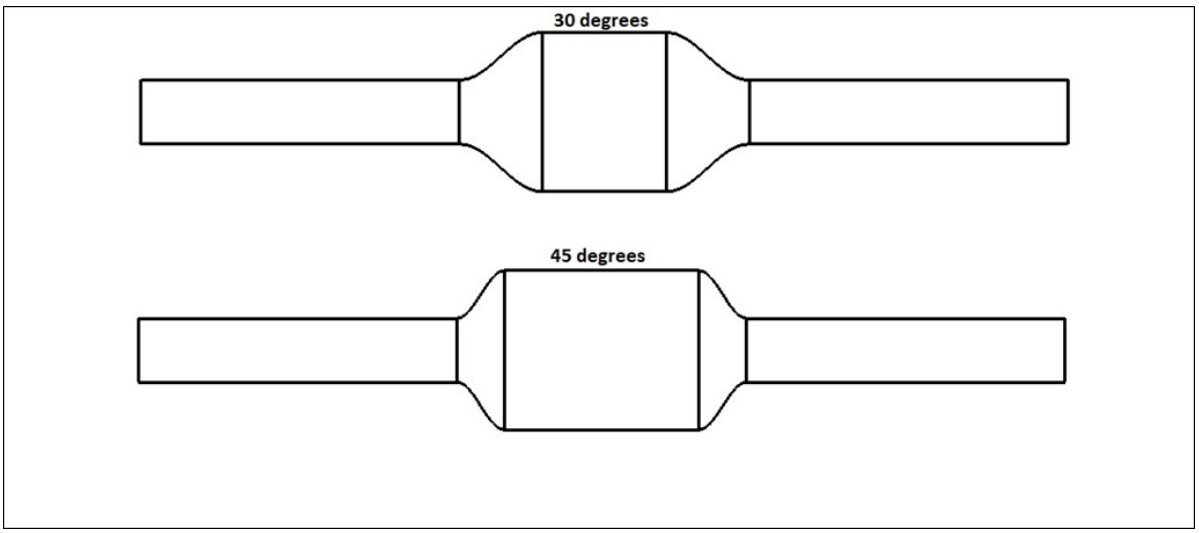

Figure A.10: 4A Geometries for Expansion Ratio = 2.5

Bibliography

[1] Gerard J Tortora and Bryan H Derrickson. *Principles of anatomy and physiology*. John Wiley & Sons, 2008.

[2] Alan T Hirsch, Ziv J Haskal, Norman R Hertzer, Curtis W Bakal, Mark A Creager, Jonathan L Halperin, Loren F Hiratzka, William RC Murphy, Jeffrey W Olin, Jules B Puschett, et al. ACC/AHA guidelines for the management of patients with peripheral arterial disease (lower extremity, renal, mesenteric, and abdominal aortic). *Journal of Vascular and Interventional Radiology*, 17(9):1383–1398, 2006.

[3] Singapore medical clinic. http://www.singaporemedicalclinic.com/abdominal-aortic-aneursym.

[4] Louise C Brown, Janet T Powell, et al. Risk factors for aneurysm rupture in patients kept under ultrasound surveillance. *Annals of Surgery*, 230(3):289, 1999.

[5] K Craig Kent. Abdominal aortic aneurysms. *New England Journal of Medicine*, 371(22):2101–2108, 2014.

[6] David A Vorp. Biomechanics of abdominal aortic aneurysm. *Journal of Biomechanics*, 40(9):1887–1902, 2007.

[7] SA Rahimi. Abdominal aortic aneurysm. *Emedicine/Medscape*, 2015.

[8] Saša Kenjereš and Alexander de Loor. Modelling and simulation of low-density lipoprotein transport through multi-layered wall of an anatomically realistic carotid artery bifurcation. J*ournal of The Royal Society Interface*, 11(91), 2013.

[9] Monica M Dua and Ronald L Dalman. Hemodynamic influences on abdominal aortic aneurysm disease: Application of biomechanics to aneurysm pathophysiology. *Vascular Pharmacology*, 53(1):11–21, 2010.

[10] David N Ku. Blood flow in arteries. *Annual Review of Fluid Mechanics*, 29(1):399–434, 1997.

[11] S Glagov, C Zarins, DP Giddens, and DN Ku. Hemodynamics and atherosclerosis. insights and perspectives gained from studies of human arteries. *Archives of Pathology & Laboratory Medicine*, 112(10):1018–1031, 1988.

[12] David N Ku, Don P Giddens, Christopher K Zarins, and Seymour Glagov. Pulsatile flow and atherosclerosis in the human carotid bifurcation. positive correlation between plaque location and low oscillating shear stress. *Arteriosclerosis, Thrombosis, and Vascular Biology*, 5(3):293–302, 1985.

[13] Jonathan P Vande Geest, Elena S Di Martino, Ajay Bohra, Michel S Makaroun, and David A Vorp. A biomechanics-based rupture potential index for abdominal aortic aneurysm risk assessment. *Annals of the New York Academy of Sciences*, 1085(1):11–21, 2006.

[14] Y Hirose and M Takamiya. Growth curve of ruptured aortic aneurysm. *Journal of Cardiovascular Surgery*, 39(1):9, 1998.

[15] David HJ Wang, Michel S Makaroun, Marshall W Webster, and David A Vorp. Effect of intraluminal thrombus on wall stress in patient-specific models of abdominal aortic aneurysm. *Journal of Vascular Surgery*, 36(3):598–604, 2002.

[16] Barry J Doyle, Anthony Callanan, Paul E Burke, Pierce A Grace, Michael T Walsh, David A Vorp, and Timothy M McGloughlin. Vessel asymmetry as an additional diagnostic tool in the assessment of abdominal aortic aneurysms. *Journal of Vascular Surgery*, 49(2):443–454, 2009.

[17] Pijush K Kundu, David R Dowling, Grétar Tryggvason, and Ira M Cohen. *Fluid Mechanics*. Academic press, 2015.

[18] John R Womersley. Method for the calculation of velocity, rate of flow and viscous drag in arteries when the pressure gradient is known. *The Journal of Physiology*, 127(3):553, 1955.

[19] Peter F Davies, Andrea Remuzzi, Ethel J Gordon, C Forbes Dewey, and Michael A Gimbrone. Turbulent fluid shear stress induces vascular endothelial cell turnover in vitro. *Proceedings of the National Academy of Sciences*, 83(7):2114–2117, 1986.

[20] Sonu S Varghese, Steven H Frankel, and Paul F Fischer. Direct numerical simulation of stenotic flows. part 2. pulsatile flow. *Journal of Fluid Mechanics*, 582:281–318, 2007.

[21] D.A. McDonald. *Blood flow in Arteries*. Monographs of the Physiological Society. E. Arnold, 1960.

[22] Wang Chang, Gao Pu-Zhen, Tan Si-Chao, and Xu Chao. Theoretical analysis of phase-lag in low frequency laminar pulsating flow. *Progress in Nuclear Energy*, 58:45–51, 2012.

[23] CJ Mills, IT Gabe, JH Gault, DT Mason, J Ross, E Braunwald, and JP Shillingford. Pressure-flow relationships and vascular impedance in man. *Cardiovascular Research*, 4(4):405–405, 1970.

[24] Ender A Finol and Cristina H Amon. Blood flow in abdominal aortic aneurysms: pulsatile flow hemodynamics. *Transactions-American Society of Mechanical Engineers Journal of Biomechanical Engineering*, 123(5):474–484, 2001.

[25] TJG Van Kruchten. *CFD Modeling of Abdominal Aortic Aneurysms*. Master's thesis, TU Delft, Netherlands, 2014.

[26] Hardy Schumacher, Hans H Eckstein, Friedrich Kallinowski, and Jens Rainer Allenberg. Morphometry and classification in abdominal aortic aneurysms: patient selection for endovascular and open surgery. *Journal of Endovascular Therapy*, 4(1):39–44, 1997.

[27] G Biswas, M Breuer, and F Durst. Backward-facing step flows for various expansion ratios at low and moderate reynolds numbers. *Transactions-American Society of Mechanical Engineers Journal of Fluids Engineering*, 126:362–374, 2004.

[28] Jaroslav Tihon, V Pěnkavová, and M Pantzali. The effect of inlet pulsations on the backward-facing step flow. *European Journal of Mechanics-B/Fluids*, 29(3):224–235, 2010.

[29] J Tihon, V Pěnkavová, J Havlica, and M Šimčík. The transitional backward-facing step flow in a water channel with variable expansion geometry. *Experimental Thermal and Fluid Science*, 40:112–125, 2012.

[30] Aditya Mushyam, Josep M Bergada, and C Navid Nayeri. A numerical investigation of laminar flow over a backward facing inclined step. *Meccanica*, 51(8):1739–1762, 2016.

[31] Petr Louda, Jaromír Příhoda, Karel Kozel, and Petr Sváček. Numerical simulation of flows over 2d and 3d backward-facing inclined steps. *International Journal of Heat and Fluid Flow*, 43:268–276, 2013.

[32] Robin Fåhræus and Torsten Lindqvist. The viscosity of the blood in narrow capillary tubes. *American Journal of Physiology–Legacy Content*, 96(3):562–568, 1931.

[33] DE Brooks, JW Goodwin, and GV Seaman. Interactions among erythrocytes under shear. *Journal of Applied Physiology*, 28(2):172–177, 1970.

[34] Sandy FC Stewart, Eric G Paterson, Greg W Burgreen, Prasanna Hariharan, Matthew Giarra, Varun Reddy, Steven W Day, Keefe B Manning, Steven Deutsch, Michael R Berman, et al. Assessment of cfd performance in simulations of an idealized medical device: results of fda's first computational interlaboratory study. *Cardiovascular Engineering and Technology*, 3(2):139–160, 2012.

[35] Frans TM Nieuwstadt, Jerry Westerweel, and Bendiks J Boersma. *Turbulence: Introduction to Theory and Applications of Turbulent Flows*. Springer, 2016.

[36] Parviz Moin and Krishnan Mahesh. Direct numerical simulation: A tool in turbulence research. *Annual review of Fluid Mechanics*, 30(1):539–578, 1998.

[37] Kamal Selvam, Jorge Peixinho, and Ashley P Willis. Localised turbulence in a circular pipe flow with gradual expansion. *Journal of Fluid Mechanics*, 771, 2015.

[38] *ANSYS Inc.* ANSYS Fluent 16.1 Documentation.

[39] Henk Kaarle Versteeg and Weeratunge Malalasekera. *An Introduction to Computational Fluid Dynamics: The Finite Volume Method*. Pearson Education, 2007.

[40] Frank M White. *Fluid Mechanics*. Boston: McGraw-Hill Book Company, 2003.

[41] Julian CR Hunt, Alan A Wray, and Parviz Moin. Eddies, streams, and convergence zones in turbulent flows. 1988.

[42] Lawrence P Harter, Barry H Gross, Peter W Callen, and Richard A Barth. Ultrasonic evaluation of abdominal aortic thrombus. *Journal of Ultrasound in Medicine*, 1(8):315–318, 1982.

[43] David A Vorp, Paul C Lee, David HJ Wang, Michel S Makaroun, Edwin M Nemoto, Satoshi Ogawa, and Marshall W Webster. Association of intraluminal thrombus in abdominal aortic aneurysm with local hypoxia and wall weakening. *Journal of Vascular Surgery*, 34(2):291–299, 2001.

[44] Trung B Le, Iman Borazjani, and Fotis Sotiropoulos. Pulsatile flow effects on the hemodynamics of intracranial aneurysms. *Journal of Biomechanical Engineering*, 132(11):111009, 2010.

[45] Barry J Doyle, Timothy J Corbett, Anthony Callanan, Michael T Walsh, David A Vorp, and Timothy M McGloughlin. An experimental and numerical comparison of the rupture locations of an abdominal aortic aneurysm. *Journal of Endovascular Therapy*, 16(3):322–335, 2009.

[46] TT Lim. An experimental study of a vortex ring interacting with an inclined wall. *Experiments in Fluids*, 7(7):453–463, 1989.

[47] R Verzicco and P Orlandi. Normal and oblique collisions of a vortex ring with a wall. *Meccanica*, 29(4):383–391, 1994.

[48] Karim Shariff and Anthony Leonard. Vortex rings. *Annual Review of Fluid Mechanics*, 24(1):235–279, 1992.

[49] T Maxworthy. Some experimental studies of vortex rings. *Journal of Fluid Mechanics*, 81(3):465–495, 1977.

[50] KC Stewart, CL Niebel, S Jung, and PP Vlachos. The decay of confined vortex rings. *Experiments in Fluids*, 53(1):163–171, 2012.

[51] Norbert Didden. On the formation of vortex rings: rolling-up and production of circulation. *Zeitschrift für Angewandte Mathematik und Physik (ZAMP)*, 30(1):101–116, 1979.

[52] Sheila E Widnall and JP Sullivan. On the stability of vortex rings. In *Proceedings of the Royal Society of London A: Mathematical, Physical and Engineering Sciences*, volume 332, pages 335–353. The Royal Society, 1973.

[53] Sheila E Widnall, Donald B Bliss, and Chon-Yin Tsai. The instability of short waves on a vortex ring. *Journal of Fluid Mechanics*, 66(1):35–47, 1974.

[54] Sheila E Widnall and Chon-Yin Tsai. The instability of the thin vortex ring of constant vorticity. *Philosophical Transactions of the Royal Society of London A: Mathematical, Physical and Engineering Sciences*, 287(1344):273–305, 1977.

[55] Thomas Leweke, Stéphane Le Dizès, and Charles HK Williamson. Dynamics and instabilities of vortex pairs. *Annual Review of Fluid Mechanics*, 48:507–541, 2016.

[56] Yasuhide Fukumoto and Yuji Hattori. Curvature instability of a vortex ring. *Journal of Fluid Mechanics*, 526:77–115, 2005.

[57] Yuji Hattori and Y Fukumoto. Short-wavelength stability analysis of thin vortex rings. *Physics of Fluids*, 15(10):3151–3163, 2003.

[58] Richard R Kerswell. Elliptical instability. *Annual Review of Fluid Mechanics*, 34(1):83–113, 2002.

[59] Sheila E Widnall. The structure and dynamics of vortex filaments. *Annual Review of Fluid Mechanics*, 7(1):141–165, 1975.

[60] Philip G Saffman. *Vortex Dynamics*. Cambridge university press, 1992.

[61] T Maxworthy. The structure and stability of vortex rings. *Journal of Fluid Mechanics*, 51(1):15–32, 1972.

[62] William Thomson. Vibrations of a columnar vortex. *The London, Edinburgh, and Dublin Philosophical Magazine and Journal of Science*, 10(61):155–168, 1880.

[63] http://jean-pierre.moreau.pagesperso-orange.fr/c_bessel.html.